Molecular Dynamics Simulations of Alkane-Functionalized Polyhedral Oligomeric Silsesquioxane (POSS)

by

Jinhua Zhou

A dissertation submitted in partial fulfillment
of the requirement for degree of
Doctor of Philosophy
(Materials Science and Engineering)
in The University of Michigan
2009

Doctoral Committee:

Professor John Kieffer, Chair
Professor Sharon C. Glotzer
Assistant Professor Joerg Lahann
Assistant Professor Anton Van der Ven

Table of Contents

List of Figures

List of Tables

List of Appendices

Chapter 1

Introduction

1.1 Polyhedral Oligomeric Silsesquioxanes

Polymer based nano-composites, i.e., materials that have structures with disparate nature juxtaposed at nano-scale level, provide a low-cost alternative to high-performance composites due to their ability to merge the component properties at the molecular scale [1, 2]. These hybrid nano-composites have a wide range of applications, which include but are not limited to biodegradable material such as food packaging; health care products and agricultural mulch film; thermally reversible gels that can be used for artificial muscles; drug delivery systems and chemical valves in microfluidic devices; low-flammability products; compatibility enhancement in otherwise immiscible polymers; and in general, materials with polymer/inorganic interfaces that have unique structure and dynamics to yield properties better than the mere sum of the constituent bulk properties [3]. When classified by nanofiller dimensionality, one can distinguish between different types of nano-composites including zero-dimensional (nanoparticle), one-dimensional (nanofiber), two-dimensional (nanolayer), and three dimentional (interpenetrating network) systems [3].

Among polymer nano-composites, functionalized polyhedral oligomeric silsesquioxane (POSS) molecules are an interesting class of 3-D nano-composites. With

organic and inorganic compounds covalently bonded to each other, these materials therefore form inherently diverse building blocks that combine contrasting characteristics at the molecular level. Silsesquioxane, by definition, refers to all structures with the chemical formula $(RSiO_{1.5})_n$, where R can be hydrogen or various hydrocarbons and their derivatives. With every silicon atom bonded to three oxygen atoms and one functionality available for the organic functional groups, this robust silicon-oxygen frame can form the basis for a wide variety of building block geometries varying in size from 1 to 3 nm. As shown in Fig. 1-1, these geometries include random structures, ladder structures, cage structures, and incompletely condensed structure, etc [1]. The most common polyhedral structure is the cubic shaped POSS with formula $R_8Si_8O_{12}$, even though other cages with well-defined geometries include n = 6, 10, 12, 14, 16 and 18 [4, 5]. Cubic POSS, therefore, is the focus of this research. Unless otherwise stated, throughout this thesis the POSS acronym specifically refers to cubic POSS. By varying the nature of the organic molecules attached to the corners of the cubic POSS cage, one hopes to control the functionality of these building blocks and thereby achieve different types of nano-composites, including highly cross-linked thermosets [6], porous networks [7], and a variety of branched copolymers [8, 9]. Appropriate functionalization of POSS cages also allows one to manufacture novel composites by taking advantage of existing manufacturing processes. For example, manipulating the chemical compatibility of these building blocks facilitates their incorporation into traditional thermoplastic resins [10].

Currently, more than 120 POSS reagents and POSS monomers are commercially available [1]. As a third-generation nano-composite —the first generation being sol-gel derived materials [11], and the second generation polymer with clay and mineral fillers

[12]— POSS possesses inherent ability to spontaneously assemble into a wide variety of nanostructures-spherical or cylindrical micelles, bicontinuous channels, co-alternating layers, and complex combinations thereof-in the melt. The resulting nano hybrid materials have a wide range of applications that will be discussed in detail in this chapter. Because of the commercial accessibility, the ease of processing and the wide applications, POSS based polymers have received increasing attention. Publication on POSS has increased more than ten-fold in the last decade [13] including several review papers [13-16].

Currently, POSS is widely employed in the industry of lightweight, high-temperature plastics, lubricants, insulation, and materials resistant to atomic oxygen, etc. The following is a brief overview of the principal current and potential future usages of POSS based nano-composites:

1.1.1 Building blocks for self-assembly

The salient feature of POSS in the ability to functionalize the silicon corner with a vast variety of organic groups, enabling bottom-up manipulation of matter to design nano-composites with varying topology and architecture and meeting the materials performance requirements in different circumstances. Most commonly fabricated patterns are lamellar and micelle structures.

Several groups have been very successful in assembling lamellar patterns. Leu's group has synthesized lamellar-shaped POSS-polyimide [17-19]. Cui et. al. successfully assembled lamellar structures with molecules composed of a POSS particle bonding to mono-tether 2-hydroxy-3, 7, 10, 11-pentakis(pentyloxy)triphenylene (P5T-OH) [20]. In the structure Cui created, every two layers of cube-shaped POSS molecules and another

two layers of disk shaped P5T-OH stack alternatively to form lamellar structure, the orientation of disk perpendicular to the layer.

Micelle and spheric topologies are also commonly seen in POSS-based assemblies. Knischka et. al. observed micellar and vesicular structures in POSS-based amphiphiles [21]. Sometimes micelle-patterned POSS systems arouse special interest because well-designed nano-porous materials could be obtained from the micelle phase by selective erosion of one phase domain from the hybrid material [22]. POSS that is functionalized with seven hydrophobic cyclopentyl groups and polyoxazoline (POZO) as hydrophilic segment can form micelles in an aqueous environment with various POSS:POZO ratio [23].

During the self-assembly process of POSS-based nano-composites, the utilization of non-covalent interactions, both intra- and inter-molecular, remains one of the principal forces that facilitate the assembly of nanoscale configurations. From the thermodynamic point of view, pattern formation is driven by the reduction of surface energy between chemically linked, yet incompatible, blocks. Limitation remains, however, in that long annealing times are needed to approach thermodynamically favorable structures in block copolymer morphologies. The amount of each component in the hybrid system is also a key factor in determining the final structure. For example, with low percentage of POSS, POSS-polybutadiene composites form lamellae that are randomly oriented; while at higher percentage, lamellae are configured parallel [24].

The length of the organic chains is usually adjusted to control the ratio between the composing components, and hence to obtain the desired pattern at the desired length scale. Our collaborators Zhang et. al. have proven, using molecular simulation, that

simply by changing the percentage of POSS or the solution, the topology can change from lamellae to micelles, illustrating the marvelous tunability of nano-composites based on this building block [25].

One benefit of having POSS as the building block for nano-composites is the ability to greatly enhance the miscibility between different polymer chains or different segments of copolymers. As observed by Mather et. al., attaching POSS to both ends of polymer chains, creating so-called telechelic molecules, greatly increases the compatibility and lower the interfacial tension between otherwise immiscible polymeric systems [26]. Huang et. al. made similar findings, putting POSS at the end of the PMMA chain increases the miscibility of PMMA with phenolic blends [27]. When blending PMMA and PS, POSS cubes attached to PMMA enhances the compatibility between the two polymers due to the attraction between POSS and PS, thus reducing the domain size and increasing the interface width, which leads to improved fracture toughness [28]. POSS is also found to increase the miscibility between the soft and hard segments of PE/polyurethane copolymer once attached PE segments [10].

The incorporation of POSS also largely influences the crystallinity of the polymer matrix. When a small amount of POSS is incorporated, isotactic polypropylene is easier to crystallize under both isothermal and nonisothermal conditions with increased crystallization rate. It is suggested that POSS might act as nucleation agent. When the amount of POSS exceeds 30 wt-%, the crystallization rate is reduced due to possible retarded growth by POSS [29].

When POSS, which is hydrophobic, is connected with hydrophilic components, the hydrophobicity of the resulting composites can be controlled by the ratio between POSS

and the organic material. When monofunctionalized with poly(ethylene glycol) (PEG) by direct urethane linkage between the diol end groups of PEG and the monoisocyanate group that is attached to POSS, the hydrophobicity of the composites can be controlled by the balance between the hydrophilic PEG and hydrophobic POSS [30]. A range of thermal and morphological properties can be obtained by controlling the POSS/PEG ratio. For example, the crystallinity of PEG is decreased by increasing the amount of POSS. The resulting PEG/POSS nano-hybrid matrix can be further employed as nano-reactors for metal and semiconductor particle formation [31], acting as the reducing agent for the metal salts and stabilizer for these metallic nano-particles, with its well-defined networks loaded with metal colloids.

When attached with other nano-particles, POSS acts as an intervening agent to adjust the spacing between large nano-particles such as gold nano-particles [32, 33], and modifies the physical, chemical, and electronic behavior of gold nano-particle assemblies accordingly [34]. The effect of POSS on the self-assembly behavior of polymers is interesting in itself, because it provides insights into bio-molecular self-assembly, such as the formation of the pathological asmyloid fibrils that play a role in Alzheimer's disease [35, 36].

1.1.2 Thermal and mechanical properties

An increase of the glass transition temperature is observed for various POSS-polymer systems upon incorporation of POSS. For the linear copolymers POSS-methacrylate/butyl methacrylate and POSS/methacrylate, blended at a ratio of 1:9, the softening point is found to be as much as 130 °C higher than the 20 °C glass-transition temperature of atactic poly(butyl methacrylate) [37]. In poly-norbornyl that contains

POSS in its side-branches, the increase of the α-relaxation temperature compared to the original poly-norbornyl is in proportion to POSS weight percentage, and so is the increase in elastic storage modulus [38]. Higher glass transition temperatures are also reported for branching systems with a backbone of polyurethane/PE copolymer [10], poly(vinylpyrrolidone-co-isobutyl), poly(acetoxylsryrene-co-isobutyl) [39], and styrene-butadiene-styrene triblock copolymer [40].

For complex systems formed from multi-functionalized POSS monomers, the effect on the glass transition temperature is mixed. With small amounts of POSS multi-bonded to vinyl ester, the glass transition temperature as well as the width of the tan δ peak in the glass transition range is not affected; while higher amounts of POSS invokes the elevation of glass transition temperature [41]. Huang et. al. observed increased T_g along with increased miscibility in POSS-PMMA/phenolic blends and attributed both effects to a stronger inter-association interaction of hydroxyl-siloxane [27].

The thermal decomposition temperature is an important factor that affects material stability. Zheng reported increased thermal decomposition temperatures in both PE/POSS random copolymer [42], and in the syndiotactic polystyrene/POSS copolymer [43]. Thermal stability and mechanical properties are largely improved in POSS/polyimide composites compared to the parent polyimide [44].

Other researchers carried out investigations in mechanical properties. The incorporation of POSS increases the Young's modulus and the glass transition temperature for ethylene-propylene copolymer [45]. For a system of ABA triblock copolymers, in which A refers to the rubbery poly(n-butylacrylate) and B refers to the glassy propyl methacrylate POSS, both increased glass transition temperature and

enhanced Young's modulus are observed [46]. Incorporation of about 31 wt-% POSS into polyimides backbones greatly improves the chemical stability, with no measurable level of erosion when exposed to atomic oxygen [47].

1.1.3 Nano-porous structures

Due to the size of the nanoparticle and the weak interaction between POSS and the polymer matrix, POSS-based copolymers by nature exhibit a high degree of porosity. The free volume of the interstitial nano-pores introduced by the nano-particles, makes the nano-composite the ideal candidate for gas/vapor separation membranes [48-50]. Porosity can be controlled by varying the architecture or altering the interaction between components. For example, the amino-POSS/chitosan composites are more porous than epoxy-POSS/chitosan due to the stronger interaction between epoxy group and chitosan that contains amino groups [51]. The length of the tether is also an important factor. Comparing between tether –CH2-CH2- and –O-Si(CH3)2-CH2-CH2-Si(CH3)2-O-, the network structure formed by the latter is found to have higher degree of reaction (81%), indicating more cross-links. The composite has less porosity, with smaller pore sizes, and consequently more efficient packing of POSS cubes. The reason for this probably is that the longer flexible linkages have more degrees of freedom for the polymer to fold, and thus are less prone to the steric hindrances imposed by the growing covalent network [52, 53].

The porous nature of POSS based nano-composites leads to an extensive shrinkage upon aging, which sometimes could cause serious engineering design problems. In some cases, however, shrinkage depression is desired at some circumstances and can be achieved by increasing the fraction of macro-pores out of total free volume. Some

materials, display shrinkage behavior followed by spring-back expansion [54]. Shrinkage can be controlled by surface modification or solvent exchange. The spring-back effect is attributed to the hydrophobicity and low concentration of reactive groups on the surface.

1.1.4 Electrical and optical properties

The incorporation of POSS into polymer systems, either through physical blending or chemical reaction changes the optical and electrical properties dramatically. The POSS particles dispersed in the polymer matrix constitute light scattering centers. The overall scattering behavior to light of certain wavelength is determined by the spatial distribution of the POSS particles. At the presence of electrical field, POSS nano-composites can switch from being transparent to reflective, making it an effective electro-optic switch device [55]. POSS is also used to alter the properties of light-emitting organic molecules. The incorporation of POSS modifies the interaction within organic matrix and accordingly the vibration frequency that atoms experience. Thus the wavelength of the emitting light can be changed. Cho et. al. achieved blue light emission for the first time by reacting POSS with electroluminescent terfluorene chromophore [56].

The addition of POSS particles is also an effective way for changing the electrical properties of nano-composites. Incorporation of as little as 2.5 mol% of POSS into polyimide reduces the dielectric constant from 3.40 to 3.09 [18]. Incomplete methyl-silsesquioxane which contains fewer than eight silicon atoms in the cube is introduced into polyimide to adjust refractive index and dielectric constant [44]. A substantial decrease in dielectric constant is also reported in urethane/POSS nanoporous film [57]. Different explanations are given for this behavior; Leu is crediting the increased free volume [19], while Muthukrishnan is holding the hindered polymerization reaction

responsible [58]. Other applications for POSS-based nano-composites include the immobilizing of metal cations, especially transition metals [59-63] to improve their catalytic efficiency [64-66]. POSS can be assembled to form dendrimer-like catalyst carriers and drug delivery vehicle [58, 67-70]. Finally, controlled alignment of POSS cubes can be exploited for nanolithography [71].

1.1.5 Motivation

To produce improved POSS-containing polymers on any basis other than trial and error, structure-property relationships for a variety of POSS-containing thermoplastics must be thoroughly understood. Even with the enormous amount of papers about POSS published in recent years, the understanding of the relationship between the structure and property is far from comprehensive. For example, no largely recognized explanation has been given yet for the mechanism underlying the mechanical reinforcement by POSS. However, this understanding is crucial in that it provides guideline for the design of novel POSS-based copolymers with specific properties.

So far, it has been hypothesized that particle size and the nature of molecular interactions are responsible for enhanced thermal and mechanical properties. Li. et. al. believe that the sterically bulky and heavy POSS particles hinders the motion of the chain segments, and hence leads to higher T_g [16, 41]. Pyun identified the importance of the size by comparing two systems with the same weight percentage of POSS: aggregated vs. evenly distributed. The author found that the aggregated POSS system has a higher T_g, proving the contributing factor of size [46]. The bulky POSS clusters are also believed to reduce chain entanglement, which results better mechanical properties [72].

Xu et. al., on the other hand, proposed that the intra- and inter-molecular interactions between POSS and surrounding compounds has the dominant role in enhancing T_g in poly(acetoxylstyrene-co-isobutylstyryl-POSS) (PAS-POSS) and poly(vinylpyrrolidone-co-isoutylstyryl-POSS) (PVP-POSS) [39]. In their experiment they observed that smaller amounts of POSS disrupts the self-association of the matrix and leads to decrease in T_g. In a subsequent paper with similar findings, Xu et. al. included the size of the aggregated POSS particles also as one of the possible causes for enhanced thermal stability of these materials, in addition to molecular interactions [73]. Strachota et al. also credit the affected POSS interaction as the cause of improved mechanical properties [74]. This explains why most improvement is observed in networks with pendent POSS acting as cross-linkers

Blocking the interactions between epoxy chains and diamine groups is believed to have altered the dielectric constant [58]. Modified interactions is held responsible for the high degree of porosity in POSS systems as well. Composites formed with chitosan and amino-POSS are more porous than those involving epoxy-POSS, because interactions are weaker while in the epoxy system strong chemical bonds are established between the amino groups of chitosan and the epoxy groups of POSS [51].

Naturally, the interactions would have strong impact on crystallization process too. As mentioned earlier, POSS facilitates crystallization in isotactic polypropylene under both isothermal and non-isothermal conditions with increased crystallization rate [29]. It is suggested that the well-dispersed POSS particles might have acted as nucleation agent. Therefore the overall orientation of the polymer chains is improved and a faster crystallization rate is obtained with the addition of POSS. Isotactic polypropylene nuclei

are probably initiated in large numbers near molecularly dispersed POSS molecules. In PE/polynorbornene/POSS copolymers in which POSS is attached to polynorbornene backbone, disordered domains of POSS form first before the subsequent crystallization of PE occurs on cooling from the molten state. When precipitating PE from xylene, it forms crystal first with limited POSS crystallization [75].

When investigating the guiding principles behind the reinforcement of polymer matrixes through POSS, simulation provides as a useful tool to examine the copolymer system at the molecular scale. The advantage of simulation is that it allows investigators to access atoms and interactions with a level of detail that experimentalists cannot. For example, one can examine how the polymer conformation changes to adapt to the POSS, how far apart the POSS cages are, or how any of these issues affect the microstructure and particular property of interest. Being able to understand in detail how POSS groups interact within an oligomer of known length is essential to creating better polymers. Another advantage of simulation is that it allows for extracting different factors and determining their effects one by one. One typical example is polydispersity. Since polydispersity is inevitable in experiment, it is difficult to accurately determine the effect of the size or the weight ratio on the overall structure and the resulting property whereas in simulations particles can be made perfectly the same size throughout the system.

This thesis work was focused on the simulation of POSS-based copolymers, specifically, POSS-hydrocarbon composites to investigate the effect of weight percentage, bonding architecture on the structure and dynamics of the resulting composites.

1.2 Literature Review

1.2.1 Synthesis

The first synthesis of POSS began in the 1940s when Scott and Patnode et. al. made an effort to make cyclic Si-O structures through hydrolysis, resulting in four-member rings [76, 77] However, it was not until 1955 that proper characterization occurred with X-ray crystallography that verified the existence of POSS [78]. Muller reported the existence of octa-silsesquioxane in 1959 [79]. Larson measured the crystal structures of POSS with X-ray diffraction and provided the estimated coordinates [80-82]. Brown Jr. and Vogt Jr. synthesized the cubic POSS structure with the fourth silicon valence terminated by hydrogen, which was termed as T8, by hydrolysis of cyclohexylsilanetriol. This also yielded side products, including various incomplete POSS structures [83]. Significant synthetic advances were made in 1989 when Feher [84] improved on earlier synthetic methods [83] to make well-defined incompletely condensed POSS, which permitted the easy synthesis of polymerizable POSS such as Cp7T8(R') where R' is organic component with single functionality, such as propyl methacrylate [8], norbornene [85], or styrene [86]. In 1993, the first POSS polymers were synthesized [87]. Functionalized POSS are more elegantly incorporated into thermoplastics by copolymerization than by mere blending to yield a nano-composite. Chemically bonded POSS can either dangle from, or be part of, the polymer backbone.

In general, most of the precursors to silsesquioxanes find their origin in trichlorosilanes. These are frequently prepared from the silicone industry's direct process reaction of methyl chloride or hydrogen chloride with silicon metal, catalyzed with copper. From there, separate efforts are carried out to synthesize POSS monomers and

POSS composites. Marcolli and Calzaferri summarized three possible synthetic routes to prepare POSS monomer: they are co-hydrolysis of trifunctional organo/hydro silanes [16, 88]; substitution reactions with retention of the POSS cages [88]; and corner capping reactions [8, 16, 88]. Worth noting is that alkyl groups larger than methyl and organo-functional groups are formed by platinum-catalyzed hydrosilylation reactions with trichlorosilane or by organometallic coupling reactions with chlorosilanes [14]. Shockey et. al. reported a fabrication recipe for POSS silane and α-olefin monomers that are suitable for polymer grafting reactions [89].

Furthermore, POSS monomers can be inserted into polymer matrix by having corner groups replaced or attached the corner groups to polymer backbone through reaction, usually at the presence of a catalyst. Zheng et. al reported the fabrication of POSS/PE system with POSS grafted to PE backbones by reaction of POSS with ring-opening cyclic structure such as cyclooctene [42]. Multi-functionalized POSS with mesogens are obtained through corner group reaction method [90]. Choi et. al. successfully synthesized a series of network structures by adjusting the ratio of reactive tethers to POSS cages [91]. Through replacement of the organic ligands at the corners, a series of POSS polymers can be obtained [58].

Besides the most common POSS system, which is cubic POSS with organic tethers, there are other POSS systems synthesized for specific purposes. Fabrication of metal-POSS was intended to produce ideal catalyst [59]. Instead of forming cyclic groups, silsesquioxane can form bridged network with the features of a gel [92, 93]. So-called incomplete POSS can be readily obtained through cleavage of Si-O-Si bonds [94].

There are several well-written review articles concerning: Baney et. al. summarized the synthesis, characterization and properties of several silsesquioxanes including phenylsilsesquioxane, methylsilsesquioxane, aliphatic silsesquioxane, vinyl-functional silsesquioxane, methacryl-functional silsesquioxane, amino-functional silsesquioxane, and epoxy-functional silsesquioxane [14]. Li et. al. summarized the synthesis and properties of homopolymers and copolymers of monomers containing POSS strcures. Monomers, such as styryl-POSS, methacrylate-POSS, norbornyl-POSS, vinyl-POSS, epoxy-POSS, and siloxane-POSS, are also described in this article. Both monofunctional and multifunctional monomers are described in reference [16].

1.2.2 Categorization of POSS

Determined by the bonding architecture, POSS composites can be divided into several groups:

- Dendrimers can be obtained if all eight corners of POSS are functionalized with organic tethers which further bifurcate [58, 67-70]. When more than two corners of the cubic POSS core is functionalized with organic substitutes, the resulting nano-composites form complex network structure and sometimes gel systems. Examples include multi-functionalized POSS/mesogen system [90] and POSS containing dimethacrylate network [95]. It is found in the latter system that multi-functionalized POSS is well dispersed and acts as cross-links to the polymeric system.
- When exactly two corners of the POSS particle are functionalized, they are considered to form linear copolymers or "bead" structure [37, 96]. They can be easily incorporated into other polymer backbones as a repeat unit [97]. Not all bi-functionalized POSS form "bead" structures, some of the corner tethers could bond

with another functional group on the same POSS cube, and form a buckle along the edge or face of the POSS particle (Rick).

- The most common and easier-to-investigate system involves POSS with only one functionality. A great amount attention is devoted to this category because of the relative ease to control the structure with different input. This group can be further put into two sub-groups: mono-tether terminus group and pendent structure [37]. The precursor for pendent POSS structure, however, is usually a mono-tether terminus macromer to start with [86]. POSS can be attached to the one or both ends of the polymer chain to form snake or dumbbell shaped structure [18]. One example of a snake structure is attaching POSS to one end of a PMMA chain [27]. Another example of mono-functionalized POSS system includes the mono-functionalized transition metal POSS systems that can be used for catalysis [60]. POSS can also be grafted to polymer backbone as a hard segment, resulting POSS-siloxane-POSS triblock structure [89]. POSS is bonded to polyimide backbones to form pendent structure [18, 47]. Similar pendent structures include PMMA backbones [28, 72], polyethylene [8, 9, 98], polyethylene with POSS-styryl macromer as branch [43], polystyrene [43, 99], polyisoprene/polystyrene block copolymer with POSS attached to polyisoprene [22], polyurethane/PE copolymer with POSS attached to PE [10], poly-norbornylene [38, 98, 100], polynorbornylene/PE copolymer with POSS to norbornylene [42, 75], poly(p-phenylenevinylene) [101], epoxy networks [74], styrene-butadiene(with POSS grafted)-styrene triblock copolymers [40], and epoxy-amine networks [102]. Sometimes the dangling pendant POSS aggregates can cause phase separation [95].

- Another big group is the material formed by physically mixing POSS and polymer components, such as physically blended POSS-isotactic polypropylene [29] or physical and chemical (mono) blending gels [103-105].. When physically mixing POSS with epoxy resin, the elastic moduli increase, the glass transition temperature decreases, and oxidation resistance improves [106]. A recent paper by Joshi et. al. presents the physically mixed POSS/polymer hybrids. At low concentration, POSS is evenly distributed and the viscosity of the matrix decreases probably it reduces the entanglement of polymer chains; At higher concentrations, POSS tends to aggregate and hinder the mobility of the matrix, which leads to higher viscosity and phase separation [107].

1.2.3 Characterization

Larsson seems to be the first to report the crystal structure of octa-silsesquioxane [82]. In the early 1990s, a group of scientist revisited the material and provided an updated crystal structure with unit cell coordinates and bonding structures derived from X-ray [108]. Infrared Spectrum [109, 110] and normal coordinate analysis [110, 111] of $H_8Si_8O_{12}$ are carried out right afterwards. Aebi et. al. measured the mass spectra of a series of POSS compounds with different corner groups [112]. In the same year, Bornhauser and Calzaferri reported vibrational spectra and normal coordinate analysis for spherosiloxanes including cubic POSS [113]. In 1997, Marcolli and Calzaferri assigned the peaks in infrared spectra and Raman spectra to different localized motions for $RH_7Si_8O_{12}$, where R could be a list of various organic and inorganic groups [114]. Auner et. al. studied the crystal structure of POSS with short tethers [115].

Substantial effort has been put to the investigation of thermolysis of POSS. During the decomposition process, the POSS-Siloxane copolymer, in which POSS has six cyclohexyl and two other groups such as OH and Osi(Methyl)3, starts to lose siloxane chain at 400˚C, followed by cyclohexyl hydrocarbon from 450 to 550˚C. The POSS Si-O framework is retained up to 500˚C. Decomposition of the silsesquioxane "cage" structure occurs between 450 and 650˚C, and the final structure is Si-O-C network [97]. Waddon and Coughlin summarized papers about crystal structures of octa-functionalized POSS [116]. T8H8 forms a hexagonal shaped lattice with ACBA stacking [82]. When the corners are attached with alkyl chains or cyclo-alkanes, the crystal structure largely retains the shape with extended box size [10, 80, 81]. When POSS is decorated with norbornyl groups instead of hydrocarbon, the same pattern follows [75, 98].

When isobutyl-POSS with one of the functional groups being aromatic diamine is reacted with epoxy system, phase separation is observed, probably due to incompatibility between isobutyl groups with the armatic epoxy-amine network. R groups have strong influence on whether POSS are miscible with the polymer matrix [41], and whether POSS would uniformly distribute in the organic matrix or aggregate to form particles of various shapes [106]. The amount of POSS present also matters. A small amount of pendent POSS with PMMA backbone well dispersed in the polymer matrix while lager amount of POSS introduced aggregation and small crystallinity domain [72]. The existence of a coupling agent, e.g., 3-aminopropyltrimethoxysilane, can retard phase separation, indicating the effectiveness of chemical bonding in preventing phase separation [44]. It is also found that dangling POSS are more likely to aggregate while multi-functionalized POSS act as cross-link and are better dispersed [102]. Aggregating

POSS themselves can act as physical cross-links to retard the motion [74]. Some other efforts no phase separation include the investigation by Kopesky et. al. of properties of blends between non-tethered POSS/polymer and tethered POSS/polymer [72].

1.2.4 Simulation

Atomic scale simulations provide a unique approach for elucidating the local morphologies and their effects on mechanical reinforcement in hybrid nano-composites, at a level that is difficult, if not impossible, to access in experiments. For example, polydispersity is inevitable in polymer synthesis, whereas in simulations the length of the substituting organic groups is precisely known when examining its effect on the structure and properties of the composite materials.

Quantum mechanical calculations were carried out to compare the stability of cubic POSS with cyclic silsesquixoane structure with different number of silicon atoms [117]. The structures of some silsesquioxane organometalic complex were determined using ab initio calculation [118, 119]. In the same year, Xiang et. al. reported the simulated structure and electronic distribution of cyclic H-silsesquioxanes including cubic POSS [120]. Quantum mechanical calculation tracks not only the atoms but also the electronic cloud of each atom, hence provides accurate description of structural features about the materials. However, due to the enormous amount of calculation involved, it is usually employed to study small systems of no more than 100 atoms. Hence it is very effective to study the stability of one single POSS cube under conditions such as containing hydrogen/deuterium inside the cube structure [121]. Sometimes, the findings of quantum mechanical calculations, such as charges on atoms and bonding distances between species, can be used as reference for molecular level or even meso-scale simulations.

Molecular dynamics (MD) simulation is common in studying structural and dynamic properties at molecular level. The effect of tethers on the assembly behavior and properties of the resulting POSS structures was studied through molecular dynamics simulation using a commercial force field [91]. It is found that two types of POSS cages of different tethers, when inserted into diaminodiphenylmethane (DDM), exhibit different fracture toughness in the resulting composites. The structure containing octaglycidyldimethylsiloxy-octasilsesquioxane (OG) have the ability to extend 200% compared to 50% of the structure containing octa(ethylcyclohexylepoxide)dimethylsiloxy silsesquioxane (OC). Other researchers used MD simulations to determine the pore sizes of a POSS-polymer complex structure [52] and investigate the properties of POSS in organic solvents [122, 123]. Based on Newtonian mechanics, molecular dynamics simulation has been a powerful tool on elucidating the local morphologies and their effects on mechanical reinforcement. The key to MD simulation is a force field that provides accurate description of atomic interactions. So far, most force fields being used are commercial force field not designed for POSS.

Monte Carlo simulation is also a popular method. It was carried out by Hillson et. al. to identify the preferred conformation of POSS particles [124]. The study found out that the POSS cages, compared to ladder structures, are quite rigid and retain the cube shape under different chemical architecture, differing slightly only in bonding angles. Our collaborators have also employed coarse-grained Monte Carlo simulation to study the morphologies of multiple POSS-tether systems [25, 125]. Using results from quantum mechanical calculation or molecular dynamics simulation to provide parameters for its empirical potential expression, the coarse-grained Monte Carlo simulation is effective in

identifying meso-scale morphologies. However, it relies entirely on random sampling of the simulated system and does not track the deterministic trajectories of particles like MD simulation does.

This thesis has devoted efforts to molecular dynamics simulation of alkane-functionalized POSS systems as alkane represents the simplest version of organic substitutes in POSS nano-composites.

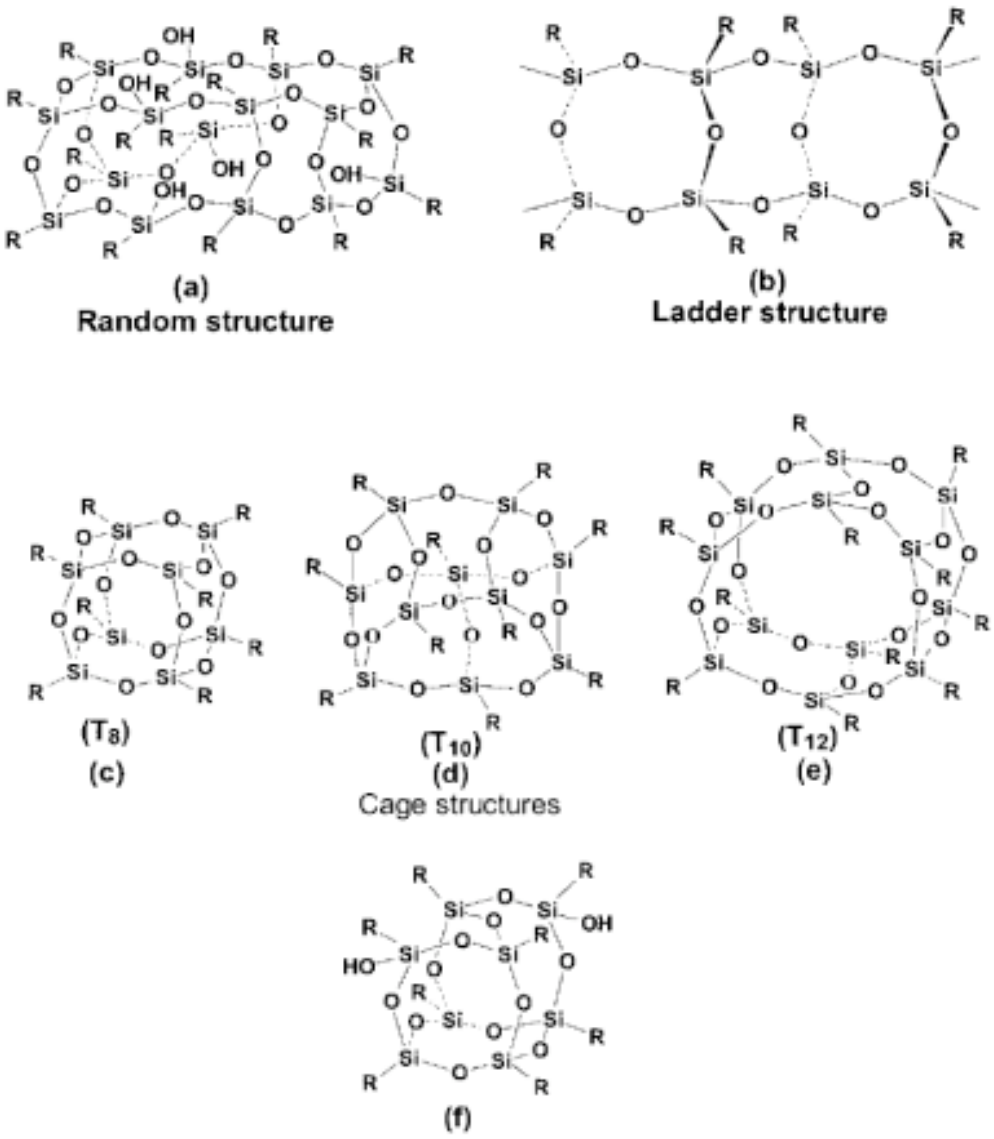

Fig. 1-1 The geometry of silsesquioxane

References

1. Lichtenhan, J.D., J.J. Schwab, and W.A. Reinerth, *Nanostructured chemicals: A new era in chemical technology*. Chemical Innovation, 2001. **31**(1): p. 3-5.
2. Sanchez, C., et al., *Designed hybrid organic-inorganic nano-composites from functional nanobuilding blocks*. Chemistry of Materials, 2001. **13**(10): p. 3061-3083.
3. Schmidt, D., D. Shah, and E.P. Giannelis, *New advances in polymer/layered silicate nano-composites*. Current Opinion in Solid State & Materials Science, 2002. **6**(3): p. 205-212.
4. Voronkov, M.G. and V.I. Lavrentyev, *Polyhedral Oligosilsesquioxanes and Their Homo Derivatives*. Topics in Current Chemistry, 1982. **102**: p. 199-236.
5. Franco, R., et al., *Theoretical study of structural and electronic properties of methyl silsesquioxanes*. Journal of Physical Chemistry B, 2002. **106**(7): p. 1709-1713.
6. Sellinger, A. and R.M. Laine, *Silsesquioxanes as synthetic platforms. Thermally curable and photocurable inorganic/organic hybrids*. Macromolecules, 1996. **29**(6): p. 2327-2330.
7. Morrison, J.J., et al., *Synthesis of functionalised porous network silsesquioxane polymers*. Journal of Materials Chemistry, 2002. **12**(11): p. 3208-3212.
8. Lichtenhan, J.D., Y.A. Otonari, and M.J. Carr, *Linear Hybrid Polymer Building-Blocks - Methacrylate- Functionalized Polyhedral Oligomeric Silsesquioxane Monomers and Polymers*. Macromolecules, 1995. **28**(24): p. 8435-8437.
9. Haddad, T.S. and J.D. Lichtenhan, *Hybrid organic-inorganic thermoplastics: Styryl-based polyhedral oligomeric silsesquioxane polymers*. Macromolecules, 1996. **29**(22): p. 7302-7304.
10. Fu, B.X., et al., *Synthesis and characterization of segmented polyurethanes containing polyhedral oligomeric silsesquioxanes nanostructured molecules*. High Performance Polymers, 2000. **12**: p. 565-571.
11. Brinker, C.J. and G.W. Scherer, *Sol-Gel Science: The physics and Chemistry of Sol-Gel Processing*. 1990, New York: Academic Press.
12. Pinnavaia, T.J. and G.W. Beall, *Polymer-Clay Nano-composites*. 2001: John Wiley & Sons.
13. Phillips, S.H., T.S. Haddad, and S.J. Tomczak, *Developments in nanoscience: polyhedral silsesquioxane (POSS)-polymers oligomeric*. Current Opinion in Solid State & Materials Science, 2004. **8**(1): p. 21-29.
14. Baney, R.H., et al., *Silsesquioxanes*. Chemical Reviews, 1995. **95**(5): p. 1409-1430.
15. Lichtenhan, J.D., *Polyhedral Oligomeric Silsesquioxanes - Building-Blocks for Silsesquioxane-Based Polymers and Hybrid Materials*. Comments on Inorganic Chemistry, 1995. **17**(2): p. 115-130.
16. Li, G.Z., et al., *Polyhedral oligomeric silsesquioxane (POSS) polymers and copolymers: A review*. Journal of Inorganic and Organometallic Polymers, 2001. **11**(3): p. 123-154.

17. Leu, C.M., Y.T. Chang, and K.H. Wei, *Synthesis and dielectric properties of polyimide-tethered polyhedral oligomeric silsesquioxane (POSS) nano-composites via POSS-diamine*. Macromolecules, 2003. **36**(24): p. 9122-9127.
18. Leu, C.M., et al., *Synthesis and dielectric properties of polyimide-chain-end tethered polyhedral oligomeric silsesquioxane nano-composites*. Chemistry of Materials, 2003. **15**(11): p. 2261-2265.
19. Leu, C.M., Y.T. Chang, and K.H. Wei, *Polyimide-side-chain tethered polyhedral oligomeric silsesquioxane nano-composites for low-dielectric film applications*. Chemistry of Materials, 2003. **15**(19): p. 3721-3727.
20. Cui, L., et al., *Supramolecular self-assembly in a disk-cube dyad molecule based on triphenylene and polyhedral oligomeric silsesquioxane (POSS)*. Chemistry of Materials, 2006. **18**(15): p. 3503-3512.
21. Knischka, R., et al., *Silsesquioxane-based amphiphiles*. Langmuir, 1999. **15**(14): p. 4752-4756.
22. Chun, S.B. and P.T. Mather. *Nanostructures from POSS-Grafted Block Copolymer Precursors*. in *Materials Research Soceity*. 2001. Boston, MA.
23. Kim, K.M., D.K. Keum, and Y. Chujo, *Organic-inorganic polymer hybrids using polyoxazoline initiated by functionalized silsesquioxane*. Macromolecules, 2003. **36**(3): p. 867-875.
24. Zheng, L., et al., *Polymer Nano-composites through Controlled Self-Assembly of Cubic Silsesquioxane Scaffolds*. Macromolecules, 2004. **37**(23): p. 8606-8611.
25. Zhang, X., E.R. Chan, and S.C. Glotzer, *Self-assembled morphologies of monotethered polyhedral oligomeric silsesquioxane nanocubes from computer simulation*. Journal of Chemical Physics, 2005. **123**(18).
26. P. T. Mather, K.P.C., T. S. Haddad and J. D. Lichtenhan, Polym. Prepr. (Am. Chm. Soc., Div. Polym. Chem.), 1996. **37**: p. 765.
27. Huang, C.F., et al., *Influence of PMMA-chain-end tethered polyhedral oligomeric silsesquioxanes on the miscibility and specific interaction with phenolic blends*. Macromolecules, 2006. **39**(1): p. 300-308.
28. Zhang, W.H., et al., *Effect of methyl methacrylate/polyhedral oligomeric silsesquioxane random copolymers in compatibilization of polystyrene and poly(methyl methacrylate) blends*. Macromolecules, 2002. **35**(21): p. 8029-8038.
29. Fu, B.X., et al., *Crystallization studies of isotactic polypropylene containing nanostructured polyhedral oligomeric silsesquioxane molecules under quiescent and shear conditions*. Journal of Polymer Science Part B-Polymer Physics, 2001. **39**(22): p. 2727-2739.
30. Kim, B.S. and P.T. Mather, *Amphiphilic telechelics incorporating polyhedral oligosilsesquioxane: 1. Synthesis and characterization*. Macromolecules, 2002. **35**(22): p. 8378-8384.
31. Chauhan, B.P.S. and U. Latif, *Inorganic/organic hybrid nanoreactors based on cyclic and cubic siloxane scaffolds*. Macromolecules, 2005. **38**(15): p. 6231-6235.
32. Hornyak, G., et al., *Gold clusters and colloids in alumina nanotubes*. Chemistry-a European Journal, 1997. **3**(12): p. 1951-1956.
33. Carroll, J.B., et al., *Electrostatic self-assembly of structured gold nanoparticle/polyhedral oligomeric silsesquioxane (POSS) nano-composites*. Journal of Materials Chemistry, 2004. **14**: p. 690-694.

34. Carroll, J.B., B.L. Frankamp, and V.M. Rotello, *Self-assembly of gold nanoparticles through tandem hydrogen bonding and polyoligosilsequioxane (POSS)-POSS recognition processes*. Chemical Communications, 2002(17): p. 1892-1893.
35. Aggeli, A., et al., *Responsive gels formed by the spontaneous self-assembly of peptides into polymeric beta-sheet tapes*. Nature, 1997. **386**(6622): p. 259-262.
36. Aggeli, A., et al., *Hierarchical self-assembly of chiral rod-like molecules as a model for peptide beta-sheet tapes, ribbons, fibrils, and fibers*. Proceedings of the National Academy of Sciences of the United States of America, 2001. **98**(21): p. 11857-11862.
37. Schwab, J.J. and J.D. Lichtenhan, *Polyhedral oligomeric silsesquioxane (POSS)-based polymers*. Applied Organometallic Chemistry, 1998. **12**(10-11): p. 707-713.
38. Mather, P.T., et al., *Mechanical relaxation and microstructure of poly(norbornyl-POSS) copolymers*. Macromolecules, 1999. **32**(4): p. 1194-1203.
39. Xu, H.Y., et al., *Preparations, thermal properties, and T-g increase mechanism of inorganic/organic hybrid polymers based on polyhedral oligomeric silsesquioxanes*. Macromolecules, 2002. **35**(23): p. 8788-8793.
40. Fu, B.X., A. Lee, and T.S. Haddad, *Styrene-butadiene-styrene triblock copolymers modified with polyhedral oligomeric silsesquioxanes*. Macromolecules, 2004. **37**(14): p. 5211-5218.
41. Li, G.Z., et al., *Viscoelastic and mechanical properties of vinyl ester (VE)/multifunctional polyhedral oligomeric silsesquioxane (POSS) nano-composites and multifunctional POSS-styrene copolymers*. Polymer, 2002. **43**(15): p. 4167-4176.
42. Zheng, L., R.J. Farris, and E.B. Coughlin, *Synthesis of polyethylene hybrid copolymers containing polyhedral oligomeric silsesquioxane prepared with ring-opening metathesis copolymerization*. Journal of Polymer Science Part a-Polymer Chemistry, 2001. **39**(17): p. 2920-2928.
43. Zheng, L., et al., *Synthesis and thermal properties of hybrid copolymers of syndiotactic polystyrene and polyhedral oligomeric silsesquioxane*. Journal of Polymer Science Part a-Polymer Chemistry, 2002. **40**(7): p. 885-891.
44. Lin, W.J. and W.C. Chen, *Synthesis and characterization of polyimide/oligomeric methylsilsesquioxane hybrid films*. Polymer International, 2004. **53**(9): p. 1245-1252.
45. Fu, B.X., et al., *Physical gelation in ethylene-propylene copolymer melts induced by polyhedral oligomeric silsesquioxane (POSS) molecules*. Polymer, 2003. **44**(5): p. 1499-1506.
46. Pyun, J., et al., *ABA triblock copolymers containing polyhedral oligomeric silsesquioxane pendant groups: synthesis and unique properties*. Polymer, 2003. **44**(9): p. 2739-2750.
47. Wright, M.E., et al., *Chemical modification of fluorinated polyimides: New thermally curing hybrid polymers with POSS*. Macromolecules, 2006. **39**(14): p. 4710-4718.
48. Stern, S.A., *Polymers for Gas Separations - the Next Decade*. Journal of Membrane Science, 1994. **94**: p. 1-65.

49. Pandey, P. and R.S. Chauhan, *Membranes for gas separation*. Progress in Polymer Science, 2001. **26**(6): p. 853-893.
50. Winberg, P., et al., *Free volume and interstitial mesopores in silica filled poly(I-trimethylsilyl-l-propyne) nano-composites*. Macromolecules, 2005. **38**(9): p. 3776-3782.
51. Strachota, A., et al., *Chitosan-oligo(silsesquioxane) blend membranes: Preparation, morphology, and diffusion permeability*. Journal of Inorganic and Organometallic Polymers, 2001. **11**(3): p. 165-182.
52. Zhang, C.X., et al., *Highly porous polyhedral silsesquioxane polymers. Synthesis and characterization*. Journal of the American Chemical Society, 1998. **120**(33): p. 8380-8391.
53. Soles, C.L., et al. *Structural Evolution of Silsesquioxane-based Organic/Inorganic Nano-composite Networks*. in *Proceedings of the Spring 2000 Meeting of the Materials Research Society*. 2000. San Francisco: Materials Research Society.
54. Dong, H.J., R.F. Reidy, and J.D. Brennan, *Shrinkage and springback behavior of methylsilsesquioxanes prepared by an acid/base two-step processing procedure*. Chemistry of Materials, 2005. **17**(24): p. 6012-6017.
55. Saez, I.M. and J.W. Goodby, *Chiral nematic octasilsesquioxanes*. Journal of Materials Chemistry, 2001. **11**(11): p. 2845-2851.
56. Cho, H.J., et al., *Electroluminescent polyhedral oligomeric silsesquioxane-based nanoparticle*. Chemistry of Materials, 2006. **18**(16): p. 3780-3787.
57. Wu, G.J. and Z.H. Su, *Polyhedral oligomeric silsesquioxane nano-composite thin films via layer-by-layer electrostatic self-assembly*. Chemistry of Materials, 2006. **18**(16): p. 3726-3732.
58. Muthukrishnan, S., et al., *Synthesis and characterization of glycomethacrylate hybrid stars from silsesquioxane nanoparticles*. Macromolecules, 2005. **38**(26): p. 10631-10642.
59. Feher, F.J., *Polyhedral Oligometallasilsesquioxanes (Pomss) as Models for Silica-Supported Transition-Metal Catalysts - Synthesis and Characterization of (C5me5)Zr (Si7o12)(C-C6h11)7*. Journal of the American Chemical Society, 1986. **108**(13): p. 3850-3852.
60. Hendan, B.J. and H.C. Marsmann, *Silsesquioxanes as models of silica supported catalyst - I. 3-(diphenylphosphino)propyl hepta propyl - octasilsesquioxane and 3-mercapto-propyl -hepta propyl - octasilsesquioxane as ligands for transition-metal ions*. Applied Organometallic Chemistry, 1999. **13**(4): p. 287-294.
61. Severn, J.R., et al., *Silsesquioxane-bonded zirconocene complexes; soluble models for silica-tethered olefin polymerization catalysts*. Dalton Transactions, 2003(11): p. 2293-2302.
62. Garrison, J.C., et al., *A fluorophenylboron-functionalized zirconium silsesquioxane complex*. Acta Crystallographica Section C-Crystal Structure Communications, 2004. **60**: p. M357-M359.
63. Wada, K., et al., *Synthesis and Catalytic Activity of Group 4 Metallocene Containing Silsesquioxanes Bearing Functionalized Silyl Groups*. Organometallics, 2004. **23**(24): p. 5824-5832.

64. Abbenhuis, H.C.L., *Advances in homogeneous and heterogeneous catalysis with metal- containing silsesquioxanes*. Chemistry-a European Journal, 2000. **6**(1): p. 25-32.
65. Duchateau, R., *Incompletely condensed silsesquioxanes: Versatile tools in developing silica-supported olefin polymerization catalysts*. Chemical Reviews, 2002. **102**(10): p. 3525-3542.
66. Hanssen, R.W.J.M., R.A.v. Santen, and H.C.L. Abbenhuis, *The Dynamic Status Quo of Polyhedral Silsesquioxane Coordination Chemistry*. European journal of inorganic chemistry, 2004. **XX**: p. 675-683.
67. Casado, C.M., et al., *Cyclic siloxanes and silsesquioxanes as cores and frameworks for the construction of ferrocenyl dendrimers and polymers*. Applied Organometallic Chemistry, 1999. **13**(4): p. 245-259.
68. Zhang, X.J., et al., *Synthesis and computer modelling of hydroxy-derivatised carbosilane dendrimers based on polyhedral silsesquioxane cores*. Journal of the Chemical Society-Dalton Transactions, 2001(22): p. 3261-3268.
69. Ropartz, L., et al., *Hydrocarbonylation reactions using alkylphosphine-containing dendrimers based on a polyhedral oligosilsesquioxane core*. Journal of the Chemical Society-Dalton Transactions, 2002(9): p. 1997-2008.
70. Dvornic, P.R., et al., *Organic-inorganic polyamidoamine (PAMAM) dendrimer-polyhedral oligosilsesquioxane (POSS) nanohybrids*. Macromolecules, 2004. **37**(20): p. 7818-7831.
71. Tegou, E., et al., *Polyhedral oligomeric silsesquioxane (POSS) acrylate copolymers for microfabrication: properties and formulation of resist materials*. Microelectronic Engineering, 2004. **73-74**: p. 238-243.
72. Kopesky, E.T., et al., *Thermomechanical properties of poly(methyl methacrylate)s containing tethered and untethered polyhedral oligomeric silsesquioxanes*. Macromolecules, 2004. **37**(24): p. 8992-9004.
73. Xu, H.Y., et al., *Preparation, thermal properties, and T-g increase mechanism of poly(acetoxystyrene-co-octavinyl-polyhedral oligomeric silsesquioxane) hybrid nano-composites*. Macromolecules, 2005. **38**(25): p. 10455-10460.
74. Strachota, A., et al., *Epoxy networks reinforced with polyhedral oligomeric silsesquioxanes (POSS). Thermomechanical properties*. Macromolecules, 2004. **37**(25): p. 9457-9464.
75. Waddon, A.J., et al., *Nanostructured polyethylene-POSS copolymers: Control of crystallization and aggregation*. Nano Letters, 2002. **2**(10): p. 1149-1155.
76. Scott, D.W., *Thermal Rearrangement of Branched-Chain Methylpolysiloxanes*. Journal of the American Chemical Society, 1946. **68**(3): p. 356-358.
77. Patnode, W. and D.F. Wilcock, *Methylpolysiloxanes*. Journal of the American Chemical Society, 1946. **68**(3): p. 358-363.
78. Barry, A.J., et al., *Crystalline Organosilsesquioxanes*. Journal of the American Chemical Society, 1955. **77**(16): p. 4248-4252.
79. Muller, R., R. Kohne, and S. Sliwinski, *Uber Silikone .47. Ein Definiertes Siloxan Aus Siliciumchloroform*. Journal Fur Praktische Chemie, 1959. **9**(1-2): p. 71-74.
80. Larsson, K., *The Crystal Structure of Octa-(Methylsilsesquioxane) (Ch3sio1.5)8*. Arkiv for Kemi, 1961. **16**(3): p. 203-208.

81. Larsson, K., *A Crystal Structure Investigation of Substituted Octa-(Silsesquioxanes) (Rsio1.5)8 and (Arsio1.5)8*. Arkiv for Kemi, 1961. **16**(3): p. 209-214.
82. Larsson, K., *The Crystal Structure of Octa-(Silsesquioxane) (Hsio1.5)8*. Arkiv for Kemi, 1961. **16**(3): p. 215-219.
83. Brown, J.F. and L.H. Vogt, *Polycondensation of Cyclohexylsilanetriol*. Journal of the American Chemical Society, 1965. **87**(19): p. 4313-&.
84. Feher, F.J., D.A. Newman, and J.F. Walzer, *Silsesquioxanes as Models for Silica Surfaces*. Journal of the American Chemical Society, 1989. **111**(5): p. 1741-1748.
85. Jeon, H.G., P.T. Mather, and T.S. Haddad, *Shape memory and nanostructure in poly(norbornyl-POSS) copolymers*. Polymer International, 2000. **49**(5): p. 453-457.
86. Haddad, T.S., B.D. Viers, and S.H. Phillips, *Polyhedral oligomeric silsesquioxane (POSS)-styrene macromers*. Journal of Inorganic and Organometallic Polymers, 2001. **11**(3): p. 155-164.
87. Lichtenhan, J.D., et al., *Silsesquioxane Siloxane Copolymers from Polyhedral Silsesquioxanes*. Macromolecules, 1993. **26**(8): p. 2141-2142.
88. Marcolli, C. and G. Calzaferri, *Monosubstituted octasilasesquioxanes*. Applied Organometallic Chemistry, 1999. **13**(4): p. 213-226.
89. Shockey, E.G., et al., *Functionalized polyhedral oligosilsesquioxane (POSS) macromers: New graftable POSS hydride, POSS alpha-olefin, POSS epoxy, and POSS chlorosilane macromers and POSS-siloxane triblocks*. Applied Organometallic Chemistry, 1999. **13**(4): p. 311-327.
90. Zhang, C.X., T.J. Bunning, and R.M. Laine, *Synthesis and characterization of liquid crystalline silsesquioxanes*. Chemistry of Materials, 2001. **13**(10): p. 3653-3662.
91. Choi, J., A.F. Yee, and R.M. Laine, *Organic/inorganic hybrid composites from cubic silsesquioxanes. Epoxy resins of octa(dimethylsiloxyethylcyclohexylepoxide) silsesquioxane*. Macromolecules, 2003. **36**(15): p. 5666-5682.
92. Shea, K.J. and D.A. Loy, *Bridged polysilsesquioxanes. Molecular-engineered hybrid organic-inorganic materials*. Chemistry of Materials, 2001. **13**(10): p. 3306-3319.
93. Shea, K.J. and D.A. Loy, *Bridged polysilsesquioxanes: Molecular engineering of hybrid organic-inorganic materials*. Mrs Bulletin, 2001. **26**(5): p. 368-376.
94. Pescarmona, P.P. and T. Maschmeyer, *Oligomeric Silsesquioxanes: Synthesis, Characterization and Selected Applications*. Australian Journal of Chemistry-An International Journal for Chemical Science, 2001. **54**: p. 583-596.
95. Bizet, S., J. Galy, and J.F. Gerard, *Structure-property relationships in organic-inorganic nanomaterials based on methacryl-POSS and dimethacrylate networks*. Macromolecules, 2006. **39**(7): p. 2574-2583.
96. Wright, M.E., et al., *Synthesis and thermal curing of aryl-ethynyl-terminated coPOSS imide oligomers: New inorganic/organic hybrid resins*. Chemistry of Materials, 2003. **15**(1): p. 264-268.
97. Mantz, R.A., et al., *Thermolysis of polyhedral oligomeric silsesquioxane (POSS) macromers and POSS-siloxane copolymers*. Chemistry of Materials, 1996. **8**(6): p. 1250-1259.

98. Zheng, L., et al., *X-ray characterizations of polyethylene polyhedral oligomeric silsesquioxane copolymers*. Macromolecules, 2002. **35**(6): p. 2375-2379.
99. Carroll, J.B., et al., "*Plug and play" polymers. Thermal and X-ray characterizations of noncovalently grafted polyhedral oligomeric silsesquioxane (POSS) - Polystyrene nano-composites*. Macromolecules, 2003. **36**(17): p. 6289-6291.
100. Haddad, T.S., et al. *Hybrid Inorganic/Organic Diblock Copolymers. Nanostructure in Polyhedral Oligomeric Silsesquioxane Polynorbornenes*. in *Mat. Res. Soc. Symp. Proc*. 2000.
101. Kang, J.M., et al., *Highly bright and efficient electroluminescence of new PPV derivatives containing polyhedral oligomeric silsesquioxanes (POSSs) and their blends*. Macromolecules, 2006. **39**(15): p. 4999-5008.
102. Matejka, L., et al., *Epoxy networks reinforced with polyhedral oligomeric silsesquioxanes (POSS). Structure and morphology*. Macromolecules, 2004. **37**(25): p. 9449-9456.
103. Kim, K.-M., K. Adachi, and Y. Chujo, *Polymer hybrids of functionalized silsesquioxanes and organic polymers utilizing the sol-gel reaction of tetramethoxysilane*. Polymer, 2002. **43**(4): p. 1171-1175.
104. Kim, K.M. and Y. Chujo, *Polymer hybrids with functionalized silsesquioxanes via two physical interactions in one system*. Journal of Polymer Science Part a-Polymer Chemistry, 2003. **41**(9): p. 1306-1315.
105. Kim, K.M. and Y. Chujo, *Organic-inorganic hybrid gels having functionalized silsesquioxanes*. Journal of Materials Chemistry, 2003. **13**(6): p. 1384-1391.
106. Ni, Y., S.X. Zheng, and K.M. Nie, *Morphology and thermal properties of inorganic-organic hybrids involving epoxy resin and polyhedral oligomeric silsesquioxanes*. Polymer, 2004. **45**(16): p. 5557-5568.
107. Joshi, M., et al., *Rheological and viscoelastic behavior of HDPE/octamethyl-POSS nano-composites*. Macromolecules, 2006. **39**(5): p. 1839-1849.
108. Heyde, T., et al., *The Crystal and Molecular-Structure of the Symmetrical Silasesquioxane H8si8o12 at 100 K, a Molecular Building Block of Some Zeolites*. Chimia, 1991. **45**(1-2): p. 38-40.
109. Bartsch, M., et al., *Infrared and Raman-Spectra of Octa(Hydridosilasesquioxanes)*. Spectrochimica Acta Part a-Molecular and Biomolecular Spectroscopy, 1991. **47**(11): p. 1627-1629.
110. Bartsch, M., et al., *H8si8o12 - a Model for the Vibrational Structure of Zeolite-A*. Journal of Physical Chemistry, 1994. **98**(11): p. 2817-2831.
111. Bornhauser, P. and G. Calzaferri, *Normal Coordinate Analysis of H8si8o12*. Spectrochimica Acta Part a-Molecular and Biomolecular Spectroscopy, 1990. **46**(7): p. 1045-1056.
112. Aebi, B., et al., *Mass spectra of octaspherosiloxanes*. Rapid Communications in Mass Spectrometry, 1996. **10**(13): p. 1607-1614.
113. Bornhauser, P. and G. Calzaferri, *Ring-opening vibrations of spherosiloxanes*. Journal of Physical Chemistry, 1996. **100**(6): p. 2035-2044.
114. Marcolli, C. and G. Calzaferri, *Vibrational structure of monosubstituted octahydrosilasesquioxanes*. Journal of Physical Chemistry B, 1997. **101**(25): p. 4925-4933.

115. Auner, N., et al., *Structural studies of novel siloxysilsesquioxanes*. European Journal of Inorganic Chemistry, 1999(7): p. 1087-1094.
116. Waddon, A.J. and E.B. Coughlin, *Crystal structure of polyhedral oligomeric silsequioxane (POSS) nano-materials: A study by x-ray diffraction and electron microscopy*. Chemistry of Materials, 2003. **15**(24): p. 4555-4561.
117. Earley, C.W., *A Quantum-Mechanical Investigation of Silsesquioxane Cages*. Journal of Physical Chemistry, 1994. **98**(35): p. 8693-8698.
118. Davidova, I.E., et al., *Theoretical study of silsesquioxane organometallic complex structure and IR spectrum. I. Object of investigation, implemented approaches and construction of molecular models*. Journal of Molecular Structure, 1998. **443**(1-3): p. 67-88.
119. Davidova, I.E., et al., *Theoretical study of silsesquioxane organometallic complex structure and IR spectrum. II Interpretation of the IR spectrum*. Journal of Molecular Structure, 1998. **443**(1-3): p. 89-106.
120. Xiang, K.H., et al., *Theoretical study of structural and electronic properties of H-silsesquioxanes*. Journal of Physical Chemistry B, 1998. **102**(44): p. 8704-8711.
121. Pach, M., R.M. Macrae, and I. Carmichael, *Hydrogen and deuterium atoms in octasilsesquioxanes: Experimental and computational studies*. Journal of the American Chemical Society, 2006. **128**(18): p. 6111-6125.
122. Striolo, A., C. McCabe, and P.T. Cummings, *Effective interactions between polyhedral oligomeric sislesquioxanes dissolved in normal hexadecane from molecular simulation*. Macromolecules, 2005. **38**(21): p. 8950-8959.
123. Capaldi, F.M., G.C. Rutledge, and M.C. Boyce, *Structure and dynamics of blends of polyhedral oligomeric silsesquioxanes and polyethylene by atomistic simulation*. Macromolecules, 2005. **38**(15): p. 6700-6709.
124. Hillson, S.D., et al., *Cages, baskets, ladders, and tubes: Conformational studies of polyhedral oligomeric silsesquioxanes*. Journal of Physical Chemistry A, 2005. **109**(37): p. 8371-8378.
125. Chan, E.R., et al., *Simulations of tetra-tethered organic/inorganic nanocube-polymer assemblies*. Macromolecules, 2005. **38**(14): p. 6168-6180.

Chapter 2

Force Field and Parameterization

2.1 Force field development

MD simulations of molecules combining species that exhibit disparate bonding types are relatively scarce due to the lack of adequate force fields. In polymer-functionalized POSS silicon and oxygen undergo mixed covalent-ionic bonding, whereas carbon and hydrogen exhibit predominantly covalent bonding and long-range dispersive interactions. As mentioned in the previous chapter, most of the simulations were based on force fields that are commonly available in commercial simulation packages, and that have originally been developed for different types of materials. In some respects, these force fields yield unsatisfactory results for POSS systems, such as the drastic overestimation of the melting temperatures [1].

To study the self-assembly process of POSS-alkane hybrid materials, and to determine how bonding inorganic cores affects the resulting structures and properties, I built a force field for POSS nano-composites based on an in-house designed charge-transfer multi-body interaction potential. The greatest challenge for all in-house force fields, usually optimized for a specific system, is the need to address applicability to similar but different structures. Thanks to the collaborating work between McCabe group and Neurock group which suggested that force field developed for one

hydrocarbon/POSS system can be applied to most alkyl silsesquioxane, thus supporting the effort of this thesis to design a force field based hexyl-functionalized POSS [2].

The force field used for the simulations described here was originally developed to model the mixed covalent-ionic bonding in silica [3-5] and has for this purpose been expanded to include terms commonly used to simulate organic polymer molecules. It contains three-body terms to describe the directionality of the covalent bonds and a charge-transfer term that controls the charge polarity within a bond and modulates between covalent and ionic character of this interaction. The charge transfer term also allows for charge redistribution upon rupture or formation of a bond, so that the potential can be used to simulate reactive systems. The single particle energy is expressed as:

$$U_i = q_i \sum_{j\neq i}^{N} \frac{q_j}{4\pi\varepsilon_0 r_{ij}} + \sum_{j=1}^{NC} C_{ij} e^{(\sigma_i+\sigma_j-r_{ij})\cdot\rho_{ij}} + \sum_{j\neq i}^{N} 4\varepsilon_{ij}\left[\left(\frac{\overline{r}_{ij}}{r_{ij}}\right)^{12} - \left(\frac{\overline{r}_{ij}}{r_{ij}}\right)^{6}\right] + \sum_{j=1}^{NC-1}\sum_{k=j+1}^{NC} (\varphi_{ij}+\varphi_{ik})\Lambda_{ijk}$$

$$+ \sum_{i\in\{l,j,k,n\}} \left[B_1(1+\cos\phi_{ljkn}) + B_2(1-\cos 2\phi_{ljkn}) + B_3(1+\cos 3\phi_{ljkn}) + B_4\right] \qquad 2\text{-}1$$

The first term of equation 2-1 describes the Coulomb interactions that exist between every pair of charged atoms. Instead of fixing the point charge on each atom, the charges are calculated during the simulation process according to the charge transfer function, $\zeta_{ij} = \left(1 + e^{b(r_{ij}-a)}\right)^{-1}$, which controls the changes in electron distribution as a function of the interatomic spacing. r_{ij} is the interatomic distance, and *a and* b are adjustable parameters. Accordingly, the charge on each atom is given by

$$q_i = q_i^0 - 2\sum_{j=1}^{NC} \delta_{ij}\zeta_{ij}\,, \qquad 2\text{-}2$$

where q_i^0 is the charge of species *i* in the reference state, and δ_{ij} depends on the polarizability difference between species *i* and *j*. The second term in equation (1) is the Born-Mayer-Huggins expression representing the repulsion between atoms due to the Pauli exclusion principle, with ρ_{ij} defined as the hardness parameter. The third term describes covalent bonding interactions, where $\varphi_{ij} = -C_{ij}\frac{\kappa_{ij}}{\eta_{ij}}\zeta_{ij}e^{\lambda_{ij}}e^{-r_{ij}\eta_{ij}}$ is purely attractive and $\Lambda_{ijk} = e^{-\gamma_{ijk}\left(\theta_{ijk}-\bar{\theta}\right)^2}$ accounts for the directionality of these bonds by constraining the angle θ_{ijk} between the *i*-*j* and *i*-*k* pairs of bonds. Note that the charge transfer function modulates between covalent attractive and ionic interactions and the angular constraints are conditional upon the existence of a covalent bond. The next term in equation 2-1 is the Lennard-Jones potential, which describes dispersive interactions between non-bonded atoms. Specifically for this force field, Lennard-Jones interaction is excluded between atom pairs that experience torsion restriction, i.e., it takes effect only when the two atoms involved are more than three neighbors away, more than four if one atom is hydrogen and more than five neighbors away if both atoms are hydrogen. The last term in equation 2-1 describes four-body torsion interaction about the dihedral angle ϕ_{ljkn}, most commonly used in force fields such as OPLS-AA [6] and TraPPE-EH [7, 8]. The torsion angle potential reaches local minima at the *trans* and *gauche* conformations and gives maximum energy at *cis* conformation. (See Appendix B for a detailed description.)

All other symbols in equation 2-1 represent empirical parameters and their values are given in table 2-1, 2-2 and 2-3. The parameters for the charge and charge transfer term

were optimized based on comparison with the results from first-principles quantum mechanical calculations. The parameters for the repulsive and directionally attractive interactions, i.e., the second and the third terms were optimized in the course of simulating various POSS compounds so as to reproduce experimentally known bond distances and angles, crystalline structures, and vibrational properties. The parameters for the torsion terms Lennard-Jones terms were obtained from references [6-8], while the rest of the parameters are optimized based on trial-and-error process to fit the experiment results.

2.2 Parameter Optimization

Mono-functionalized hexyl-POSS crystal has been well studied through experiment, of which X-ray and infrared spectrum have been reported. Hence it was used for parameter optimization to match the simulation results with experimental results. The simulation box contained 64 mono-functionalized hexyl-POSS molecules. The initial crystal structure is constructed based on coordinates from X-ray diffraction data of the mono-functionalized hexyl POSS crystal [9]. Inside each triclinic $P\bar{1}$ unit cell are two oppositely positioned molecules with the tails pointing to each other. The simulated configuration contains 4×4×2 unit cells. A random velocity obeying a Boltzmann distribution at the target temperature is assigned to each atom. To accommodate the high frequency of the motion of hydrogen atoms, a time step of 0.5 fs was used. The system is then relaxed for about 1 ns with NPT ensemble to ensure that it reaches the energy minimum. In Fig. 2-1 we compare the experimentally determined ideal atomic positions and unit cell shape with a snapshot of simulated crystal structure cooled from 291 K to 5

K. The latter retains a small degree of frozen disorder due to the relatively rapid quenching rate 1 K/ps. In fact, some of the atoms are displaced to the opposite side of the simulation box due to periodic boundary condition. Nevertheless, agreement between experimental and simulated structures is visually apparent; a quantitative analysis of the simulated structure is provided in the next section. The data for structural and spectral analyses were collected and averaged over a period of 100 ps after equilibration. To apply constant pressure, Rahman-Parrinello algorithm [10] is used, which allows for both the size and the shape of the simulation box to change.

Local configurations, including bond distances and bond angles, of the simulated crystal are then measured, reported in table 2-4, and compared to experimental findings [9]. As can be seen from this table, the difference between the simulation and experiment is negligibly small. The largest discrepancy in bond distances occurs in the Si-O bond, with a mere 0.87% overestimate by the simulations. As for the angles, the average bending angles from simulation are very close to experimental values, with the largest difference being 2° for the Si-O-Si angle. The simulated cage diameter is 5.36 Å, compared to 5.356 Å in experiments [9]. Hence, our potential model accurately reproduces molecular level structural features.

The crystal structure can be considered as composed of alternative layers of inorganic POSS cages and organic hydrocarbon chains. In table 2-5 we list the lattice parameters of the crystal structure, comparing simulations and experimental results [9]. The simulation box undergoes some degree of deformation as a result of thermal motion of the atoms. The dimension along c axis, which is approximately perpendicular to the layers matches perfectly well with experiment result, accurately capturing the inter-layer

spacing. As for the cross-sectional area, a small deformation is observed: the a-axis is extended by 0.33% and the b-axis is reduced by 2.78%. Overall, the volume of the unit cell is reduced by 1.44%. The axis angles α, β, and γ follow the same sequence as in experiments, i.e., $\alpha > \gamma > \beta$, with α and γ slightly larger than the experimental values by 2.63% and 3.6%, respectively. As a result, the density of the simulated crystal is 1.571 g/cc, compared to 1.546 g/cc in experiments. As reference, Peng et. al. predicted a density of about 1.3g/cc at 700K [11]. These comparisons reflect the accuracy with which our potential reproduces the crystal structure features. All structural parameters deviate by less than 3% from experiment. Moreover, the optimization of potential parameters was not only based on reproducing structural characteristics but also vibrational properties, as detailed below.

Based on MD simulations by Xia and Landman, the root-mean-squared end-to-end distance for liquid hexane averages 5.596 Å at 334 K [12]. In our simulations, with one end of the carbon chain fixed onto the POSS cage, the root-mean-squared end-to-end distance of the hexyl chain is 6.36 Å at 291 K, noticeably larger than for pure hexane. Compared to pure hexane in the liquid state, the flexibility of the hexyl groups within the POSS lattice is constrained from adopting cis configuration, which explains this difference.

The combined hybrid Compass and TraPPE force field used in their work reproduced structural features of POSS system, but behaved poorly in predicting melting point, indicating inaccurate dynamics description [1]. In comparison, the advantage of our in-house designed force field is optimized to also capture dynamical properties of the

materials system. The crucial test we use is the infrared (IR) spectrum, which we calculated as the Fourier transform of the total dipole moment time correlation function. In Fig. 2-2 we compare IR spectra from experiments [9] and our simulations.

All spectral features are reproduced with good agreement, both in terms of the position and relative intensity of the peaks. Furthermore, in simulations we can easily verify what vibrational modes give rise to each of these spectral features. The most intense peak is located around 1139 cm^{-1} and is assigned to the Si-O-Si asymmetric stretching mode. Compared to the experimental spectrum where five distinct peaks appear within the range from 847 cm^{-1} to 916 cm^{-1}, in the simulated spectrum the δ(Si-H) modes overlap with the n(Si-C) stretching mode to produce a broad absorption band with slightly reduced intensity. The absorption band corresponding to the Si-H stretching mode appears around 2350 cm^{-1} in the simulated spectrum, compared to 2274 cm^{-1} in the experimental one, with comparable width and somewhat lower intensity than observed in the experiment. For all other major absorption bands from the experiment, including the C-H stretching modes, the Si-O-Si symmetric stretching, the O-Si-O bending modes, and the relatively weak CH_2 wagging modes between 1150 cm^{-1} and 1350 cm^{-1}, we find excellent agreement between simulation and experiment. To our knowledge, this is the first calculation of the infrared spectrum for the hexyl-functionalized POSS crystal, and serves as validation of our force field in correctly describing the structural dynamics in such systems. The experimental and simulated absorption of the crystal is reported in table 2-6.

In summary, a force field is tailored to simulate hydrocarbon/POSS systems. The force field is applied to mono-functionalized hexyl POSS crystal and yields good agreement with experiment results in terms of structure and vibrational properties.

Element	σ_i (nm)	n_i	z_i	q_i^0 (ecu)
Si	0.101	8	+4	0
O	0.143	8	-2	0
C	0.095	8	+4	0
H	0.065	2	+1	0

Table 2-1 Force field parameters for elements

Pair	$A_{ij}\left(10^{-19}J\right)$	$\rho_{ij}\left(nm^{-1}\right)$	$\eta_{ij}\left(nm^{-1}\right)$	$\kappa_{ij}\left(nm^{-1}\right)$	$e^{\lambda_{ij}}$	ε_{ij}	$\bar{r}_{ij}(nm)$
Si-Si	0.1000	34.5000	0.00	14.500	0.0000	3.8700×10^{-2}	0.3822
Si-O	0.0550	43.5000	3.60	46.500	30.6760	2.2850×10^{-2}	0.3513
Si-C	0.1900	48.5000	1.10	43.000	1.0834	2.5350×10^{-2}	0.3653
Si-H Si-H3	0.1300	49.5000	2.80	41.500	2.3270	9.0000×10^{-3}	0.3455
O-O	0.1000	35.5000	0.00	10.500	0.0000	2.3650×10^{-2}	0.2940
O-C	0.1800	17.0000	0.00	19.000	0.0000	1.8775×10^{-2}	0.3233
O-H O-H3	0.1800	50.5000	0.00	30.500	0.0000	1.1575×10^{-2}	0.2783
C-C	0.2000	45.0000	1.20	45.500	1.7435	1.5275×10^{-2}	0.3500
C-H C-H3	0.2000	37.3000	0.40	31.000	0.5353	1.0300×10^{-2}	0.3000
H-H H-H3 H3-H3	0.1000	14.5000	0.00	14.500	0.0000	6.9625×10^{-3}	0.2500

Charge transfer	δ_{ij} (ecu)	a (nm)	b $\left(nm^{-1}\right)$
Si-O	-0.194	0.200	57.00
Si-C	-0.06	0.225	105.0
Si-H	-0.023	0.190	75.00
C-C	0.000	0.160	15.00
C-H C-H(3)	0.040	0.140	20.00

Table 2-2 Force field parameters for 2-body interactions

Triplet	$\gamma_{ijk}\left(rad^{-2}\right)$	$\bar{\theta}(rad)$
O-Si-O	0.305	1.892
O-Si-C	0.340	1.941
O-Si-H	0.390	1.911
Si-O-Si	0.162	2.653
Si-C-C	0.480	1.910
Si-C-H	0.480	1.910
C-C-C	0.230	2.094
C-C-H C-C-H3	0.120	2.071
H-C-H H-C-H3	0.330	1.823

Torsion	$B_1\left(10^{-19}J\right)$	$B_2\left(10^{-19}J\right)$	$B_3\left(10^{-19}J\right)$
C-C-C-C	4.9018×10^{-2}	-9.4145×10^{-3}	1.0925×10^{-1}
C-C-C-H3	0.0000	0.0000	1.1791×10^{-1}
H-C-C-H3	0.0000	0.0000	9.8998×10^{-2}

from reference [6]

Table 2-3 Force field parameters for 3-body and 4-body interactions

	Si-O(Å)	Si-C(Å)	Si-H(Å)	C-C(Å)	C-H(Å)	O-Si-O(°)	O-Si-C(°)	Si-O-Si(°)
Exp.	1.606(8)[a]	1.832(4)[a]		1.529[b]	1.09[b]	109.37(45)[a]	110.42(18)[a]	148.52(1.73)[a]
Sim.	1.62	1.82	1.44	1.54	1.10	109.5	109.2	146.6

a from reference [9]; b from reference [7]

Table 2-4 Bonding configuration of mono-hexyl POSS at 291 K

	a (Å)	b (Å)	c (Å)	U (Å^3)	α (°)	β (°)	γ (°)
Exp.	7.7775(9)	7.9747(9)	18.033(2)	1093.5(2)	86.941(13)	79.443(9)	84.378(11)
Sim.	7.8029 ±0.0491	7.7532 ±0.0284	18.0630 ±0.0864	1077.8 ±5.7	89.225 ±0.410	82.305 ±0.456	84.481 ±0.577

Experimental data from reference [9]

Table 2-5 Crystal structure analysis

	Experiment	Simulation
$\nu_{asym}(CH_3)$ / $\nu_{asym}(CH_3)$	2959 / 2930	2834
ν(Si-H)	2274	2350
$\delta(CH_2\text{-Si})$	1407	1504
ν_{asym}(Si-O-Si)	1139	1130
δ(Si-H) / ν(Si-C)	887 / 790	843
ν_{sym}(Si-O-Si)	468	502
δ(O-Si-O)	401	382

Experimental data from reference [9]

Table 2-6 Infrared absorptions (cm^{-1}) of mono-functionalized hexyl-POSS

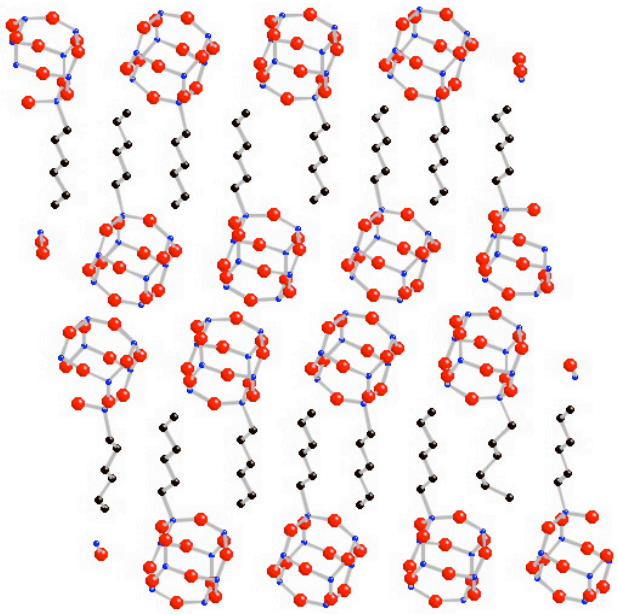

a)

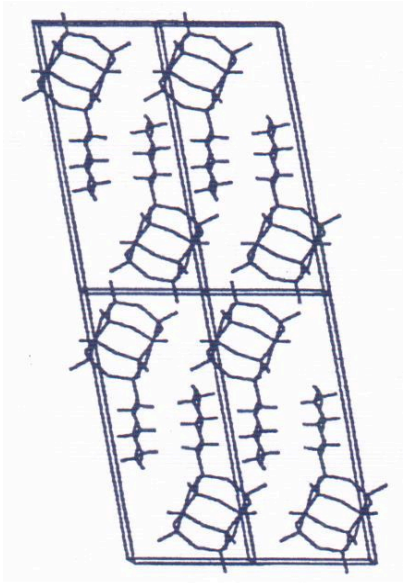

b)

Fig. 2-1 Structure of the mono-teher hexyl POSS crystal: a) snap shot at 5 K from simulation, silicon is blue, oxygen is red, carbon is black, and hydrogen is omitted for clearer appearance; b) sketch from X-ray data in experiment [9]

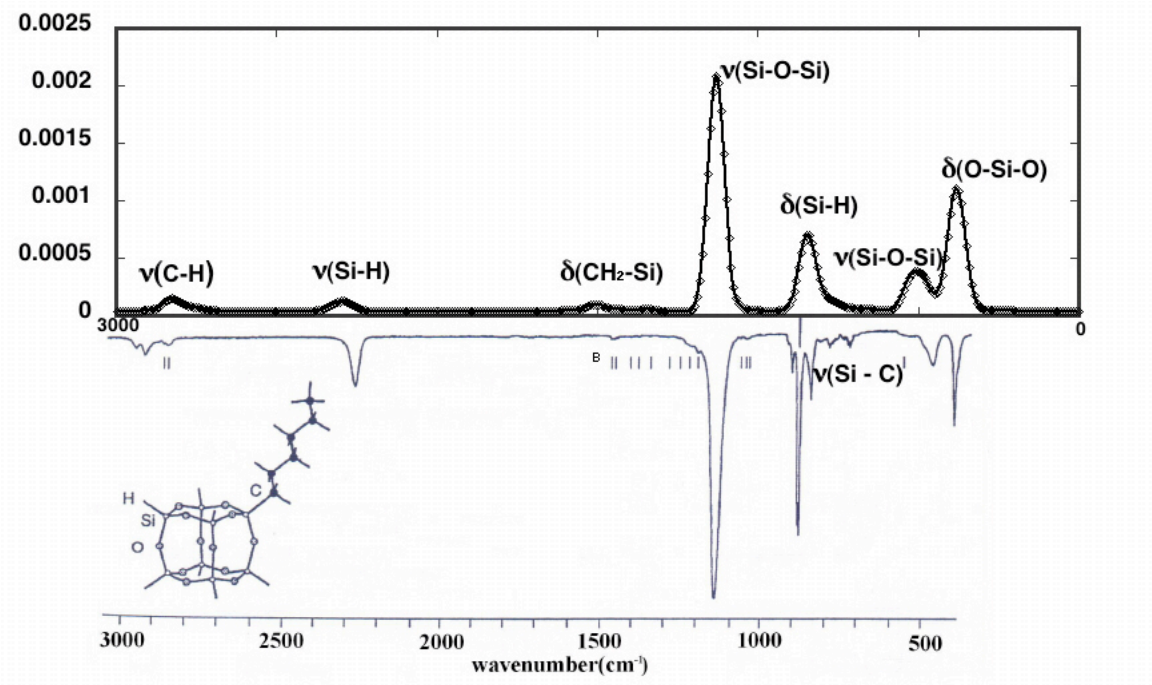

Fig. 2-2 Infrared Spectrum of the mono-functionalized hexyl POSS: top, simulation; bottom, experiment [9]

References

1. Ionescu, T., et al., *Evaluation of Force Fields for Molecular Simulation of Polyhedral Oligomeric Silsesquioxanes*. J. Phys. Chem. B., 2006. **110**: p. 2502-2510.
2. Li, H.-C., et al., *Ab Initio Analysis of the Structural Properties of Alkyl-Substituted Polyhedral Oligomeric Silsesquioxanes*. Journal of Physical Chemistry A, 2007. **111**: p. 3577-3584.
3. Andersen, H.C., *Molecular-Dynamics Simulations at Constant Pressure and-or Temperature*. Journal of Chemical Physics, 1980. **72**(4): p. 2384-2393.
4. Duffrene, L. and J. Kieffer, *Molecular dynamic simulations of the alpha-beta phase transition in silica cristobalite*. Journal of Physics and Chemistry of Solids, 1998. **59**(6-7): p. 1025-1037.
5. Huang, L.P. and J. Kieffer, *Molecular dynamics study of cristobalite silica using a charge transfer three-body potential: Phase transformation and structural disorder*. Journal of Chemical Physics, 2003. **118**(3): p. 1487-1498.
6. Jorgensen, W.L., J.D. Madura, and C.J. Swenson, *Optimized Intermolecular Potential Functions for Liquid Hydrocarbons*. Journal of the American Chemical Society, 1984. **106**(22): p. 6638-6646.
7. Chen, B., M.G. Martin, and J.I. Siepmann, *Thermodynamic properties of the Williams, OPLS-AA, and MMFF94 all-atom force fields for normal alkanes*. Journal of Physical Chemistry B, 1998. **102**(14): p. 2578-2586.
8. Chen, B. and J.I. Siepmann, *Transferable potentials for phase equilibria. 3. Explicit-hydrogen description of normal alkanes*. Journal of Physical Chemistry B, 1999. **103**(25): p. 5370-5379.
9. Calzaferri, G., R. Imhof, and K.W. Tornroos, *Structural and Vibrational Properties of the Octanuclear Silasesquioxane C6h13(H7si8o12)*. Journal of the Chemical Society-Dalton Transactions, 1994(21): p. 3123-3128.
10. Parrinello, M. and A. Rahman, *Polymorphic Transitions in Single-Crystals - a New Molecular-Dynamics Method*. Journal of Applied Physics, 1981. **52**(12): p. 7182-7190.
11. Peng, Y. and C. McCabe, *Molecular Simulation and theoretical modeling of polyhedral oligomeric silsesquioxanes*. Molecular Physics, 2007. **105**(2-3): p. 261-272.
12. Xia, T.K. and U. Landman, *Molecular Evaporation and Condensation of Liquid N-Alkane Films*. Journal of Chemical Physics, 1994. **101**(3): p. 2498-2507.

Chapter 3

Melting and Subsequent Glass Transition of Mono-Functionalized Hexyl-POSS Crystal

3.1 Simulation approach

The in-house force field has been developed and optimized to ascertain adequate performance with respect to the structure and dynamics of crystalline mono-functionalized alkyl-POSS. In this chapter I carry out investigation to explore the structural and dynamic properties of the same system, mono-functionalized hexyl-POSS crystal, during melting and subsequent glass transition for which no experimental data exist yet.

The crystalline configuration of mono-hexyl-POSS, equilibrated at 291 K, served as starting point for a simulated heating and cooling cycle under ambient pressure. The system was heated up to 550 K before subsequently cooled to 150 K. Temperature was ramped at a rate of 1 K/ps, both for heating and cooling. Every 20 K, the system was further relaxed isothermally for 1 ns with NPT ensemble to obtain the equilibrium structure. To accommodate the high frequency of the motion of hydrogen atoms, a time step of 0.5 fs was used.

The data for structural and spectral analyses were collected and averaged over a period of 100 ps after equilibration. While for the initial equilibration of the crystalline configurations we used the Rahman-Parrinello algorithm [1], which allows for shear deformation of the simulation box, the thermal expansion during heating and cooling was captured by the Anderson algorithm [2]. This was indicated because the melting temperature of the system was unknown and because molten configurations, which do not sustain shear deformations, cannot be simulated stably within the Rahman-Parrinello representation. By using the Andersen algorithm, the simulation box is allowed to dilate and contract isotropically, appropriate for the material in the liquid and supercooled liquid states.

As we pointed out in the previous chapter, some of the commercial force fields yield unsatisfactory results for POSS systems with drastic overestimation of the melting temperatures [3]. I will present here that this in-house force field comes up with reasonable prediction of melting point of mono-functionalized hexyl-POSS crystal.

3.2 Results and discussion

To explore the behavior of this system under melting and glass formation, I heated the crystal structure until molten, equilibrated the system at high temperature, and cooled this configuration back down to room temperature. Fig. 3-1 shows the equilibrium volume of the system as a function of temperature. The volume of the system gradually increases with average thermal expansion rate of $5.033 \cdot 10^{-4}$ K^{-1} before the crystal melts. At 430 K, the volume of the system increases sharply, indicating a melting transition. There is no experiment data for the melting point of mono-functionalized POSS. Octa-

functionalized hexyl POSS is reported to have a melting point of about 305 K [4], while for hydrogen-terminated POSS the melting point is 523 K [5]; the predicted melting temperature of mono-functionalizeded POSS is halfway in between. No covalent bonds break during the melting process or while the system is in the liquid state. The structure is further heated as high as 610 K, with the liquid phase expanding at a rate of $1.357 \cdot 10^{-3}$ K^{-1}. Upon cooling, the system remains liquid to as low as 355 K, then the super-cooled liquid goes through a glass transition, marked by the change in the slope of the volume vs. temperature data. The glass has an average thermal expansion coefficient of $3.4699 \cdot 10^{-4}$ K^{-1}, slightly less than the crystal.

Next we examine the melting process in detail. Snapshots of the structures at the transition temperature of 430 K are shown in Fig. 3-2. Just as the system reaches 430 K, without going through relaxation, both POSS cages and hydrocarbon chains are periodically arranged in space, only slightly displaced from their average lattice sites due to thermal motion (Fig. 3-2 a). While pure *n*-hexane melts at 178 K [6], the hexyl chains in this hybrid structure are prevented from leaving lattice sites by being connected to POSS cages. Then as time goes on the structure undergoes a sequence of transitions. According to our simulations, melting is initiated by hydrocarbon chains departing from lattice positions into random directions and becoming entangled with the hydrocarbon chains of neighboring molecules. This stage is apparent after 500 ps, as shown in Fig. 3-2 b. The entropy gain associated with the polymer entanglement gradually overcomes the POSS-POSS interactions. After 800 ps, POSS cages have noticeably rotated about their lattice positions (Fig. 3-2 c), and after 1 ns, noticeable translational disorder has arisen within the POSS sub-lattice (Fig. 3-2 d). By 1.2 ns simulation time, POSS cages

originating from different bi-layers begin to mix (Fig. 3-2 e), and evolve towards an entirely amorphous structure containing small domains of POSS and hydrocarbon, such as is shown for 1.5 ns in Fig. 3-2 f. This sequence of configurational changes coincides with the sharp increase in the V-T curve in Fig. 3-1 a.

We can also observe the different stages of the melting process through various quantitative measures of structural analysis. Fig. 3-3 a shows the cage-cage pair correlation function, calculated based on the coordinates of the cage centers. Curves at different temperatures are shifted along y-axis for clarity. Upon heating the structural correlations between 10 Å and 16 Å gradually attenuate and then abruptly vanish upon melting. In the melt, only the first nearest neighbor peak, which decreases in intensity to about 60% of its room temperature value and shifts from 7.75 Å to 8 Å by 450 K, as well as a feature just below 16 Å prevail. This reveals strongly preferred spacing in the arrangement of POSS cages. The coordination number, defined as the number of POSS cages within the closest distance, can be calculated as follows:

$$N = \int_0^R \frac{4\pi(n-1)r^2 g(r)}{V} dr \qquad 3\text{-}1$$

in which, n is the number of particles of same species, V denotes the volume of the simulation box and g(r) is the calculated pair correlation function. The integration is carried out over spacing distance between 0 and R, the value R determined by the spacing where the first peak of g(r) ends. Here I picked R = 9.8 Å based on the shape of g(r) at 291 K. The coordination number for the crystal structure at 291 K is 8, in line with the visual observation of the structure. In the melts at 430 K, the coordination number

decreases to 7, indicating the reduced preference between POSS cages. The coordination number goes slightly up to 7.2 when the structure is cooled back down to 291 K, a sign of partial recovery of preferred POSS-POSS close arrangement.

During heating the flexibility of the hydrocarbon chain increases as evident from the torsion angle distribution. At 291 K, a small portion of the hexyl chain segments visit the *cis* configuration, as reflected by the small peak at 60°. This peak grows continuously as temperature increases below the melting point, but jumps up abruptly when the structure melts. The end-to-end distance of the hexyl chain is defined as the distance between the silicon atom to which the hexyl chain is attached and which we will refer to as "neck," and the carbon at the other end of the chain, which we will refer to as "tail." The distribution of the neck-to-tail distances shows a sharp peak around 7.72 Å at 291 K; this peak moves to shorter distance and broadens upon heating. Accordingly, the chain becomes increasingly more flexible, even while still constrained within the POSS lattice.

Mean squared displacements of different elements were calculated to assess the their mobility at different temperatures. The mean squared displacement of species at 430 K is plotted in fig. 3-4, on a log-log scale. To quantify the difference in mobility between the organic and inorganic segments of the structure, we compare the displacement of silicon atoms to that of the carbon atom located at the free end of the hydrocarbon chain. In Fig. 3-5, we plot the ratio of instantaneous mean squared displacement at 80 ps, $\left\langle r_{C(6)}^2 \right\rangle \Big/ \left\langle r_{Si}^2 \right\rangle_{80\,\mathrm{ps}}$ vs. temperature. Below the melting temperature of 430 K this quantity represents the ratio of squared vibrational displacements from equilibrium positions, as enter the Debye-Waller factor, and is consistently larger than 2. At 291 K

$\left\langle r_{C(6)}^2 \right\rangle / \left\langle r_{Si}^2 \right\rangle_{80\,\mathrm{ps}}$ is about 2.4 in the crystal, and as the temperature rises this ratio increases to above 3.2, indicating that thermal activation accelerates the displacement of hydrocarbons more than that of the POSS cages. This behavior can be explained as a remnant tendency of the hydrocarbons to melt before crystalline order is abandoned within the sublattice formed by the POSS cages. After the melting temperature of 430 K is surpassed, $\left\langle r_{C(6)}^2 \right\rangle / \left\langle r_{Si}^2 \right\rangle_{80\,\mathrm{ps}}$ abruptly drops below 2 and appears to be converging towards 1 with increasing temperature. The melting of the crystal allows for the POSS cages to catch up with the motion of hydrocarbon chains, i.e., at high temperatures both components of the hybrid molecule migrate as a coupled entity. Hence, Fig. 3-5 illustrates how the hydrocarbons tend to escape from the crystalline order at temperatures below the melting point of the hybrid material, but are prevented from doing so by being bonded to POSS cages that prevail in the crystalline state.

To better identify the local structural rearrangements and certain inherent packing preferences of hexyl-functionalized POSS upon melting and subsequent cooling to the glassy state, we present a series of refined spatial correlation functions in Fig. 3-6. In addition to the "neck" and "tail" atoms, defined above, we refer to the silicon atom diagonally opposed to the neck atom as the "head" atom. The pair correlation functions in Fig. 3-6 are shifted for clarity; the position of the baseline on the vertical axis is commensurate to the temperature of the system.

As can be seen from Fig. 3-6 a, the head-head distribution exhibits sharp peaks before melting. Once the structure is melted, the peaks are broadened and their intensity reduced, but the onset of the first peak remains unchanged. The persistence of this well-

defined distance between heads into the molten state indicates a strong affinity between POSS cages. The long-range features completely disappear in the melt. Both short and long-range features reemerge in the glassy state with smaller magnitudes, implying a partial recovery of the preferred arrangement in the glass. As for tail-tail distributions, instead of showing a definite transition between crystal and melt, the peaks shift and decrease in intensity continuously. The main reason of this continuity is that the hexyl chain attains liquid-like disorder before the melting point. The first peak is around 6 Å in the crystal at 291 K and moves to shorter distance as the temperature rises. It reaches 4 Å in the melt. The close spacing between the ends of the hexyl chains is preserved in the glass, and rather well defined, as indicated by the strong peak. In the crystal, the anti-parallel alignment of hydrocarbon chains imposes the large tail-tail spacing. Once melting destroys this order and the hydrocarbon chains can coil up and closer tail-tail spacings can be achieved. With the onset of the first peak located around 6.5 Å, the head–tail spacing is much larger than head–head or tail–tail spacings in the crystal, as can be seen from Fig. 3-6 c. This reflects the preferred interactions between like species. Upon heating, a shoulder arises at about 430 K and increases in intensity with the increasing temperature, as the favored POSS-POSS and hydrocarbon-hydrocarbon pairings are disrupted by thermal fluctuations. The layered structure of alternating POSS cages and hydrocarbons yields to more homogeneous distribution of these species. The neck–tail correlations in the crystal gradually disappear as the temperature rises and POSS cages begin to rotate. The corresponding peaks in the pair correlation functions disappear upon melting. No particular ordering between necks and tails is evident in the glass.

Fig. 3-3 also shows the cage-cage and torsion angle distributions in the glassy state. The unfavorable *cis* configuration and disordered cage arrangements characteristic of the melts are largely preserved in the glass, and long-range features are partially recovered upon eliminating thermal disorder.

3.3 Conclusion

The melting and glass transition process of the system have been investigated. The system shows a well-defined melting point according to T-V curve. However, qualitative and quantitative structural analysis reveals partial melting of the hydrocarbon domain prior to the disintegration of the lattice formed by POSS cages upon heating. Electrostatic POSS-POSS interactions are markedly attractive, and are responsible for sustained close association and clustering of POSS cages in the molten state. This clustering is accentuated when the system goes through the glass transition upon cooling.

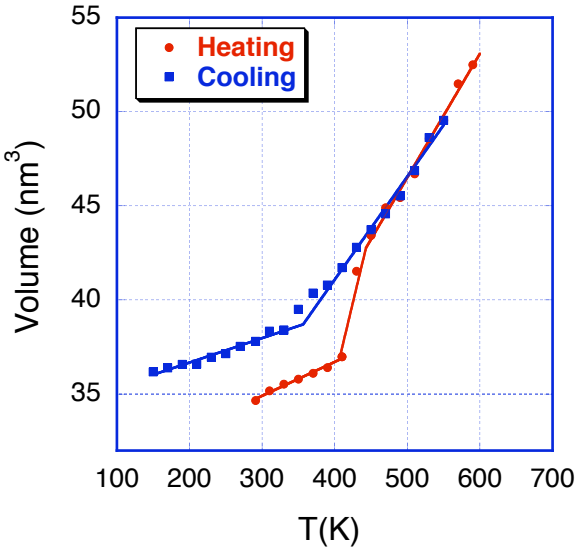

a)

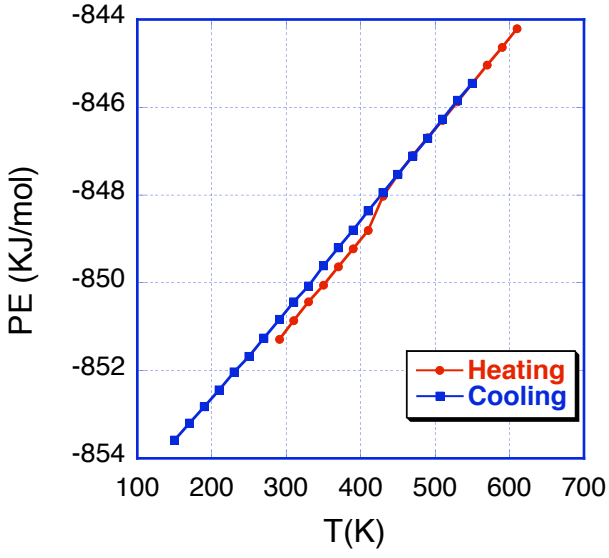

b)

Fig. 3-1 Heating and cooling curves of mono-functionalized hexyl POSS: a), volume; b), potential energy

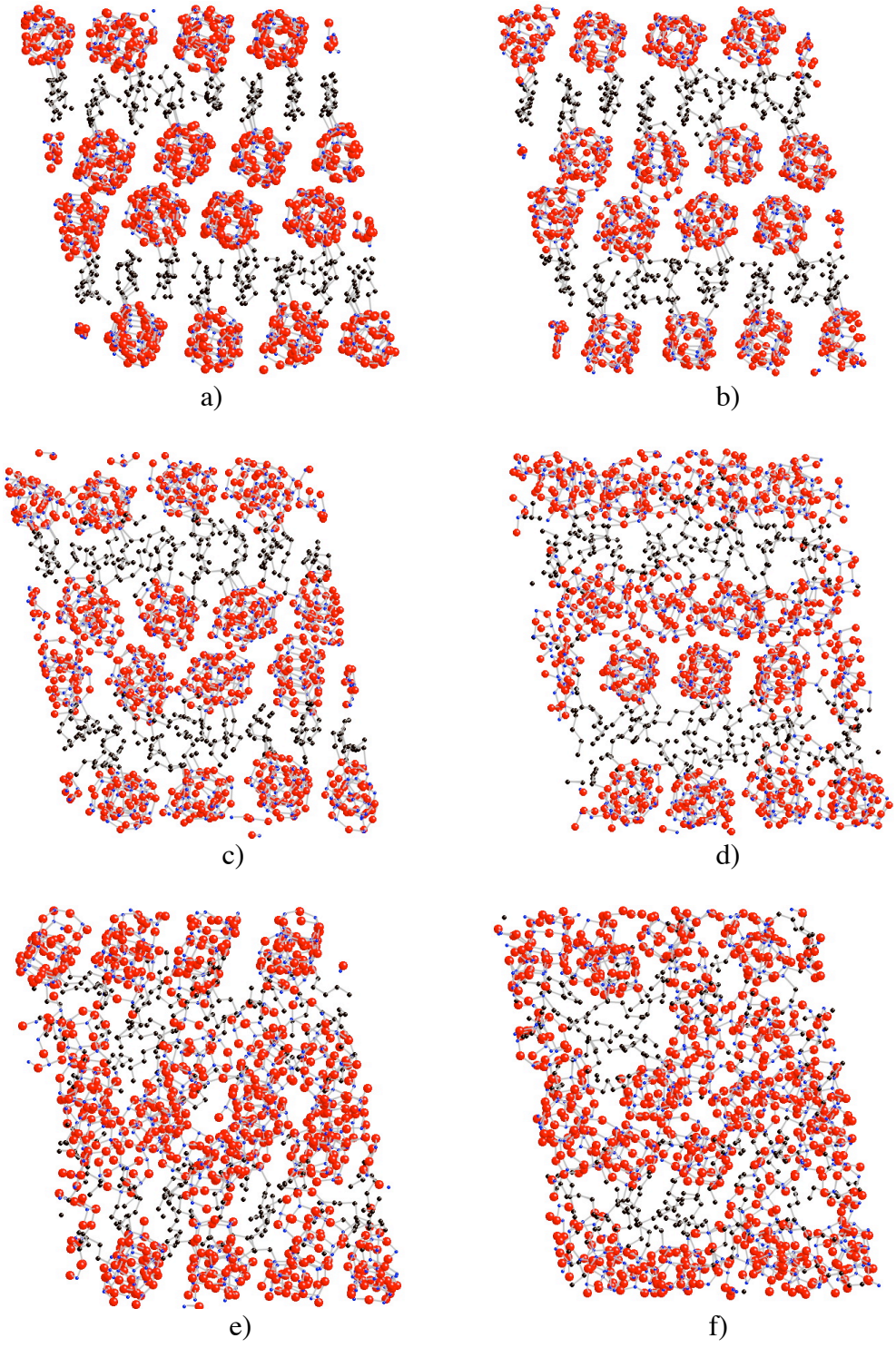

Fig. 3-2 Snapshots of the structures at 430 K. a) 0 ps; b) 500 ps; c) 800 ps; d) 1000 ps; e) 1200 ps; f) 1500 ps

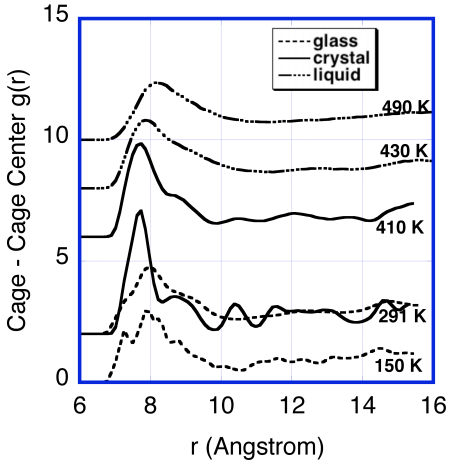

a)

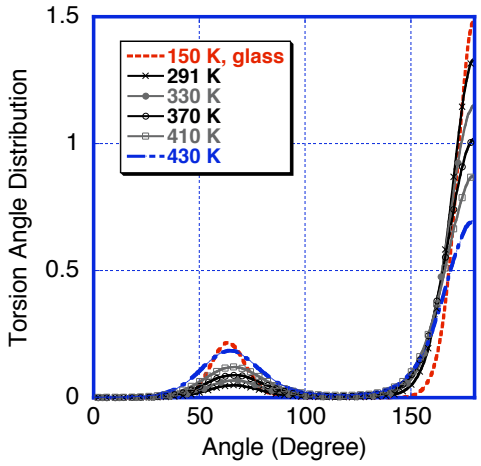

b)

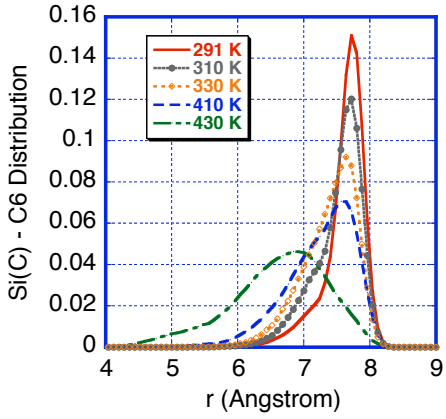

e)

Fig. 3-3 Structural features of hexyl-POSS: a) Cage-center distribution; b) torsion angle distribution; c) distribution of spacing between one silicon atom, Si(C), which is bonded to carbon and the end of the C6 chain

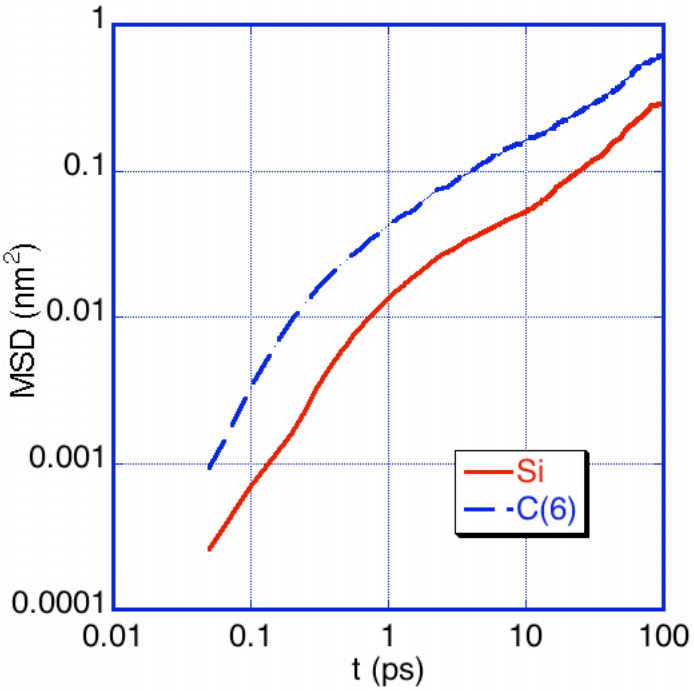

Fig. 3-4 Mean squared displacement at 430 K, of silicon atom and the carbon atom at the end of the hydrocarbon chain

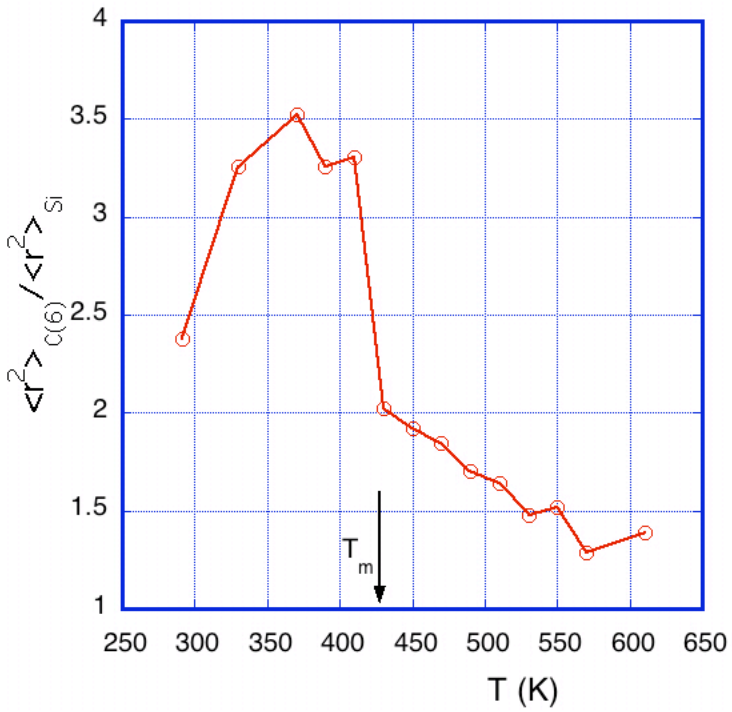

Fig. 3-5 Ratio of instantaneous mean squared displacement of the end carbon to that of silicon at 80 ps, as a function of temperature

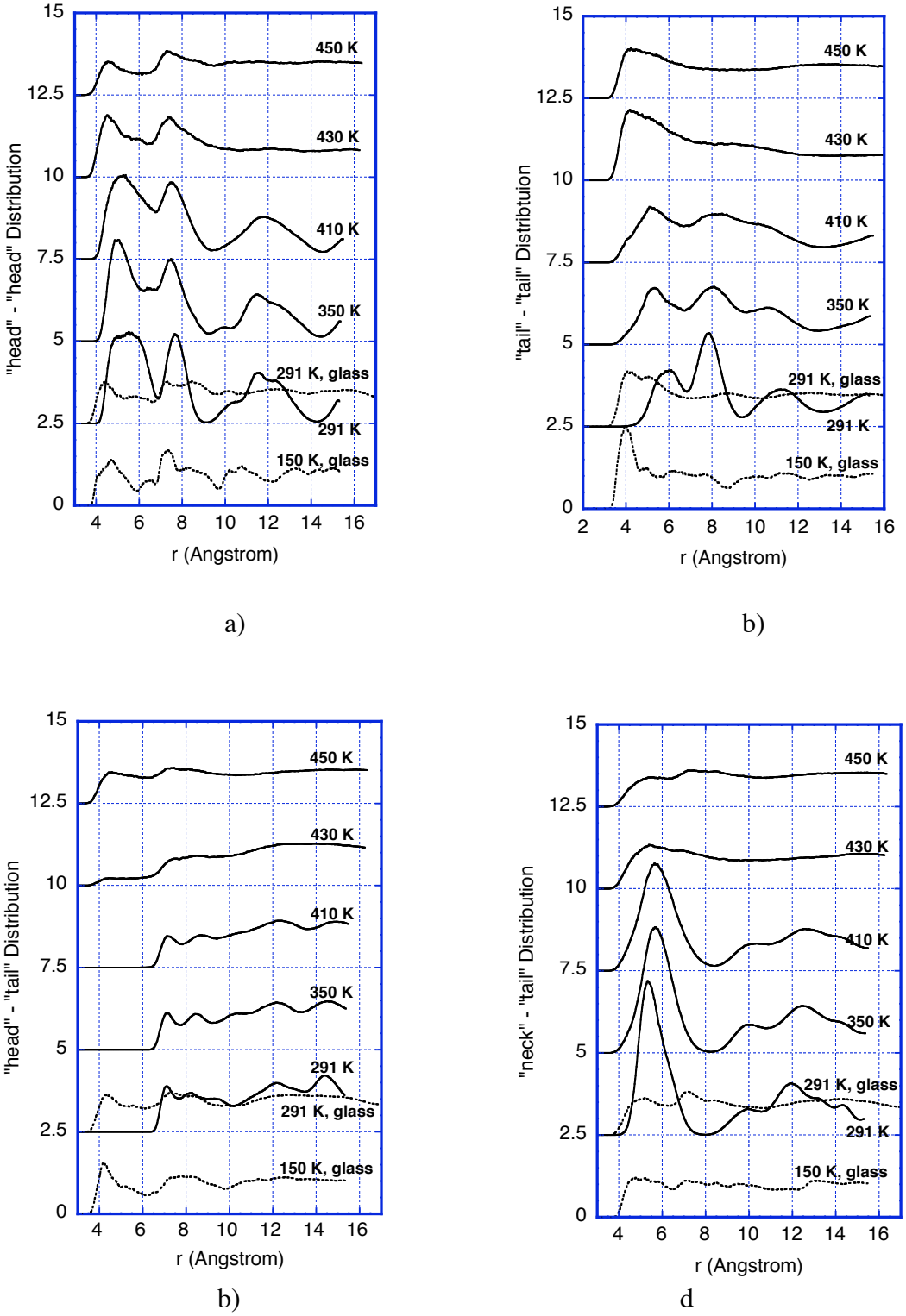

Fig. 3-6 Marker atom distribution: a) head – head correlation distribution; b) tail – tail correlation distribution; c) head – tail correlation distribution; d) neck – tail correlation distribution

References

1. Parrinello, M. and A. Rahman, *Polymorphic Transitions in Single-Crystals - a New Molecular-Dynamics Method*. Journal of Applied Physics, 1981. **52**(12): p. 7182-7190.
2. Andersen, H.C., *Molecular-Dynamics Simulations at Constant Pressure and-or Temperature*. Journal of Chemical Physics, 1980. **72**(4): p. 2384-2393.
3. Ionescu, T., et al., *Evaluation of Force Fields for Molecular Simulation of Polyhedral Oligomeric Silsesquioxanes*. J. Phys. Chem. B., 2006. **110**: p. 2502-2510.
4. Bolln, C., et al., *Thermal properties of the homologous series of 8-fold alkyl-substituted octasilsesquioxanes*. Chemistry of Materials, 1997. **9**(6): p. 1475-1479.
5. Larsson, K., Ark. Kemi, 1960. **16**: p. 215.
6. *http://www.npi.gov.au/databased/substance-info*. 2007.

Chapter 4

Mono-, Di-, and Pendent-Functionalized POSS systems

4.1 Mono-functionalized POSS system

The previous chapter describes extensive studies on one specific mono-substituted system, $H_7Si_8O_{12}$-C_6H_{15}, which were carried out to first derive parameters for the force field we developed for this system, and to subsequently investigate the melting process of the hybrid compound. This chapter contains the study of mono-, di-, and pendent-functionalized POSS systems with varying tether lengths. We conducted these simulations in order to identify the effect of tether length and bonding architecture on the structure and properties of these hybrid materials.

Three different synthetic routes have been employed in experiments to obtain mono-substituted POSS. Trifunctional organo/hydro monomers, in the form of $RSi(OH)_3$ and $HSi(OH)_3$ respectively, can form various heterosubstituted POSS compounds through co-hydrolysis process. When hydro and organo monomers are mixed with 7:1 ratio, the main resulting compounds will be mono-substituted POSS molecules [1, 2]. The second approach starts with incomplete POSS particles, namely POSS cages with only 7 silicon atoms, and produces mono-substituted POSS particles as the only end-products through corner capping reactions [2, 3]. However, due to the instability of the

incomplete POSS particles, the practical use of this approach is limited. The third method, also the most widely used method, is substituting desired organic tethers in place of reactive corners of octa-hydro POSS molecules [2, 4, 5]. All the three routes allow one to easily prepare mono-functionalized POSS with a variety of tethers of varying length. Examples of mono-tethered POSS include silsesquioxane-based amphiphiles [6], the cube-disc shaped POSS material [7], POSS terminated polymer system [8], POSS-silane and POSS-olefin monomers [9], polyimide-chain-end tethered POSS with application for low-dielectric constant materials [10].

In this work, three mono-substituted POSS systems are studied. The functional groups consist of hydrocarbon chains with 5, 9 and 20 carbons respectively. The starting configurations were obtained by duplicating the unit cell that contains one functionalized POSS molecule four times in each crystallographic direction. The systems were first kept at a constant temperature of 600 K and a constant pressure of 100 kPa for about 500 pico seconds, allowing for the structures to relax. After that the systems underwent a cooling process with the temperature decreasing by 0.5 K per pico-second. Configurations of the systems were recorded at temperatures 25 K apart between 550 K and 200 K. At each recorded temperature, the systems experienced a relaxation process for as long as 1 ns to ensure that thermal equilibrium was achieved. Accordingly, we obtained the equilibrium structures for the mono-functionalized POSS compounds with varying tether lengths and under different temperatures. The results of the simulation are discussed in the following paragraphs.

The mass densities of these three systems as a function of temperature during cooling are shown in figure 4-1 a). As expected, the mono-functionalized C20-POSS,

in which a single hydrocarbon chain of 20 carbons is attached to each POSS cage, has the lowest density due to the large percentage of light hydrocarbon atoms incorporated in the POSS matrix. To better understand the structure and porosity of these systems and compare the relative changes that the different systems undergo upon cooling, in figure 4-1 b) we plotted the specific atomic volume of each system, i.e., the volume by Avogadro's number of atoms. At low temperature, the specific volume decreases as the number of carbon atoms in the substituting alkane chain increases, indicating more efficient packing with longer chains. The higher packing efficiency of molecules tethered with longer hydrocarbon chains can be explained by the inability of the shorter chains to fill the space between POSS cages efficiently. Tethered to the POSS cages, the hydrocarbon chains have only limited mobility, and thus cannot closely align with chains tethered to the neighboring POSS cages. Longer chains, on the other hand, possess more degrees of freedom to bend and closely align a larger fraction of their length with other hydrocarbon chains. Thus the free volume can be filled and packing efficiency greatly improved. It is interesting to note, however, that at temperatures above ~400 K, the volume per atom of mono-C9POSS increases drastically and is close to that of mono-C5POSS. Of the systems investigated here, the behavior of C9-POSS stands out, particularly at high temperatures. In the liquid states, the asymptotical thermal expansion coefficient of C9-POSS is $1.659 \cdot 10^{-3}$ K^{-1}, that of C5-POSS is $1.374 \cdot 10^{-3}$ K^{-1}, and that of C20-POSS is $1.367 \cdot 10^{-3}$ K^{-1}. These numbers, calculated from the specific volumes near 500 K are slightly larger than that of C6-POSS, discussed in the previous chapter, probably because of the slower cooling rate, 0.5 K/ps instead of 1 K/ps, we adopted here. We expect the rates of volume change to increase, the slower

the cooling rate, as the system is allowed more time for structural relaxation leading to efficient molecular packing. For the melts, the thermal expansion coefficient reaches a maximum for the C9-POSS system, indicating a changeover in the behavior of the polymer tether. In general, thermal expansion in the liquid state involves both anharmonic effects and structural reorganization. We can assume that hydrocarbon chains assume folded or coiled up configurations at low temperatures, while at high temperatures their segments pivot about C-C bonds and the chains explore a larger volume, giving them on average a larger end-to-end distance. In C5-POSS the overall structure is dominated by the interactions between POSS cages and their reconfiguration. The short 5-membered tethers can be accommodated by the interstices that naturally develop in the network formed by these cages, even though their average end-to-end distance increases. In C20-POSS, the hydrocarbon chains form a matrix in which the POSS cages are embedded. Thermal expansion is controlled by the anharmonicity and reorganization of hydrocarbon molecules. We do not expect a significant unfolding of these long chains between low and high temperatures. Because of the enthalpic and entropic energy gain, these chains maintain their entanglement and resulting dense packing over the entire temperature range. The C9-POSS is on the border between the two behaviors. At low temperatures the POSS network dominates the structure and the hydrocarbon chains fold up within this network's interstices. At high temperatures, the chains unfold, pushing apart the POSS cages, and destroying the dense random packing of these cages. This results in the observed peak thermal expansion for the C9-POSS system in the liquid state, i.e., the most significant structural reorganization.

As the temperature is lowered in glass-forming systems, their structures relax into more densely packed configurations, eliminating free volume to the extent possible. Structural reorganization and optimization of molecular packing end with the glass transition. Below T_g, while a certain amount of free volume prevails, only anharmonic effects contribute to thermal expansion. It is therefore no surprise that at 100 K the thermal expansion coefficient of all three systems have similar values, reduced by nearly an order of magnitude from their high-temperature values: from highest to lowest value, it is $3.524 \cdot 10^{-4}$ K^{-1} for C20-POSS, $2.556 \cdot 10^{-4}$ K^{-1} for C9-POSS, and $2.319 \cdot 10^{-4}$ K^{-1} for C5-POSS. The increasing thermal expansion coefficient and the decreasing volume with increasing length of hydrocarbon chains in the system is in line with the fact that hydrocarbon presents more rapid anharmonic vibration than silicon and oxygen of the POSS particles.

With decreasing temperature, the specific volume vs. temperature curves for the three POSS systems exhibit a distinct change in slope, characteristic of the glass transition process, and that is similar to the behavior observed for C6-POSS described in the previous chapter. Given the high quench rates, ubiquitous to molecular simulation, the glass transition range is spread over several tens of degrees, and T_g is not easy to pinpoint as a kink in the volume vs. temperature curves. Nevertheless, as we did for the case of C6-POSS, we asymptotically fitted the high and low temperature extremes of the volume vs. temperature curves with straight lines, and we determined the glass transition temperatures of the three systems as the intersections of these lines extrapolated towards temperatures intermediate to glass and melt. T_g values so determined are 345 K for C5-POSS, 350 K for C9-POSS and 333 K for C20-POSS.

While the difference between C5-POSS and C9-POSS is small, Tg of C20-POSS is obviously lower indicating a decreasing glass transition temperature with the decreasing percentage of POSS compounds in polymer systems. This observation is consistent with the widely reported enhancement of glass transition temperature in polymers upon incorporation of POSS moieties [11-13].

We now examine the structural characteristics of these systems. In fig 4-2 we plot the pair correlation functions of the center of mass of the POSS cages for the three systems at 250 K and 550 K respectively. Curves are shifted vertically for clarity. At 550 K, all three systems present a first peak around 8.2 Å with similar intensity, indicating no impact of the length of the tethers on the spacing between POSS cages in the melt. When only one corner of the POSS cube is functionalized, POSS cages can approach one another at the remaining seven bare corners. At these high temperatures, POSS particles possess the mobility to circumnavigate their single functionalized corners, hence leading to the same POSS cage spacing for the three systems. Zhang and co-workers observed similar behaviors in their simulations of POSS monomers with organic substitutes of varying length. Although different nano-structured phases developed, the spacing between nearest-neighbor POSS cages remained the same [14]. When cooled to 250 K, the first peak of the pair correlation trajectories shifts slightly to shorter distances; for C5-POSS it appears at 8 Å and for both C9-POSS and C20-POSS at 7.8 Å, a mere 0.2-0.4 Å (or 3-5%) reduction in cage-cage distance compared to their high temperature spacing. Knowing that the size of simulation box shrinks by more than 3 Å from 550 K to 250 K (or 8-10%), it is evident that the cooling process greatly reduces the free volume of the systems while imposing comparably little impact on

minimum distance between POSS cubes. The nearest-neighbor peaks are again of similar height for all three POSS systems, but they are taller than at 550 K, reflecting the enhanced number of POSS cages at close vicinity. The first peak exhibits distinct shoulder towards larger distances, indicating two different nearest-neighbor configurations, possibly imposed by the asymmetry of the single tether configuration and the inability to accommodate the tether efficiently within the interstices between POSS cages. The latter increases from C5- to C9-POSS, commensurate with the height of the shoulder. In our results, the position of the second peak at 250 K varies with the length of tether, it appears at a shorter distance the longer the hydrocarbon chain attached to the POSS cube.

Next, we analyze the structure for the relative placement of the extremities of the functionalized POSS molecules. The definitions for "head" and "tail" are given in chapter 3. The "head"-"head", "head"-"tail" and "tail"-"tail" spatial correlations are plotted in fig. 4-3. At 550 K, the "head"-"head" distribution shows a small peak at around 4.75 Å for all three mono-functionalized POSS systems, as seen in Fig 4-3 a), and a more prominent peak at around 7.5 Å. These curves appear similar to the 'head'-'head' distribution of mono-hexyl-POSS at 450 K, only that the peaks are even less intensive. As we recall that the nearest distance between the centers of the POSS cages at this temperature is around 8.2 Å and the diameter of the POSS cages is 5.36 Å. A close spacing of 2.86 Å would be obtained if the 'head's point directly at each other along a 'head'-'head' centered line-up along the axis defined by 'head' and 'neck'. The actual distance of 4.75 Å means that the 'head's points away from the direct line-up along the axis. To identify the configuration that contributes to the first peak, we recall

that the first peak in crystalline mono-hexyl-POSS corresponds to the POSS cage arrangement where the "head" points to the face or edge of the nearest-neighbor POSS cages. Due to the ionic nature of these particles, this orientation preference is likely caused by the attraction of "head", which is silicon, to the oxygen atoms of the neighboring POSS. This orderly orientation arrangement allows more stable packing of adjacent POSS cages from an atomic interactions point of view. Thus, the weak first peak we observe here is likely what is left of the close line-up between oxygen and silicon from neighboring POSS cubes while most such line-up are disrupted by high temperature.

Note, however, that it is the second peak in these pair correlation functions that is the dominant one. This indicates that the grouping of 'head's adopting the above mentioned orientation is so rare that it behaves as if it is a defect. The second-nearest coordination shell, which contains a larger number of particles, is better defined than the first. The second peak is very close to the spacing of the cube centers.

When the hybrid systems are cooled to 250 K, the first peak for all three systems increases significantly in intensity relative to the second peak (Fig 4-3 b), with that for C20-POSS displaying the biggest increase. Hence the relative increase in the first peak not only reflects the enhanced definition of the aggregates formed by POSS cages as thermal fluctuations diminish, but considerable structural reorganization. Both the first and second peaks also shift to smaller spacing. The intensification of the first peak results from an increasing number of POSS cubes join in the shell of closest neighbor, causing more of the head groups to point inward, bringing them closer to the faces of neighboring cubes, and improving overall packing efficiency. This temperature

dependence of the head-head correlation function represents further evidence for the tendency of POSS cubes to cluster. The fact that the second-nearest "head"-"head" neighbor peak still slightly prevails in magnitude, however, indicates that the strong attraction between POSS cubes not necessarily leads to closed-packed structures but stable cavernous groupings as well.

In "tail"-"tail" distributions at 550 K, all three systems display one weak peak at around 5 Å, as shown in Fig 4-4 a), which reflects little correlation between the spatial arrangement of the tether ends. The curves flatten as the hydrocarbon component increases. There are two possible reasons. The longer the chain, the lower the number of chain ends per unit volume, and hence, the less significant peak in the distribution function. Also a greater length means the chain is more flexible, hence more likely to form a homogeneous and even spatial distribution rather than being segregated. Similarly, to the "head" – "head" distributions, the peaks become more prominent and shift towards shorter distances when the systems are cooled to 250 K (Fig 4-4 b). The nearest-neighbor peaks rise sharply from small r-values, but trail off more gradually towards large r-values, in some cases exhibiting a distinct shoulder. This clearly delineates the closest distance to which two tail groups can approach each other, but also shows a significant degree of dispersion in this spatial arrangement. Most likely, this reflects the various sites along the end of the hydrocarbon chain to which the tail group of another chain can dock. A second peak appears, in the case of C20-POSS also a third peak, indicating the emergence of order upon cooling.

POSS-tether interactions are captured by the "head"-"tail" distributions (Fig 4-5 a and b). The most prominent feature at 550 K is a small peak near 8 Å. A shoulder at

smaller distances shows the closest possible approach between heads and tails, but its magnitude shows that this grouping is not favored at high temperature. Upon cooling, however, this first peak intensifies and even exceeds the second-nearest neighbor peak in intensity, due to a well-defined pairing between heads and tails. To some extent the appearance of this pair correlation functions and their evolution with temperature mirror that of the head-head correlation functions. This can be understood as follows. Evidently the positions of the first two peaks, at high and low temperature, are independent of the chain length. Definition in the head-tail configuration, under these circumstances, can be achieved if the POSS-tether assemblies align in an anti-parallel fashion: tethers next to one another and POSS cubes away from each other, on the opposite sides of the tether trunk. For as long as entropic factors control the structural arrangements, it is between 4 and 19 times more likely for a "head" group to dock along the side of hydrocarbon chain than with an "end" group. Thus spatial coordination between head and tail remains poorly defined. At low temperatures, the van der Waals attractions between hydrocarbons establish more order in this subsystem; hydrocarbon chains increasingly align. Maximum exposure of chains to one another, and thus minimization of the energy due to van der Waals contributions, is achieved when the tail of one chain is positioned in the vicinity of the neck of an adjacent chain, i.e., on the far side of the POSS cube from the head atom, which is at a distance of approximately 4.5 Å. Apparently, the caving in of open POSS clusters promotes these anti-parallel alignments in the hydrocarbon chains.

Based on the above structural analyses, we can establish the following structural model for the mono-tethered POSS-alkane systems: At high temperature, the POSS

cubes form clusters with significant amounts of free volume in their centers. The alkane tethers point away from the cluster, with no particular orientation. At low temperatures, the clusters collapse, allowing for a denser packing of the POSS cubes, and the hydrocarbons each other such that a significant fraction of POSS-alkane units are aligned in an anti-parallel fashion. The length of the tethers appears not to have significant impact on the micro structural features except on porosity at high temperature.

4.2 Pendent POSS system

So far all the systems that we have studied are composed of POSS cubes functionalized with a single organic group, albeit the latter vary in length. These linear structures provide a simplified system to sort out the effects of POSS and polymer on each other. Usually termed as POSS monomers, these linear POSS molecules could further interact with one another or more polymer matrix to form complex structures. One common approach to enable such interactions is to introduce reactive double bonds into the organic chains of the POSS monomer. The polymerization between the organic groups will then automatically incorporate POSS particles into the resulting polymer matrix as dangling attachment. As early as 1995, Lichtenhan et. al. successfully synthesized methacrylate-functionalized POSS monomer with one –C=C- bond in the organic chain, $R_7Si_8O_{12}C_7O_2H_{11}$, where R refers to cyclo-hexyl or cyclo-pentyl corner groups [15]. These monomers then polymerize through bond-opening reactions of the double bonds to form poly-propylene with dangling POSS side groups. Tsuchida and collaborators have also successfully obtained polyethylene and poly-propylene copolymers containing pendent POSS branches [16]. The scheme to synthesize poly-

POSS-ethylene is sketched in figure 4-4. The composition of these pendent POSS copolymers can be adjusted by varying the length of the organic groups in the monomers. The POSS cubes dangling from the copolymers are not dispersed evenly and have a tendency to aggregate [17]. The incorporation of POSS particles in the pendent group can sometimes improve the compatibility of the backbone polymer with other polymers through attractive POSS-polymer interaction [18].

We simulated three pendent POSS copolymers, the compounds resulting from polymerization the tether end groups of mono-tethered C10-POSS, C15-POSS and C20-POSS respectively. Three of these mono-functionalized POSS monomers are connected to a backbone so that their anchor points are one C-C distance apart. The resulting pendent structure is then replicated periodically in space to generate the initial configuration for our simulations. The polymerization scheme and the basic building block configuration are shown in figure 4-8 and 4-9. The pendent poly-POSS-PE copolymer in the unit cell assumes star shape after initial relaxation due to the short backbone chain and the long side chains. The simulation box comprises 16 unit cells with a total of 48 POSS particles incorporated. Similar to the investigation of mono-functionalized POSS, the pendent POSS systems are kept at high temperature to relax before being cooled at 0.5 K per pico second. The density of these pendent POSS systems is measured at temperatures 25 K apart, seen in figure 4-5. As expected, the lower the temperature and the less hydrocarbon components, the higher the mass density of the system. Each pendent POSS copolymer molecule can be seen as a 'cluster' of three POSS-hydrocarbon monomers whose abilities to move apart is constrained due to their bond to the common backbone. At high temperatures, the

pendent system has higher density and is less porous compared to the corresponding mono-tether monomer which moves apart when heated. This is evident in C20-POSS, the only system for which we have investigated both the monomer and the pendent one. When cooled to low temperature, the density of both systems is about the same. The increase in packing density is less for the pendent structure because the tether POSS monomers are already linked up at high temperature. The specific volume per mole of atoms, is also plotted to better compare the packing efficiency of the three pendent POSS systems. By fitting the linear asymptotic behavior of the V-T curves we obtain the thermal expansion coefficients at 500 K. They are $1.059 \cdot 10^{-3}$ K^{-1} for pendent C10-POSS, $1.164 \cdot 10^{-3}$ K^{-1} for pendent C15-POSS and $1.226 \cdot 10^{-3}$ K^{-1} for pendent C20-POSS, all of which smaller than that of the mono-functionalized POSS systems. This finding proves that at high temperatures the pendent systems are less porous than their independent mono-tethered counterparts, since free volume is the main factor to determine thermal expansion coefficient in liquids. The overall packing efficiency is higher the longer the tethers for pendent structure as well, as revealed by the sequence of specific volume over all temperatures. At 125 K the thermal expansion coefficients of the three systems are $2.958 \cdot 10^{-4}$ K^{-1} for pendent C10-POSS, $2.135 \cdot 10^{-4}$ K^{-1} for pendent C15-POSS, and $3.139 \cdot 10^{-4}$ K^{-1} for pendent C20-POSS, respectively. The thermal expansion coefficient of pendent C20-POSS is slightly lower than that of the independent mono-tethered C20-POSS it the glassy state, possibly because the bonding constraint in pendent POSS limits anharmonic vibration. Extrapolating the linear curves at high/low temperatures points to a glass transition temperature of 362 K for

pendent C10-POSS, 343 K for pendent C15-POSS and 354.5 K for pendent C20-POSS, respectively.

Pair correlation functions of the center-of-mass of the POSS cages are plotted in fig. 4-10. There is strong resemblance among the correlation functions of the pendent POSS copolymers of various tether lengths at high temperature. The pendent C10-POSS and pendent C15-POSS show a first peak around 8.14 Å, while the pendent C20-POSS has a first peak at a slightly larger distance of 8.28 Å. Overall the effect of the length of the organic tethers on the distance between nearest POSS cages is negligible. When cooled to 250 K, the first peak of these correlation curves shifts slightly to shorter distances, residing at 7.85 Å for pendent C10-POSS and at 7.99 Å for both pendent C15-POSS and pendent C20-POSS. The reduction in spacing between POSS cages (~3.5%) is disproportional to the reduction of the size of the simulation box (8-10%) due to the fact that the decrease in volume mainly results from eliminating free volume within the systems. Small peaks emerge at larger distances at low temperature, indicating the emergence of intermediate-range order upon cooling. Furthermore, the intensity of the first peak in the cage-cage pair correlation function increases, and a shoulder appears on its right side that is more accentuated the longer the hydrocarbon chain, indicating growing size of clusters formed by POSS cubes. This trend is only observed in pendent structure, not in mono-functionalized POSS monomers. A possible explanation is that the clustering of POSS cages in pendent configuration is constrained by the bonding at the end of hydrocarbon chains. The shorter the hydrocarbon chain, the harder for POSS cages to approach each other and hence, the more limited size of

aggregates. In monomers, POSS cages have no barriers for reaching one another, and hence, the length of the hydrocarbon chains does not affect the size of the cluster.

To further investigate the orientational preference in the spatial arrangement of building blocks, we plotted the "head" – "head" distribution function of the pendent POSS compounds in fig 4-11. At 550 K all three systems exhibit a small peak around 4.6–4.7 Å and a stronger second peak around 7.3 Å. These curves bear strong resemblance to those of mono-functionalized POSS systems. At high temperatures, when POSS systems exhibit liquid behavior, the bonding at the end of the hydrocarbon chains is not likely to affect the orientation of the POSS cages, and thus the spatial configuration of POSS cubes is similar to that of individual tethered POSS molecules. At 250 K, however, the shapes of the "head"–"head" correlation functions of pendent POSS systems deviate from those of mono-functionalized POSS. All three mono-functionalized POSS systems observe two prominent peaks in 'head' – 'head' distribution. In pendent structure, two of the systems, pendent C15-POSS and pendent C20-POSS see a dominant first peak, around 4.3 Å and 4.4 Å, respectively. As we have discussed in the previous section, the first peak corresponds configurations in which the "head" of one POSS cube is pointing towards the edge or face of another, after the POSS cages adopt more compact packing. The pendent C10-POSS is an exception. While the first peak is more intensive than that at 550 K, it is not as tall as the second peak. In this case, the tethering at the tail of the short hydrocarbon chain inhibits the necessary rearrangements of the POSS cubes. These 'head'-'head' correlation functions, together with the observations regarding the cage-cage center distribution, allow us to draw the following conclusions. The fact that alkane chain functionalized

POSS cubes are rigidly connected at the opposite end of tether affects the structural organization of those with short chains more than those with long chains. Long hydrocarbon chains provide POSS cubes with enough flexibility to approach one another so that their behavior is similar to that of individual tethered POSS molecules.

As expected, the 'tail'-'tail' distribution functions are quite different from those of mono-functionalized POSS because some of the 'tails' are chemically bonded. The 'tail' – 'tail' distribution functions presents a very sharp and tall first peak around 2.5 Å and a second smaller peak at 4.5 Å, both at 550 K and 250 K. These peaks correspond to the first and second nearest intra-molecular neighbor distances. The inter-molecule 'tail'-'tail' pairs cannot be easily identified in these correlation functions.

4.3 Di-functionalized POSS system

Both mono-functionalized POSS system and pendent POSS structure have only one corner of the POSS cages bonded to an organic tether. The functionality is directly associated with the complexity of a polymeric system. For example, when functionalizing POSS cages two organic molecules, of the possible configurations encompass three different symmetries: (i) functionalization of neighboring silicon atoms; (ii) functionalization of the silicon atoms diagonally opposed on the face of a POSS cube; and (iii) functionalization of silicon atoms across the body-diagonal of the cube. Based on the relative orientation of the two functional groups, typically organic substitutes, one can expect different assembly behaviors of POSS cages, whether these groups are reactive or simply impose steric constraints. In our research, we investigated simple di-functionalized POSS monomers, with pentane or decane bonded to diagonally opposed corners. The molecules are shown in figure 4-12.

The mass density of the monomers is plotted as a function of temperature in figure 3.10. At 550 K, the densities of the di-pentane and di-decane functionalized POSS systems are comparable, and they are on par with the density of mono-C20-POSS. Towards lower temperatures the density of both systems rapidly increases, with the di-C5-POSS system being generally denser that di-C10-POSS in terms of mass per unit volume. On the other hand, in terms of number density, the sequence is reversed granting the greater packing efficiency to the molecule with the longer tether length. At 50k, the free volume in both systems is greatly reduced. The density of di-C5-POSS is close to that of mono-C9-POSS, which contains similar amount of hydrocarbon. The density of di-C10-POSS is still on par with that of mono-C20-POSS.

As in the systems discussed earlier, the molar volumes as a function of temperature are plotted in figure 4-13 b). Even though di-functionalized C10-POSS contains the same fraction of hydrocarbon component in the system, when compared to mono-functionalized C20-POSS, the molar volume of the former is noticeably larger at 550 K. The fact that one long hydrocarbon chain is replaced by two shorter chains alters the packing efficiency in the system. Shorter chains unfold at higher temperature, while longer chains maintain their entanglement and resulting dense packing because of the enthalpic and entropic energy gain. Similarly but less evidently, di-functionalized C5-POSS occupies a higher volume per mole compared to mono-C9-POSS, which has a slightly smaller but closely matched hydrocarbon concentration. The calculated thermal expansion coefficients are $2.246 \cdot 10^{-3}$ K^{-1} and $1.573 \cdot 10^{-3}$ K^{-1} for di-C5POSS and di-C10POSS respectively at 500 K. Apparently the thermal expansion coefficient of the di-functionalized is higher than that of mono-functionalized or pendent systems,

indicating a higher free volume content in the melts of diagonally di-functionalized POSS hybrids. Based on the thermal expansion coefficients of liquid di-C5-POSS and di-C10-POSS, the longer hydrocarbon chain length reduces the ability to generate free volume with increasing temperature. A similar trend was observed between mono-C9-POSS and mono-C20-POSS. When cooled to low temperature, the free volume is removed and the molar volume of di-C10-POSS is on par with mono-C20-POSS at 50 K. The thermal expansion coefficients of the low-temperature glasses are also reduced to $3.553 \cdot 10^{-4}$ K^{-1} and $3.536 \cdot 10^{-4}$ K^{-1} for di-C5-POSS and di-C10-POSS, respectively. By extrapolating from the asymptotic linear portions of these V-T curves, we determined the glass transition temperatures as 377 K for di-C5POSS and 343.5 K for di-C10POSS. These T_gs are on par with what was observed in other POSS copolymer systems.

As shown in figure 4-11, the two diagonally functionalized POSS systems, di-C5-POSS and di-C10-POSS, exhibit the first peak in the cage-cage center pair correlation function at the same distance, around 8.3 Å at 550 K and 8.0 Å at 250 K. Combining this with our observations regarding mono-functionalized and pendent POSS systems, show again that the spacing between the nearest-neighbor POSS cubes is not affected by the length of the organic substitutes bonded to POSS. Accordingly, when functionalized with at least up to two organic chains, the remaining bare corners of the POSS cages leave sufficient access space for POSS cubes to approach one another. Even though no investigation has carried out, we have a strong suspicion that for POSS cages with four or higher functionality, the length of the organic tether will have a stronger impact on the aggregation behavior of POSS particles.

We also investigated the structural characteristics of POSS systems through 'head','neck' and 'tail' pair correlation functions. It is important to point out that, because the POSS cages are symmetrically functionalized at diagonally opposed corners, we can no longer distinguish between "head" and "neck;" both terms now refer to the same structural feature. The "head"–"head" distribution is plotted for di-functionalized POSS in figure 4-14 a). Unlike for mono-functionalized or pendent POSS, which show a first peak around 4.5 Å for "head"-"head" distribution, di-functionalized POSS exhibits with a very broad first peak at about 7.5 Å, which corresponds to about the spacing where the second peak for the mono- and pendent POSS appears. Hence, as one might expect, the existence of the second hydrocarbon chain blocks the head-to-face approach between two POSS. At 250 K distinct shoulders develop at low inter-atomic spacings, hinting at the orientational preference when POSS clusters become more compact. Also, more peaks appear at larger distances, indicating a intermediate-range order in structure. The "tail"–"tail" correlations function for di-C10 POSS exhibits an intense peak around 4 Å at low temperatures, which does not appear for di-C5-POSS. As the POSS cubes approach one another at the open six corners, the decyl chain in di-C10 POSS is long and flexible enough to allow for the ends of the chains to reach one another, while for di-C5-POSS this not the case.

To understand the overall impact of bonding architectures and tether length on the structural arrangement of the resulting composites, coordination number for different systems is calculated by integrating the pair correlation functions of POSS center distributions:

$$N = \int_0^R \frac{4\pi(n-1)r^2 g(r)}{V} dr \qquad 4\text{-}1$$

in which n is the number of POSS particles in the system and g(r) is the pair correlation function and R is the spacing where g(r) reaches minimum after the first peak. The coordination numbers of various systems at 250 K are recorded in table 4-1. The mono-functionalized systems are showing the showing the highest coordination numbers, indicating greater extent of aggregation than the other two systems. When the tethers are constrained, such as the pendent structure, or when there are more corners blocked by organic substitutes, such as the di-functionalized POSS systems, the aggregation of POSS cages are dampened. Within the same bonding architecture, for both mono- and di- functionalized POSS systems, the longer the tether the lower the coordination numbers. This behavior is expected as POSS cages are more evenly distributed at the presence of larger amount of polymer components. The same trend is not observed in pendent structure probably due to the fact that the physical constraint by shorter chain hampers POSS aggregation even though the smaller amount of polymer components encourages POSS aggregation. Hence the length of the tethers and the bonding architecture have great impact on the aggregation of POSS cages.

4.4 Summary

In this chapter we describe a comprehensive investigation of the structural properties of alkane-functionalized POSS systems. Three types of POSS structures are included: mono-functionalized POSS; pendent POSS structure; and POSS functionalized with two tethers on body diagonal corners. Of all the systems studied, regardless local architecture, the longer the chain the more efficient packing is achieved

as longer chains bend to fill the interstices around POSS cages. The distances between the nearest-neighbor POSS cubes are, however, not affected by the length of the organic functional groups attached to POSS. Due to the availability of open corners, the one or two organic substitutes at the corner of the POSS cages do not prevent them from approaching each other. POSS systems contain significant amounts of free volume at high temperatures and exhibit a glass transition between 300 to 400 K. At low temperatures, the POSS clusters adopt denser packing with increased number of POSS cubes within nearest spacing. Cubes in the cluster arrange with orientational preference: pointing their h'ead's to the faces or edges of other cubes. The packing of pendent POSS structure is constrained by the bonding to the backbone. This is most significantly in the case of shorter chains. POSS cubes with two functionalities observe less efficient packing when compared to the mono-functionalized POSS system with same amount of organic component. The fact that one longer chain are replaced by two shorter chains leaves the chains less flexible and constrained from filling interstices around POSS cubes.

When the functionality increases, the network complexity increases, a bigger simulation system is required to capture the structural features of the network configuration. The amount of calculation will increase exponentially, which makes it difficult for the atomistic level MD simulation to produce any meaningful measurement of structural features. As possible extension of future research, it is, however, possible, to study a small system of multi-functionalized POSS using MD with the sole purpose to obtain inputs for meso-scale simulation. The variables such as spacing between

nearest POSS particles and number of POSS cubes within nearest neighbor shell are useful information when building a coarse-grained model.

Coordination Number	Number of carbon atoms per POSS cage				
	5	9	10	15	20
Mono-functionalized	8.1	7.4			6.4
Di-functionalized			5.9		4.0
Pendent POSS			5.5	6.5	6.3

Table 4-1 Coordination numbers of POSS cages in various POSS systems at 250 K

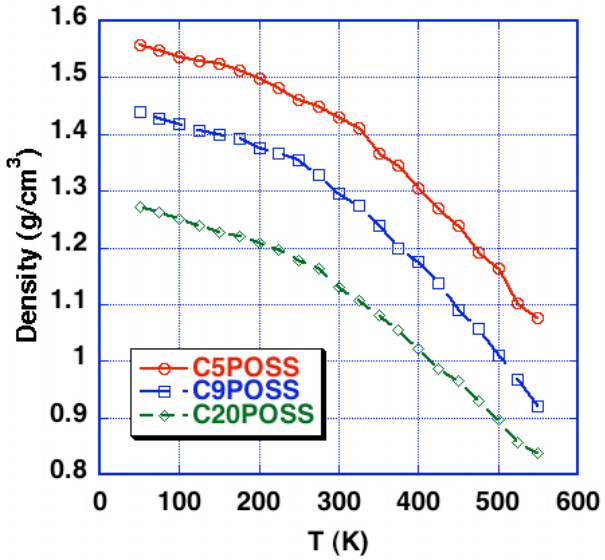

a)

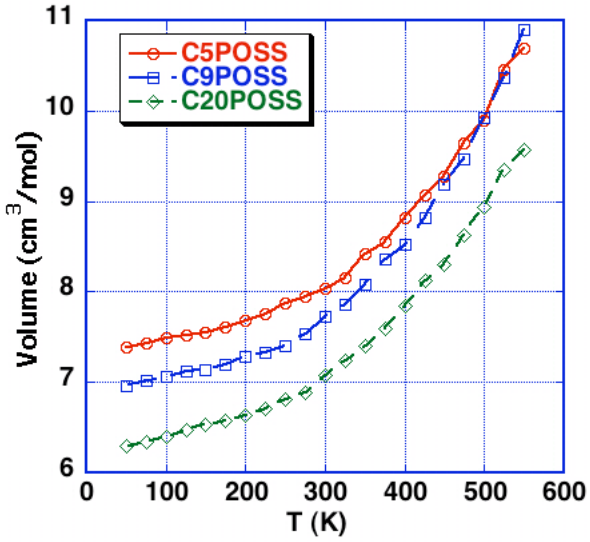

b)

Fig 4-1 a) Density and b) Specific volume of the simulated mono-functionalized POSS systems

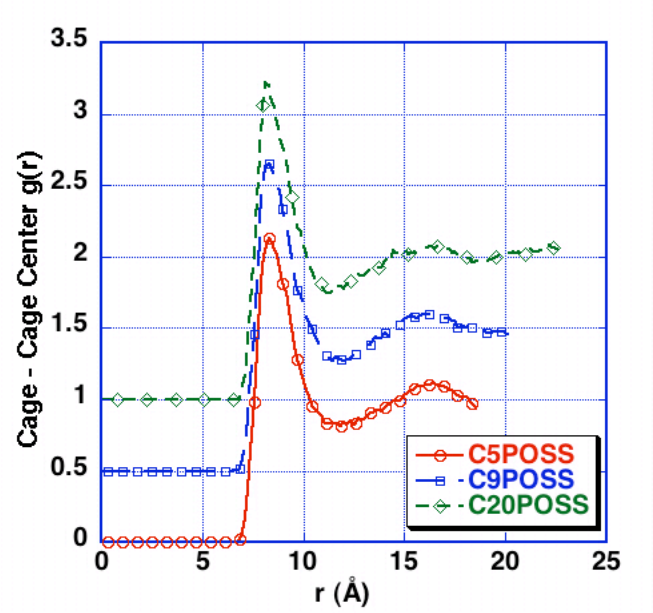

a)

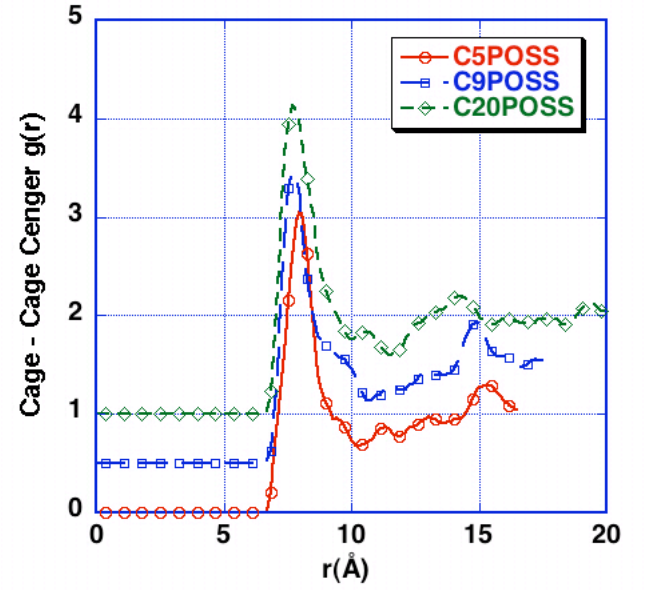

b)

Fig. 4-2 Pair correlation function of POSS-POSS cage centers for the various mono-functionalized POSS systems, (a) at 550 K and (b) at 250 K

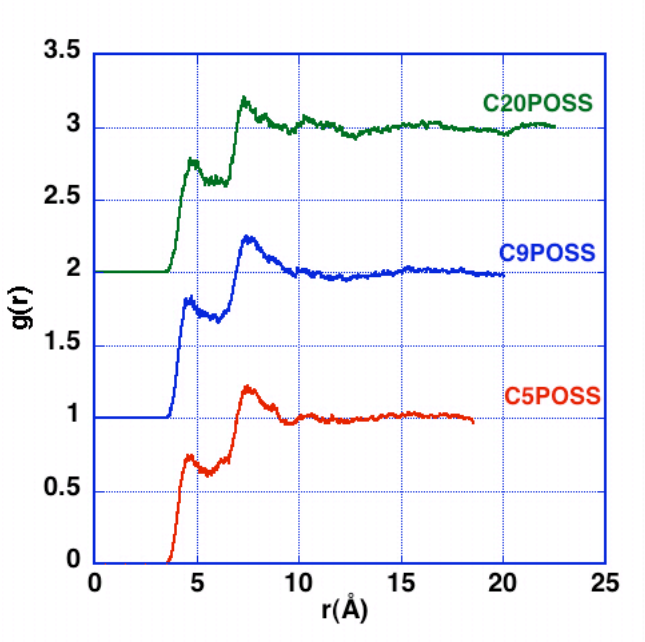

a)

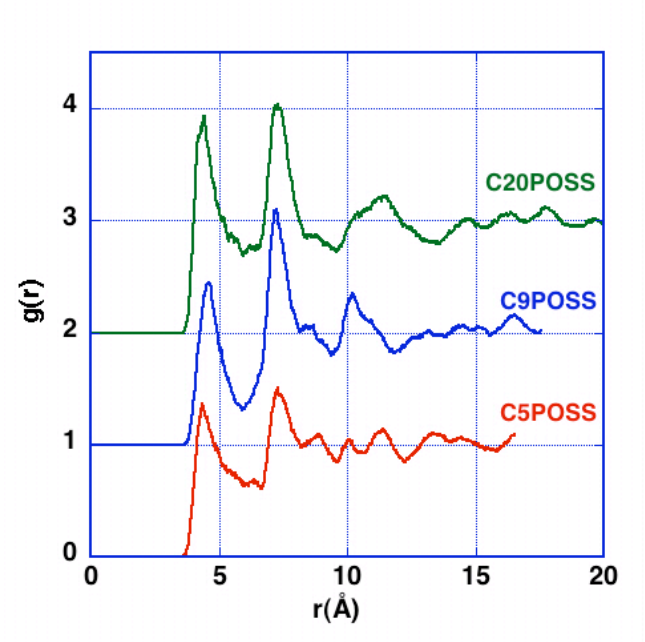

b)

Fig 4-3 “head”-“head” distribution of the three mono-functionalized POSS systems, (a) at 550 K and (b) at 250 K

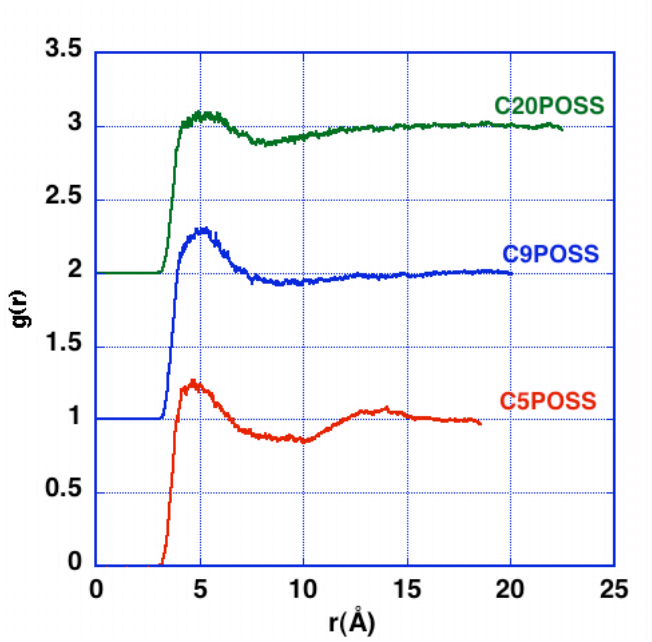

a)

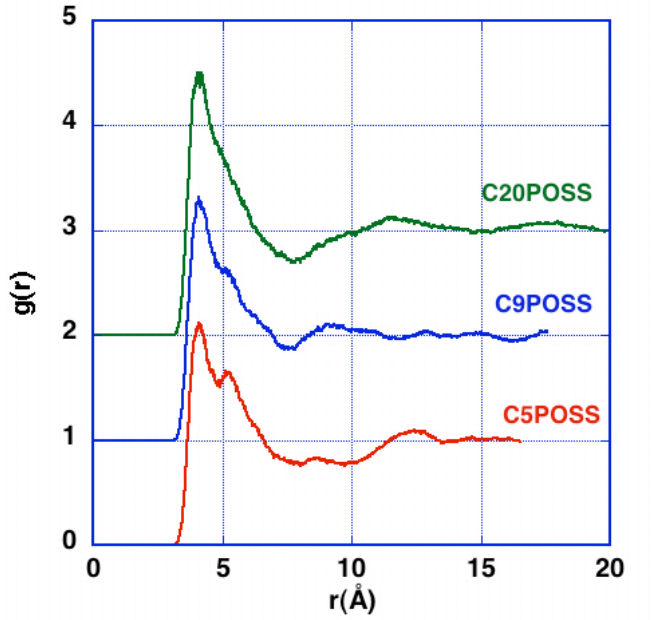

b)

Fig 4-4 "tail"-"tail" distribution of the three mono-functionalized POSS systems, a) at 550 K; b) at 250 K

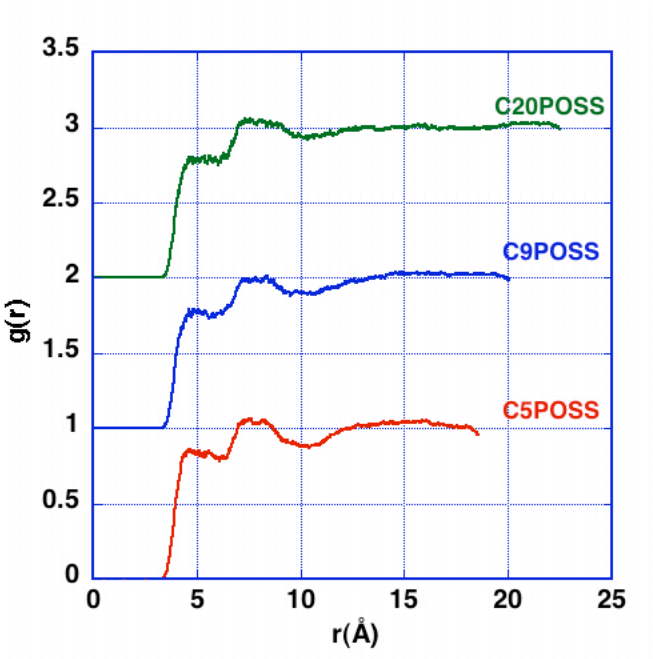

a)

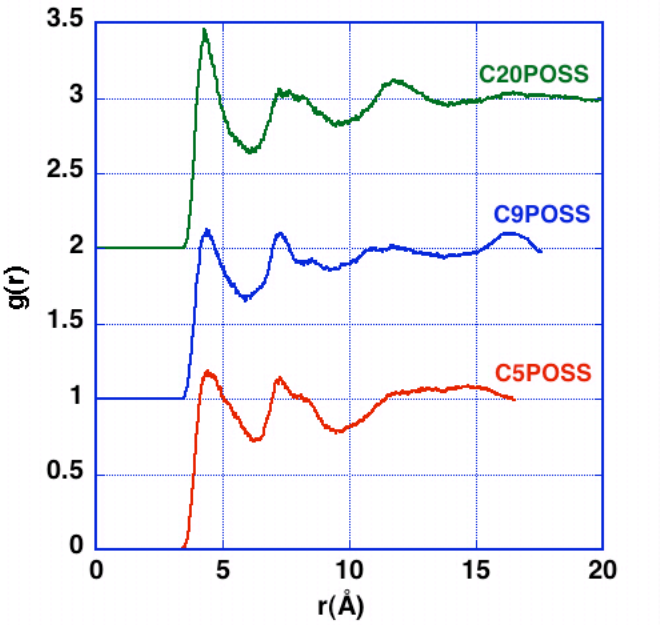

b)

Fig. 4-5 “head”-“tail” distribution of the three mono-functionalized POSS systems, a) at 550 K; b) at 250 K

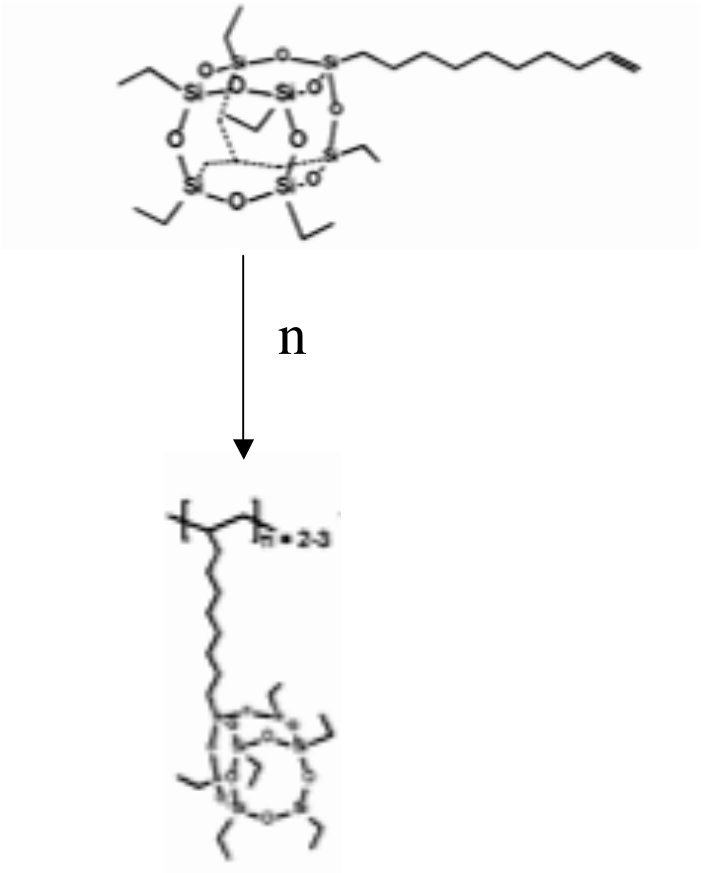

Fig 4-6 Scheme: oligomerization of reactive POSS monomer into pendent POSS copolymer

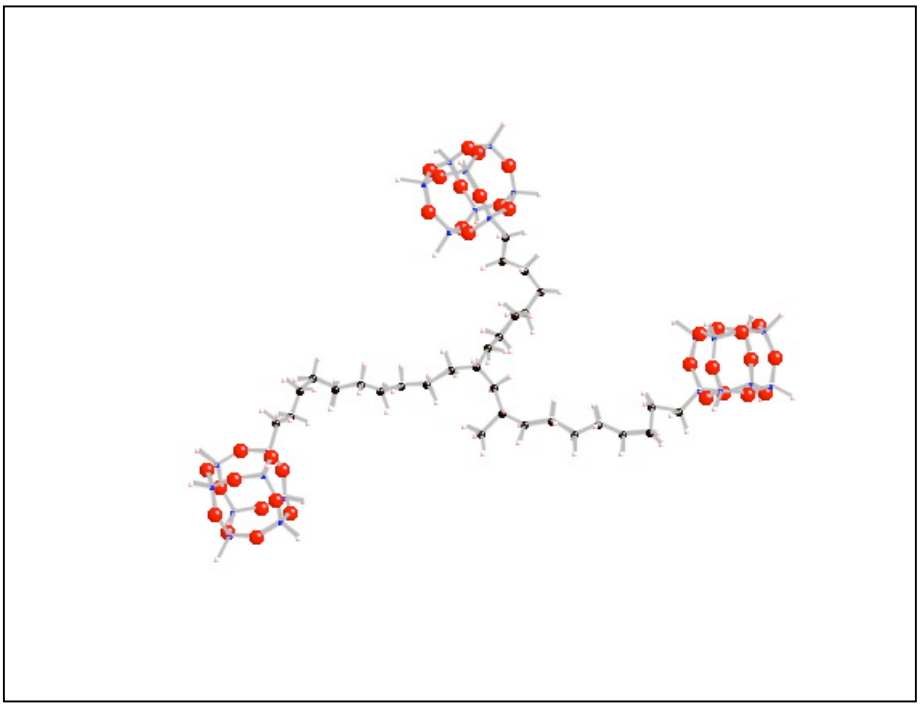

Fig. 4-7 Unit cell of pendent C10-POSS: blue, silicon; red, oxygen; black, carbon; pink, hydrogen

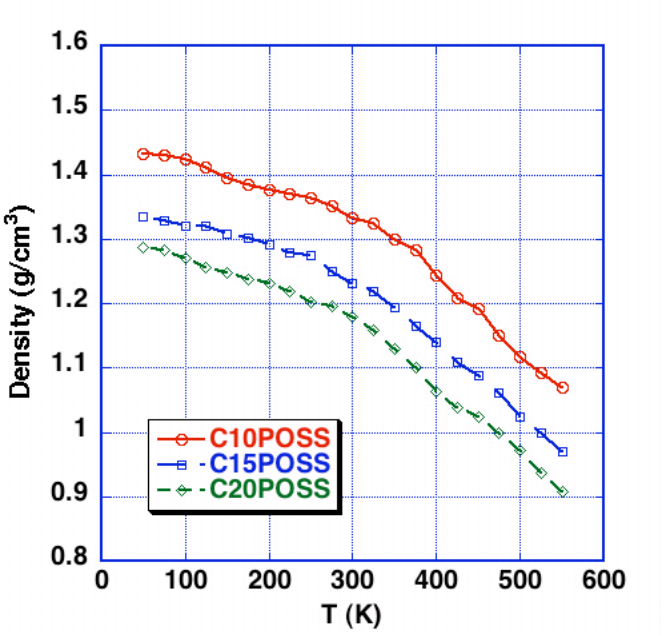

a)

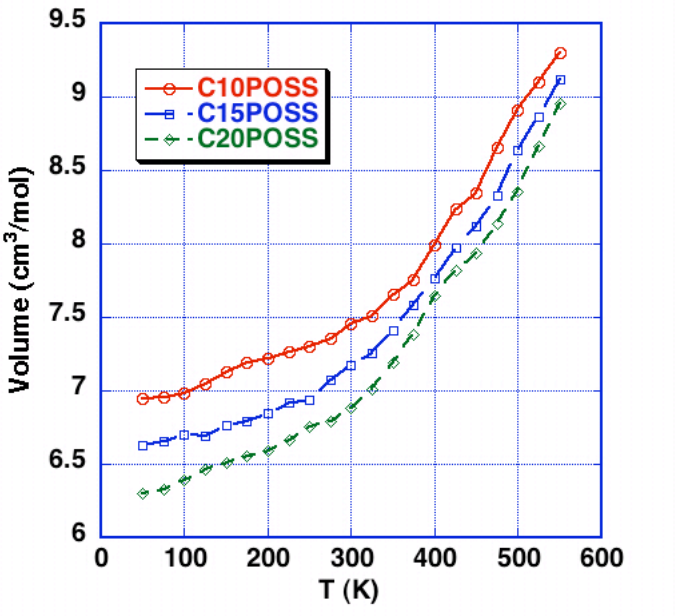

b)

Fig. 4-8 a) Mass density and b) specific volume of the simulated pendent POSS systems

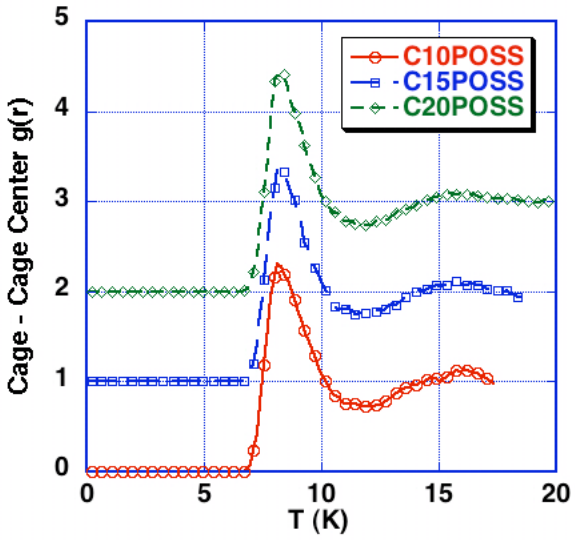

a)

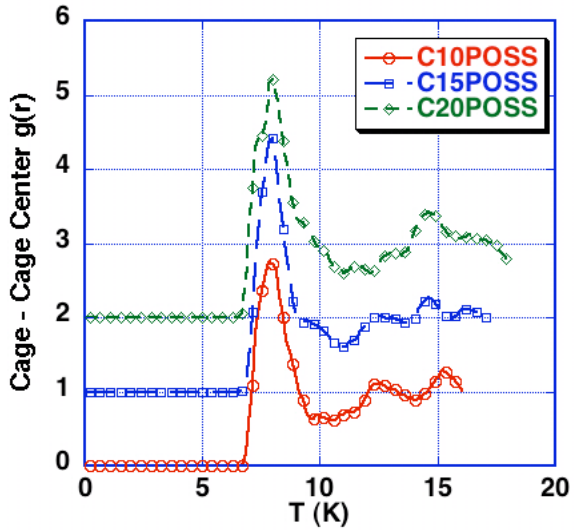

b)

Fig. 4-9 Pair correlation function of pendent POSS compounds, a) at 550 K; b) at 250 K

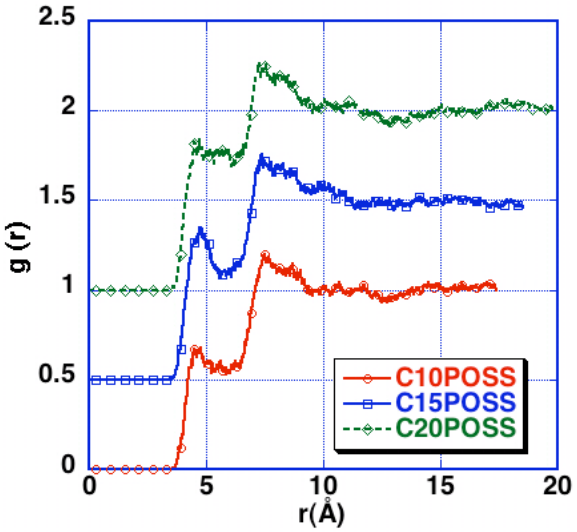

a)

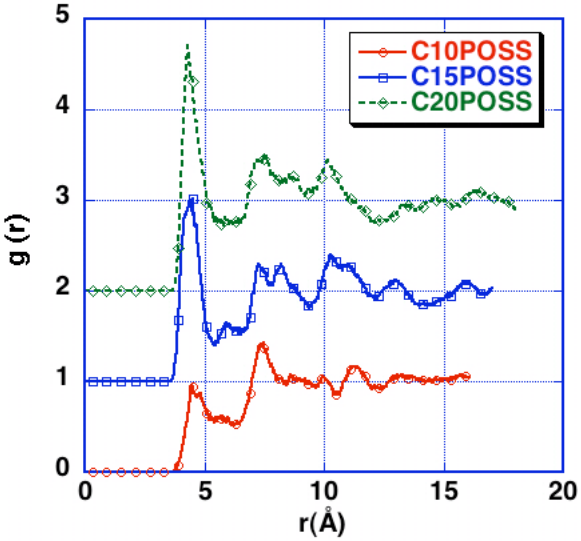

b)

Fig. 4-10 “head”- “head” distribution of pendent POSS compounds, a) at 550 K; b) at 250 K

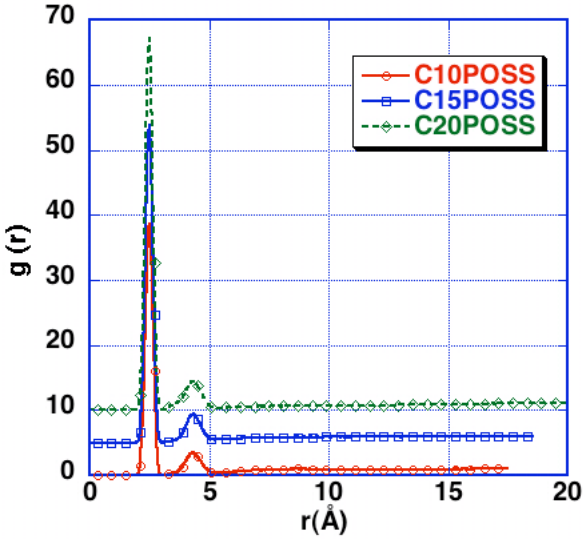

a)

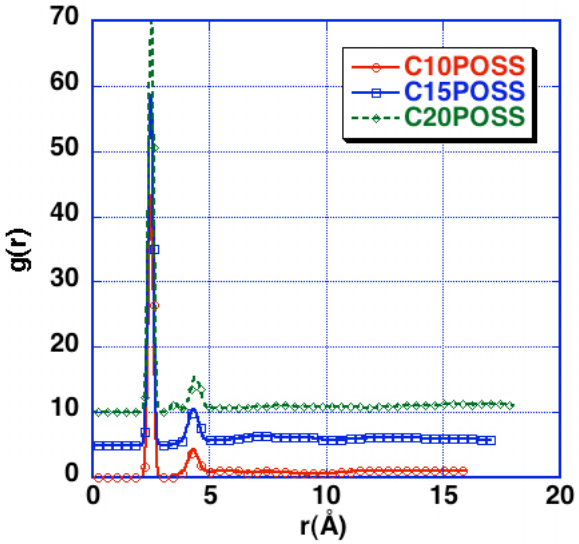

b)

Fig. 4-11 “tail” – “tail” distribution of pendent POSS compounds, a) at 550 K; b) at 250 K

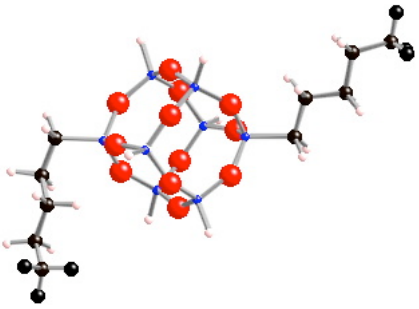

a)

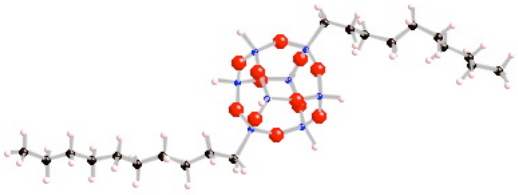

b)

Fig. 4-12 Unit cell of two diagonally bonded POSS molecules, a) POSS with two pentyl chains; b) POSS with two dedcyl chains

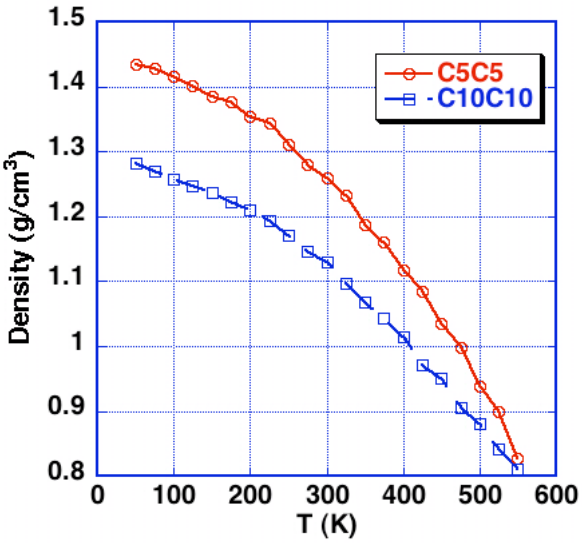

a)

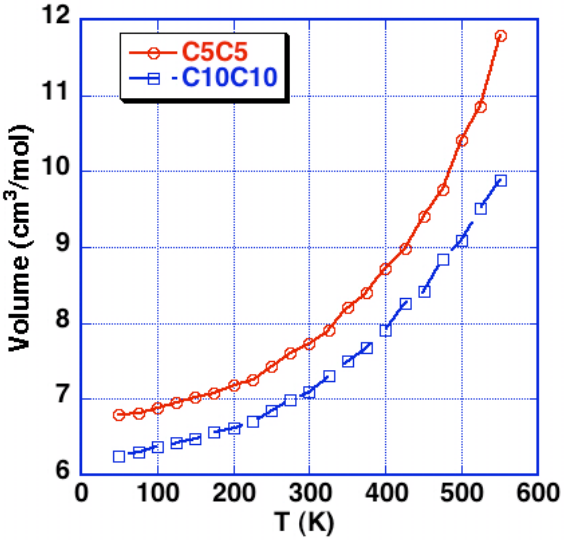

b)

Fig. 4-13 a) Mass density and b) specific volume of diagonally functionalized POSS structure

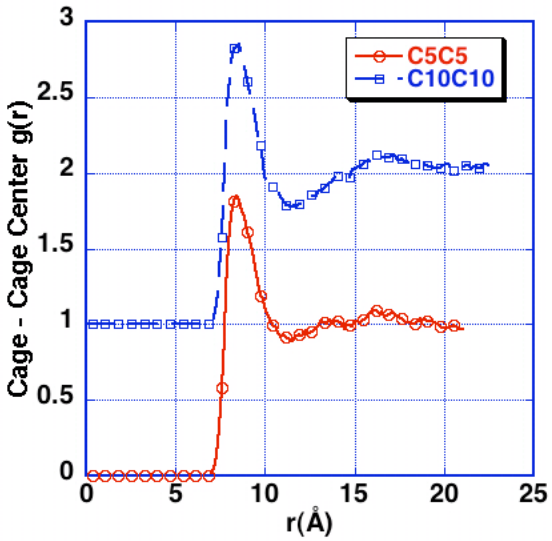

a)

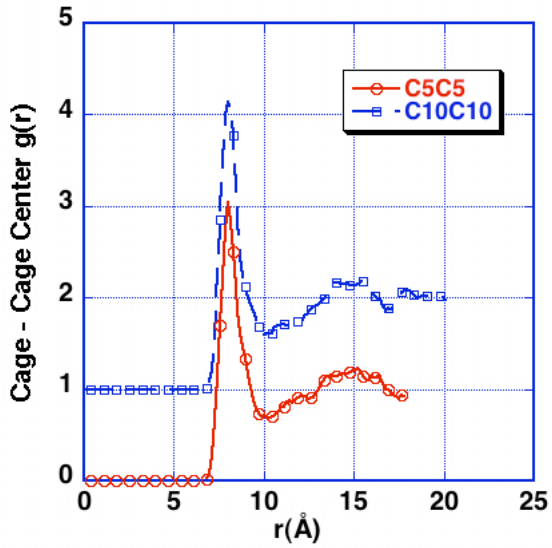

b)

Fig. 4-14 Pair correlation function of di-functionalized POSS, a) at 550 K; b) at 250 K

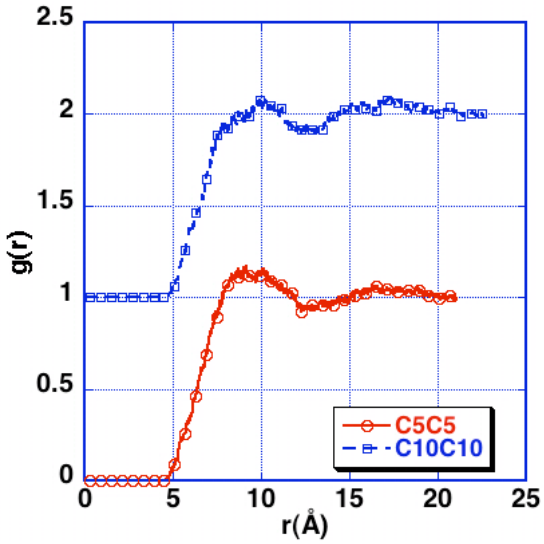

a)

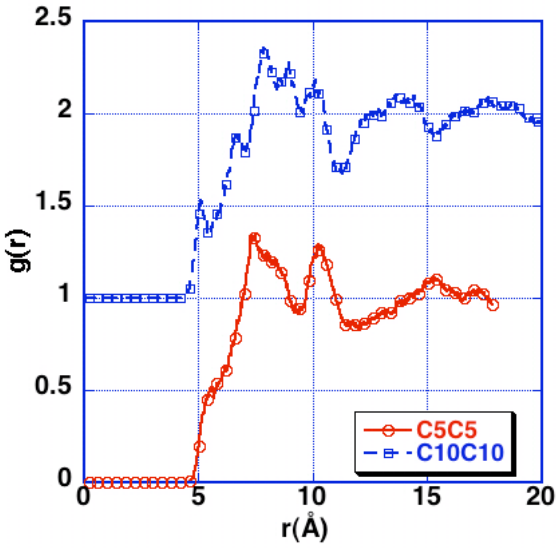

a)

Fig. 4-15 “head” – “head” distribution of di-functionalized POSS, a) at 550 K; b) at 250 K

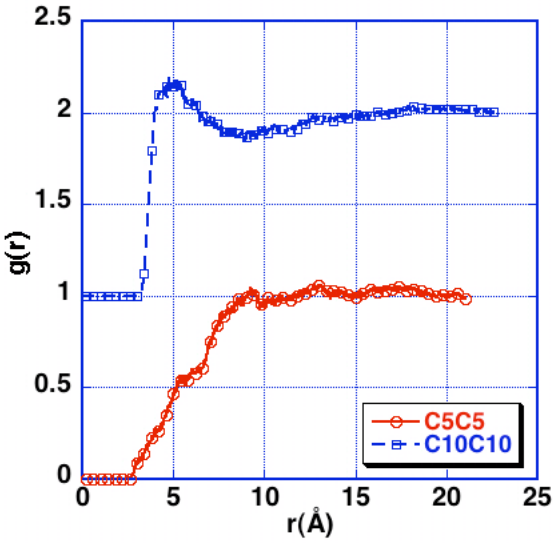

a)

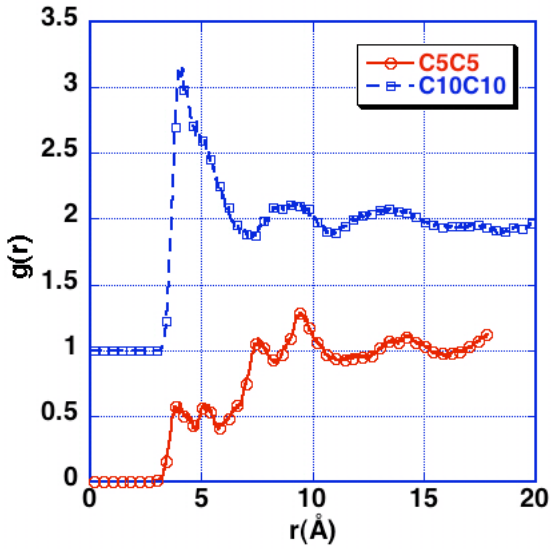

b)

Fig. 4-16 “tail” – “tail” distribution of di-functionalized POSS, a) at 550 K; b) at 250 K

References

1. Calzaferri, G., et al., The monophenylhydrosilasesquioxanes PhH(n-1)Si(n)O(1.5n) where n=8 or 10. Journal of the Chemical Society-Dalton Transactions, 1996(15): p. 3313-3322.
2. Marcolli, C. and G. Calzaferri, Monosubstituted octasilasesquioxanes. Applied Organometallic Chemistry, 1999. 13(4): p. 213-226.
3. Feher, F.J., K.J. Weller, and J.J. Schwab, Reactions of Hydrosilsesquioxanes and Chlorosilsesquioxanes with Phosphoranes. Organometallics, 1995. 14(4): p. 2009-2017.
4. Calzaferri, G. and R. Imhof, Synthesis of the First Organometallic Monosubstituted Octanuclear Silasesquioxane. Dalton Transactions, 1992. 23: p. 3391-3392.
5. Moran, M., et al., Ferrocenyl Substituted Octakis(Dimethylsiloxy)Octasilsesquioxanes - a New Class of Supramolecular Organometallic Compounds - Synthesis, Characterization, and Electrochemistry. Organometallics, 1993. 12(11): p. 4327-4333.
6. Knischka, R., et al., Silsesquioxane-based amphiphiles. Langmuir, 1999. 15(14): p. 4752-4756.
7. Cui, L., et al., Supramolecular self-assembly in a disk-cube dyad molecule based on triphenylene and polyhedral oligomeric silsesquioxane (POSS). Chemistry of Materials, 2006. 18(15): p. 3503-3512.
8. P. T. Mather, K.P.C., T. S. Haddad and J. D. Lichtenhan, Polym. Prepr. (Am. Chm. Soc., Div. Polym. Chem.), 1996. 37: p. 765.
9. Shockey, E.G., et al., Functionalized polyhedral oligosilsesquioxane (POSS) macromers: New graftable POSS hydride, POSS alpha-olefin, POSS epoxy, and POSS chlorosilane macromers and POSS-siloxane triblocks. Applied Organometallic Chemistry, 1999. 13(4): p. 311-327.
10. Leu, C.M., et al., Synthesis and dielectric properties of polyimide-chain-end tethered polyhedral oligomeric silsesquioxane nanocomposites. Chemistry of Materials, 2003. 15(11): p. 2261-2265.
11. Schwab, J.J. and J.D. Lichtenhan, Polyhedral oligomeric silsesquioxane (POSS)-based polymers. Applied Organometallic Chemistry, 1998. 12(10-11): p. 707-713.
12. Xu, H.Y., et al., Preparations, thermal properties, and T-g increase mechanism of inorganic/organic hybrid polymers based on polyhedral oligomeric silsesquioxanes. Macromolecules, 2002. 35(23): p. 8788-8793.
13. Cardoen, G. and E.B. Coughlin, Hemi-telechelic polystyrene-POSS copolymers as model systems for the study of well-defined inorganic/organic hybrid materials. Macromolecules, 2004. 37(13): p. 5123-5126.
14. Zhang, X., E.R. Chan, and S.C. Glotzer, Self-assembled morphologies of monotethered polyhedral oligomeric silsesquioxane nanocubes from computer simulation. Journal of Chemical Physics, 2005. 123(18).
15. Lichtenhan, J.D., Y.A. Otonari, and M.J. Carr, Linear Hybrid Polymer Building-Blocks - Methacrylate- Functionalized Polyhedral Oligomeric Silsesquioxane Monomers and Polymers. Macromolecules, 1995. 28(24): p. 8435-8437.

16. Tsuchida, A., et al., Ethene and propene copolymers containing silsesquioxane side groups. Macromolecules, 1997. 30(10 May 19): p. 2818-2824.
17. Bizet, S., J. Galy, and J.F. Gerard, Structure-property relationships in organic-inorganic nanomaterials based on methacryl-POSS and dimethacrylate networks. Macromolecules, 2006. 39(7): p. 2574-2583.
18. Zhang, W.H., et al., Effect of methyl methacrylate/polyhedral oligomeric silsesquioxane random copolymers in compatibilization of polystyrene and poly(methyl methacrylate) blends. Macromolecules, 2002. 35(21): p. 8029-8038.

Chapter 5

POSS Composites as Candidate of Ion Conductor

5.1 Background

As demonstrated in previous chapters, series of nano-hybrid materials can be formed by reactive interaction between POSS particles and various organic components. Due to the different chemical characteristics that POSS particles and organic components possess inherently, the resulting hybrid compounds are composed of mixture of hard silica segments and soft organic domains. No macro-scale phase separation exists, however, thanks to the chemical bonding between organic and inorganic components. Particles in soft domains have higher mobility while the POSS aggregates provide supportive matrix and enhanced mechanical properties. The perfect juxtaposition of mobility and stability renders this to be an ideal candidate as electrolyte with application in batteries and fuel cells. The properties important to high performance electrolyte include high conductivity, good mechanical properties, and chemical stability [1]. With superb mechanical properties and structural stability, POSS compounds can be turned into a high-performing solid-state ion conductor as long as a ion-conducting mechanism can be developed by utilizing the high mobility of the soft domains of POSS composites.

Today most electrolytes and separator membranes are either made of inorganic acids and their salts or synthesized from doped polymeric or polymer-salt complexes [2]. Both candidates, acid-based and polymer-based electrolytes, possess inherent advantages and disadvantages. Acid-based electrolytes, usually in the form of porous glass, possess superb conductivity [3, 4]. However, they also show high chemical activity and are susceptible to humidity and active chemical agents, which restricts their application [5]. There are two types of polymer electrolytes: polymer-salt, a polymer in which a salt is dissolved which both cations and anions mobile; or polyelectrolyte, a polymer containing charged groups covalently bonded to the polymer with only the counter-ions mobile. As an example of early polymeric electolyte, proton conductor in this case, Nafion (chemical structure shown in Fig. 4-1) invented by DuPont in 1960s need extremely high humidity to exhibit adequate proton conductivity [5]. However, high ion mobility is typically observed in a liquid-like environment, i.e., above the glass transition of a polymeric system, at which point the mechanical integrity of the polymer network as dropped below acceptable levels for this application. It takes a high degree of polymerization to achieve high molecular weight and stable solid-state phase while the existence of free ions imposes negative impact on the polymer chains and leads to extensive degradation [6]. Most polyelectrolytes can only operate at room temperature or below, leaving the practical use of polyelectrolyte limited. Hence, the key to overcoming these limitations is to decouple ion migration from the dynamics of that part of the structure that is responsible for the mechanical stability of the system. Here we attempt to build a novel electrolyte from POSS based hybrids in a bid to solve the dilemma faced by conventional electrolyte. As we have already shown in the preceding

chapters, POSS based copolymer provides a unique way to juxtapose rigid polyhedral structures that provide superb mechanical properties with a more flexible softer phase that can potentially provide excellent conductivity. By functionalizing POSS with organic groups that can act as spacers between cubes and that can donate a charge carrier, an interpenetrating conductive phase can be created in such a hybrid system. Our investigation is the first-ever attempt made to explore the possibility to turn POSS-organo hybrids into electrolytes. Our objective is to develop the basic design criteria for such a hybrid electrolyte using simulation, and identify the most promising materials building blocks to be subsequently synthesized and assembled in the laboratory.

5.2 Simulation-based materials design

As the charge carrier for this study, we chose the Li^+ cation, which is the key element in lithium ion battery technology. We conceived of two contrasting ways of accommodating the presence of Li^+ ions in the system through negatively charged moieties: one is in the form of siloxy group, $-Si-O^- \cdots Li^+$, and the other in the form of carboxyl group, $-C(=O)O^- \cdots Li^+$. Of these, the first one resides at the head section of the POSS cube and the second at the tail end of a hydrocarbon chain tethered to the POSS cube. The latter provides the additional advantage of a variable chain length, creating different degrees of separation between the rigid cage and the conducting part of the structure. In this investigation we compare the behavior of systems based on 5-membered and 20-membered hydrocarbon chains attached to POSS, i.e., in total four different POSS copolymers:

$Li^+ \cdots {}^-O\text{-}(Si_8O_{12}H_6)\text{-}C_5H_{11}$ and $(Si_8O_{12}H_7)\text{-}C_5H_8(=O)O^- \cdots Li^+$

$Li^+ \cdots {}^-O\text{-}(Si_8O_{12}H_6)\text{-}C_{20}H_{41}$ and $(Si_8O_{12}H_7)\text{-}C_{20}H_{38}(=O)O^- \cdots Li^+$

The structures for the shorter of these building blocks are shown in figure 4-2. For brevity, the molecules will be termed as carboxy-C*n*-POSS and siloxy-C*n*-POSS, respectively, where n = 5 or 20. Note that the double bond in the carboxyl group is delocalized, and at any given moment it is not clear which of the two oxygen bears the extra negative charge and which one is connected to carbon via the double bond. To simplify the simulation, these two oxygen atoms are treated using the same in the force field. Each oxygen atom forms one covalent bond with carbon and shares the negative charge, carrying net charge of –0.5 each. In the siloxy-C*n*-POSS the oxygen acts as liaison between silicon and lithium and carries a –1 charge. The soft and flexible hydrocarbon in carboxyl-based C5POSS is expected to accommodate the movement of the ionic bonding while the rigid and bulky POSS particles constrain the ions associated to it in siloxy-based C5POSS. Therefore, carboxyl-based electrolyte is expected to possess superior conductivity with Li^+ serving as the charge carrier. Transport property as represented by diffusion coefficient can be compared to identify the doping methodology more effective in promoting conductivity.

The simulation box is generated by duplicating the unit cell 4 times along each coordinate direction in three-dimensional space, as shown in figure 4-2. The force field described previously is employed to describe the interaction between POSS and hydrocarbon. For the newly introduced lithium-oxygen ionic bonding, however, only part of the force field formula is needed to capture the interaction. Due to the fact that Li^+ forms strong ionic bonds, Li^+ particles are only subject to Coulomb interaction and Pauli exclusion while the effect of covalent bonding and Lennard-Jones interaction is negligible. Hence the three-body angular term, four-body torsion and Lennard-Jones

interaction are taken out to render the simplified force field as described in equation 4-1, which is exactly the first two terms of equation 2-1 in chapter 2:

$$U_i = q_i \sum_{j \neq i}^{N} \frac{q_j}{4\pi\varepsilon_0 r_{ij}} + \sum_{j \neq i}^{NC} A_{ij} e^{(\sigma_i + \sigma_j = r_{ij})\rho_{ij}}, \qquad 4\text{-}1$$

in which r_{ij} is the spacing between two interactive particles. Reardon [7] has developed parameters for Li-O paring under force field 4-1, as reported in table 4-1. For the pairing between Li^+ and other elements, ρ_{ij} is obtained through extrapolation under the guideline: $\rho_{ij} = \sqrt{\rho_{ii} \cdot \rho_{jj}}$, while A_{ij} is obtained through trial-and-error to reproduce average pair spacing between species. All Li^+ parameters are reported in table 4-1.

5.3 Results and Discussion

Simulation runs were carried out with an integration time step of 0.5 fs. Configurations were briefly pre-relaxed at below 100 K before being heated up to 550 K instantaneously under ambient pressure. Systems are then run under NPT ensemble at 550 K for 1 ns or longer, to ensure that the systems reach their equilibrium structure. Snapshots of the two systems are shown in figure 4-3 and 4-4. The strong electrostatic attraction between lithium and oxygen ions brings the ions of the opposite charge in neighboring molecules together to form clusters of –Li-O- in siloxy-based electrolyte, see in figure 4-3 a). To enhance the visibility, we change the color pattern of the elements and dim the color of C5POSS to show the whereabouts of the –Li-O- domains. Lithium is labeled as blue, the oxygen atom that bonds to lithium is labeled as red, and the oxygen in POSS particles is dimmed to light pink, silicon to light blue, and carbon to light

yellow. As known previously, POSS cages tend to approach each other to form aggregates, hence the siloxy groups that reside at their 'head's are trapped inside the POSS aggregates, taking lithium ions along through strong electrostatic force. The positively charged ion and negatively charged siloxy group are also attracted to the oppositely charged groups of neighboring POSS molecules. Therefore –Li-O- clusters form at the core of the POSS aggregates with POSS cages rotating to accommodate this formation. Due to the bulky size of the POSS particles and accordingly the limited number of POSS cages within POSS aggregates, the –Li-O- domains are small in size and are isolated 'island's. Figure 4-3 b) shows the same structure with the hydrocarbon hidden. POSS particles can be seen gathering around the –Li-O- clusters and leaving small voids scattered throughout the structure. Figure 4-3 c) shows the same structure with the hydrocarbon shown, but silicon and oxygen of POSS particles hidden. The hydrogen dangling from POSS particles can still be seen scattered about the system. Hydrocarbon is apparently separate from the –Li-O- domains and fills in the remaining space left between the domains and their surrounding POSS cages. Lithium oxide, with its strong ionic bonding, has a melting point as high as 1840 K. Even though they are not crystalline, the –Li-O- clusters residing in the middle of POSS aggregates are held together through the same strong ionic bonding. Hence the ionic clusters are expected to be the least mobile regions in the system and act as anchoring points to the surrounding structures. The lithium ions, trapped within individual –Li-O- 'island's are unlikely to migrate. The POSS cages, anchored by the –Li-O- domains, experience low mobility as well while the hydrocarbon stick out from the POSS aggregates will enjoy the highest

mobility. The actual measurement of the mobility of different species will be presented later.

Conversely, in carboxyl-based electrolyte, the Li^+ ions are bonded to linear organic chains that are relatively small in size and flexible to either straighten or bend. Lithium ions and carboxyl groups of different C5-POSS molecules are attracted to each other through strong Coulombic interactions. The flexible hydrocarbon chains facilitate the clustering of –Li-O- domains without much constraint. Thus the –Li-O- clusters in carboxyl-based system can grow bigger and eventually form a continuous band or trunk. Visually, from the snapshots of figure 4-4 a), the –Li-O- domain appears as if it is divided into three separate 'island's. However, due to periodic boundary conditions, these three islands are actually connected and form one continuous band. The aggregation of POSS particles seems to be promoted by the existence of Li^+ in the system as the –Li-O- domains push more POSS particles together as shown in figure 4-4 b). Hydrocarbon on the other hand aligns along with the –Li-O- domains as the end of the hydrocarbon chains is anchored to the domains. Similar to the –Li-O- clusters in siloxy bases C5-POSS, the –Li-O- trunk here also offers anchoring points and is expected to be least mobile. The mobility of the hydrocarbon chains are impeded to a great extent due to the fact that they are directly tied to the anchoring –Li-O- trunk. POSS cages, on the other hand are freer as they are farthest away from anchoring points. Unlike the siloxy-based C5-POSS, where the POSS cubes encircling the –Li-O-clusters impose an inherent energy barrier for lithium migration, the –Li-O- trunk in carboxyl-based C5-POSS provides a continuous tunnel where lithium can diffuse between vacant sites within the trunk via hopping mechanism. Noting that the ratio of oxygen and lithium in the trunk is

2 to 1, there are plenty of vacant sites in the trunk for lithium to hop around. Even without further quantitatively examining the structural or dynamic properties of the two systems, one can already guess that the carboxyl-based electrolyte is a superior conductor to the siloxy-based system.

We have also examined the structure quantitatively. To this end, pair correlation functions have been calculated, see figure 4-5. For Li-Li pairing, the first peak appears around 3.9Å in siloxy-based electrolyte and around 4.5Å in carboxyl-based electrolyte. The fact that the closest Li-Li spacing within carboxyl-based system is larger than that of siloxy-based system is indicative of weak ionic bonding between lithium cations and the carboxyl base. Each carboxyl group contains two oxygen atoms that share the negative valence and are composing the –Li-O- domains while in siloxy group the negative valence belongs to only one oxygen atom. The –Li-O- domains in carboxyl-based system contain twice as many oxygen atoms than the siloxy-based electrolyte. The existence of these excessive oxygen atoms also contributes to the larger spacing between closest lithium ions in carboxyl-based electrolyte. The pair correlation function of the siloxy-based system exhibits a weak second nearest lithium neighbor peak at around 5.8 Å. At around 8.5 Å, the curve drops to zero before finally approaching 1 at longer distance. Clusters in the siloxy-based electrolyte are clearly small with only a couple of Li-O pairs, 8.5 Å being a good estimate of average cluster radius. The pair correlation function in carboxyl-based electrolyte slowly decreases with a few weak peaks. However, the curve stays above 0 over the entire spatial range beyond the first peak, which indicates continuous and even distribution of Li^+ in the system, in part due to the migration of Li cations. Together with the snapshots

presented before, we can conclude that Li+ is rather evenly distributed within the –Li-O- band that runs throughout the entire structure. The pair correlation function of Li-O pairs tells a similar story, exhibiting a continuous curve for the carboxyl-based system and a disjointed curve for siloxy-based system respectively.

The insertion of Li^+ ions in the systems greatly alters the structural features of mono-functionalized C5POSS. As in chapter 2 and 3, 'head'-'head' and 'tail'-'tail' distributions are plotted to reveal additional details about the relative orientation of the POSS particles. The 'head'-'head' distribution functions for the carboxyl-based system are shown in figure 4-6. They resemble those of the regular mono-functionalized C5POSS, with two weak peaks at around 4.5 Å and 7.4 Å respectively. However, the height of both the first and second peaks is elevated, indicating higher concentration of 'heads' at close range and accordingly the preferred 'head' to 'head' orientation as a result of 'tails' being anchored by the –Li-O- band. The siloxy-based system presents a distinctively different 'head' – ' head' distribution with a dominant first peak at a larger spacing of around 5.8 Å and a subdued second peak around 10 Å. The POSS particles in the siloxy-based systems are lining up outside of the –Li-O- domains through self assembly and hence the 'head's cannot freely approach each other as they do in regular mono-C5POSS, which explains the larger spacing for the first peak. The second peak corresponds to the distance between 'heads' surrounding different –Li-O- clusters. The 'tail' – 'tail' distribution shows the exactly opposite behavior. The pair correlation function of siloxy-based system appears to be very similar to that of mono-C5POSS, while that of carboxyl-based system presents an intensive first peak around 5.9 Å and a much weaker second peak around 10.6 Å. The strong first peak results from the fact

that the –Li-O- band binds the end of lots hydrocarbon chains together, creating short distance between those chain ends. The second peak reflects the distance between chain ends across the band.

Pair correlation functions of the POSS cage centers are shown in figure 4-7. The curves of both of the systems resemble the shape of the pair correlation function of the regular mono-functionalized C5-POSS with a dominant first peak and a weak second peak. Both the carboxyl-based C5-POSS and the regular mono-functionalized C5-POSS exhibit the first peak around 8.3 Å. The fact that the end of the hydrocarbon chain in the carboxyl-based system is anchored to the –Li-O- trunk does not impact the distance between the closest POSS neighbors, very similar to the pendent structure in which the ends of the hydrocarbon chains are also anchored. Pushed apart by the –Li-O- clusters in the middle, POSS cages in the siloxy-based system exhibit a nearest-neighbor spacing that is slightly larger, i.e., 8.8 Å. The coordination numbers are calculated based on the pair correlation functions at 550 K and are shown in table 5-2. The coordination numbers of the two electrolyte systems are higher than that of regular mono-functionalized C5-POSS. Accordingly, the formation of the –Li-O- cluster and –Li-O- band promotes the aggregation of POSS cages, and hence more POSS cages are pushed into a close-packed grouping. In both carboxyl-based and siloxy-based systems, beyond the first peak g(r) reaches minimum at a larger spacing, another indication of the greater extent of aggregation.

So far the structural features of those two systems have been carefully examined. Next the dynamic properties will be studied by calculating the mean squared displacement (MSD) of the elements in the systems under NVT conditions. The MSD

of the elements in the carboxyl- and siloxy-based systems, shown in figure 4-8, reflect quite different vibration and migration patterns.

When MSD is plotted on a log-log scale, the curves for both diffusive and non-diffusive species exhibit an onset at very short times with a slope exceeding 1, which represents the ballistic regime corresponding to the thermal vibrations of particles with their nearest-neighbor coordination shell. At long times, cures for non-diffusive species will level at a plateau value, oftentimes associated with the Debye-Waller factor that describes the thermal broadening in diffraction measurements. MSDs for particles that migrate via Brownian motion exhibit a diffusive regime characterized by a slope of 1. At low temperatures it may take a long time before species reach their diffusive regime. Due to computational limitation we were only able to measure the MSD for as long as 200 ps. On this scale, most of the MSD curves shown in fig. 4-8 exhibit a long-time asymptotic slope of close to 0.5, indicating some level of aperiodic displacements but not diffusive motion. This is probably due to the fact that the motion of all particles are constrained based on the covalent bonds that connect them; those species that are closest to the anchor points have the smallest mobility, while those farthest away have the largest. In the siloxy-based system, the MSDs of all elements gradually approach this square root dependence on time and show no signs of diffusion. Lithium and the oxygen that bonds to lithium have the smallest mobility while the curves of silicon and oxygen from POSS particles are slightly above them. As I have predicted when analyzing the structural features of siloxy-based C5-POSS, the clusters confined within POSS aggregates in siloxy-based systems act as anchoring points due to the strong ionic bonding within the cluster. POSS particles, residing on the perimeter of the –Li-O-

clusters, enjoy slightly larger degree of freedom but are still anchored to the –Li-O- domains. Hydrocarbon, therefore, has the greatest freedom of motion in the siloxy-based system. The MSD curves of silicon and oxygen overlap, because the migration of these two species is coupled. The same is true for the hydrocarbon and the curves of lithium and non-bridging oxygen are more or less correlated as well. Hence the conclusion is that in siloxy-based systems, lithium cations are confined in small isolated clusters and cannot migrate over long distances within the system.

In the carboxyl-based system, the continuous –Li-O- band behaves as anchoring points and impedes carbon and the non-bridging oxygen from achieving high mobility. POSS particles, dangling away from the band, are free to experience thermal vibrations and exhibit larger displacements than carbon. With carbon pinned by the –Li-O- band, the motion of hydrogen is decoupled from the carbon due to its small weight and high frequency vibration. Lithium shows a distinctly different MSD than all the other elements. De-coupled from the non-bridging oxygen near to which it resides, lithium moves slower than hydrogen at short times due to relatively smaller ampitude of thermal vibration. The slope of the MSD of lithium gradually increases as lithium starts migrate via hopping mechanism within the continuous –Li-O- trunk, which will be illustrated below by tracing the movement of one single lithium ion. After about 100 ps, the distance traveled by lithium is greater than any other species, and, what is most important, the slope of log(MSD) vs. log(t) is close to 1 after around 120 ps, indicating the start of the diffusive regime. The –Li-O- trunk possesses little mobility just as the –Li-O- clusters in siloxy-based system. However lithium manages to diffuse by de-coupling from the oxygen it bonds to, namely breaking ionic bonds with adjacent

oxygen atoms and form new bonds with new oxygen atoms. This site-hopping mechanism adopted by diffusive species is very common among ionic materials.

To prove that Li^+ actually hopped between sites other than experiencing high magnitude vibration, the movement of a single Li^+ ion in carboxyl-based electrolyte at 550 K is traced, as shown in figure 4-9. The cation initially vibrates around the local energy minimum when it sits in a site surrounded by three opposite-charged oxygen anions, O#77, O#22 and O#3. These three anions and the lithium cation are essentlially in the same plane, while O#66 is far away outside of this plane. As time goes by, the lithium cation gradually shifts toward O#66 while the carboxyl groups largely remain at their position, except for slight wiggling and rotation. Eventually the lithium cation resides between O#77 and O#66, possibly another local energy minimum. These snapshots correspond to the time circled in figure 4-9 h), where coordinates of the lithium exhibit great shifts. The observation of the movement of one single lithium cation is consistent with our earlier assumption: the -Li-O- domain has little mobility with diffusion of lithium ions mainly relying on lithium ions hopping between local energy minima on potential surface. Hence we can claim with confidence that lithium ions diffuse within the –Li-O- band in carboxyl-based systems. The diffusion coefficient can be calculated from the MSD according to:

$$D = \frac{1}{6}\lim_{t\to\infty}\frac{C_{rr}(t)}{t}, \qquad 4\text{-}2$$

in which $C_{rr}(t)$ is the MSD at time t. Hence, at 550 K, the diffusion coefficient of Li^+ cations in carboxyl-based systems is calculated by assessing the slope of MSD curve after 100 ps on a linear scale. It equals to $2.78\cdot10^{-6}$ cm^2/s. The diffusion coefficient of

of Li^+ cations in the siloxy-based C5-POSS cannot be calculated since the lithium never diffuses. Furthermore, the diffusion coefficient could be utilized to obtain ion conductivity. The Nernst-Einstein function describes the relationship between ion conductivity and diffusion coefficient:

$$\lambda = \frac{cDZ^2F^2}{RT} \qquad 4\text{-}3$$

where c is the mol concentration of conducting ions; Z = 1, is the valance of the Li^+ ion; F is Faraday constant with a value of 96500 Cb/mol; and R is the gas constant. Hence from this function, when Li^+ has a concentration of $2.298 \cdot 10^{-3}$ mol/cm^3, the conductivity of Li+ in carboxyl-based electrolyte at 550 K is about 1.3 siemens per meter per mol.

As we have described before, the diffusion of Li^+ is a process in which Li+ cations overcome the energy barrier between local energy minima. Therefore, the diffusivity of the lithium cations follows the Arrhenius equation:

$$D = D_0 \cdot e^{-\frac{E_A}{R \cdot T}}, \qquad 4\text{-}4$$

where R is gas constant and E_A is activation energy. D_0 is the maximum diffusion coefficient, namely the diffusion coefficient of a material at infinite temperature. T is temperature and D is the diffusion coefficient at temperature T. We already know the diffusion coefficient of lithium in carboxyl-based C5-POSS is $2.78 \cdot 10^{-6}$ cm^2/s at 550 K. To obtain the activation energy, the diffusion coefficient must be determined as a function of the temperature. The carboxyl-based C5-POSS was heated to 600 K at a rate of 0.5 K/ps. A smaller time step of 0.25 fs is used due to the increased vibration frequency of hydrogen. The system is relaxed for 1 ns before the MSD is measured

over a 200 ps time period. The resulting MSD is shown in figure 4-10, on a log-log scale. Compared to the displacements at 550 K, all elements possess higher mobility at 600 K. At this high temperature, the displacement of lithium surpasses that of hydrogen as early as 60 ps. The diffusive regime for lithium is better defined at this temperature and the diffusion coefficient is calculated to be $5.85 \cdot 10^{-6}$ cm^2/s by evaluating the slope of the curve after 100 ps. Fitting the data using equation 4-4 yields a reasonable estimate for the activation energy for lithium to diffuse in carboxyl-based electrolyte, with a value of $4.08 \cdot 10^4$ J/mol. We recognize that this is a very small temperature range for determining such a quantity. However, at higher temperatures the system melts, and we would be measuring liquid-state diffusion, and at lower temperatures Li does not reach its diffusive regime within 200 ps.

Theoretically, by increasing the temperature in the siloxy-based electrolyte, Li^+ will exhibit higher mobility and overcome the energy barrier to break out of its POSS-cube surrounded cluster, and travel as far as it does at lower temperature in carboxyl-based system. Practically, however, the hydrocarbon in the system starts to disintegrate and melt before a diffusive regime for Li is reached, making the siloxy-based system less interesting for battery electrolyte applications.

We have also investigated the carboxyl-based and siloxy-based systems that contain 20 carbons in the hydrocarbon chains. The same simulation approach is taken for the two C20-POSS electrolyte systems. The calculations take much longer time as the two C20-POSS systems contain almost twice the number of particles compared to their C5-POSS counterparts. Hence the MSDs are collected for both systems over a shorter time period. At 575 K, all species in siloxy-based C20-POSS exhibit greater mobility than

those in siloxy-based C5-POSS at 550 K. The higher mobility of species partly results from the higher temperature for C20-POSS, but it can also be attributed to the fact that the different species are connected with longer, more flexible hydrocarbon chains, which facilitate the motion of particles. As in the siloxy C5-POSS, in siloxy C20-POSS systems the –Li-O- domains show lowest mobility and behave as anchoring points, as revealed by the MSDs of lithium and non-bridging oxygen. POSS cages, anchored by the –Li-O- clusters, have second lowest mobility while hydrocarbon chains enjoy the greatest degree of freedom now that they are on average ten C-C bonds away from the anchoring POSS/-Li-O- clusters. No species show signs of diffusion as the slope of log(MSD) versus log(t) is well below 1 for all of them.

In carboxyl-based C20-POSS, the impact of the length of the hydrocarbon chain on the mobility of all species in the system is more obvious. The displacements of all species after 10 ps in carboxyl-based C20-POSS at 575 K (fig. 4-11 b) are greater than those in carboxyl-based C5-POSS at 600 K (fig. 4-8 b). The long chains, flexible to straighten or bend, provide greater independence in relative movements for POSS aggregates, hydrocarbon segments and the continuous –Li-O- trunk. Hence the motion of species is mainly subject to the binding force within each segment, but less impeded by other segments. Similar to the carboxyl C5-POSS, carboxyl C20-POSS contains the continuous –Li-O- band providing anchoring sites and exhibiting the lowest mobility. Hydrocarbons anchored to the ionic domains have slightly higher mobility. POSS cages, dangling far away from the –Li-O- band exhibit highest mobility. None of these species show signs of diffusion except for lithium. Even though the –Li-O- band is fixed and does not move around, the lithium ions can migrate via hopping diffusion

within the continuous –Li-O- band. The displacement of lithium reveals a sharp increase in slope at around 60 ps and it catches up with other species around 70 ps. This indicates the start of diffusive regime, and lithium can potentially migrate far distances over longer time periods. The slope of the MSD of carboxyl-based C20-POSS after ~60 ps gives us the diffusion coefficient of lithium in the system to be about $2.31 \cdot 10^{-5}$ cm^2/s, much higher than that in carboxyl-based C5-POSS.

5.4 Summary

This chapter demonstrates the concept of utilizing POSS nano-hybrid as candidate of electrolyte feasible with careful engineering of doping. So far we have discovered that by introducing charged groups attached to the end of the hydrocarbon chain can produce ion conducting system while introducing charged groups directly attached to POSS particles does not. Interestingly, the only species that reaches a diffusive regime is lithium embedded in a continuous trunk of Li-O, which as a whole constitutes the least mobile and most stable part of the structure. Hence, Li migration relies on the existence of defects in the Li-O trunk. The lengthening of the chains appears to promote the diffusivity of the conducting ions in the electrolyte. The interested reader is encouraged to continue the exploration to improve the conductivity of POSS based electrolytes. The possible investigation could start with varying the number of functionalized groups that POSS cages bond to, increasing the concentration of charged groups in the hydrocarbon chains, and replacing the hydrocarbon chains with other organic substitutes, etc.

Li^+	q_i (ecu)= +1; n_i= 2; z_i = 1; σ_i (nm) = 0.0925;	
Pairing	$A_{ij}\left(10^{-19}J\right)$	$\rho_{ij}\left(nm^{-1}\right)$
Li - Si	0.145	34.469
Li - O	1.8	25.0
Li - C	0.195	39.366
Li - H	0.145	22.346
Li - Li	0.19	34.438

Table 5-1 Parameters for lithium in the force field

	Spacing at first peak (Å)	Spacing at g(r) minimum (Å)	Coordination Number
Mono-C5POSS	8.3	11.9	8.8
Carboxyl-C5POSS	8.3	12.3	10.8
Siloxy-C5POSS	8.8	12.5	9.8

Table 5-2 Quantitative measurement of pair correlation function for different POSS systems at 550 K

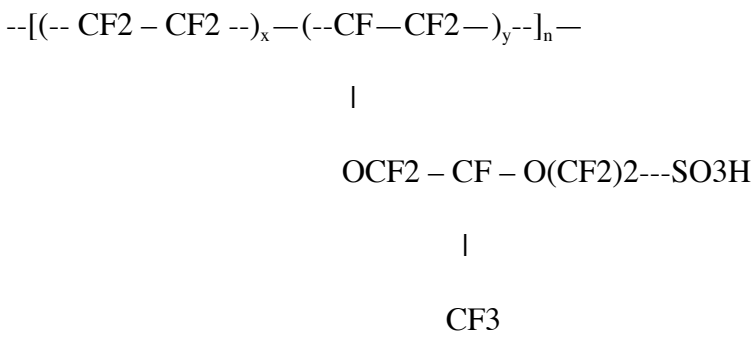

Fig. 5-1 Chemical structure of Nafion

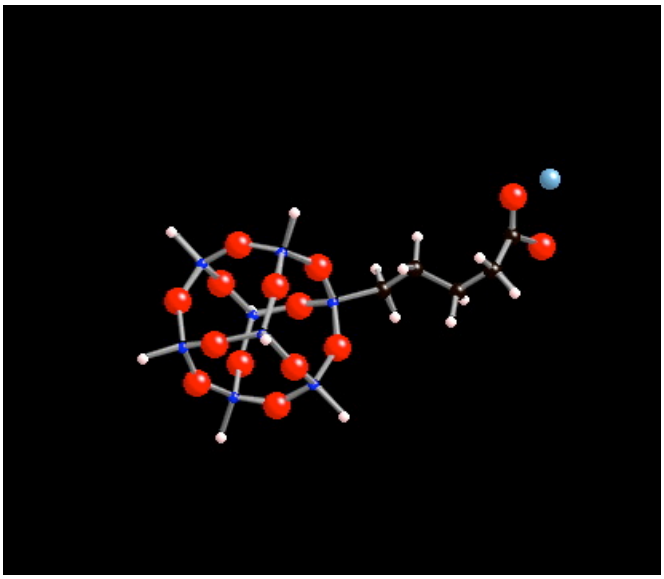

a)

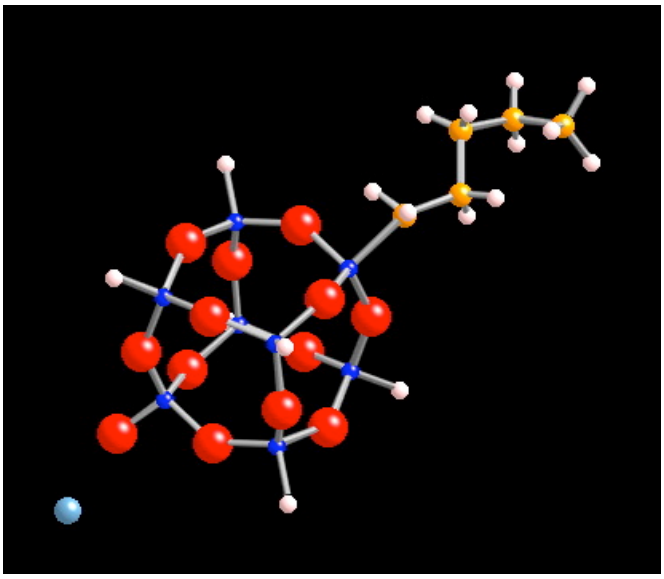

b)

Fig. 5-2 a) Single $H_7Si_8O_{12}$-$C_5H_8OO^-Li^+$ molecule, carboxyl-based Li+ electrolyte and b) Single $Li^+O^-Si_8O_{12}H_6$-C_5H_{11} molecule, siloxy-based Li^+ electrolyte; Blue, Silicon; Red, Oxygen; Orange, Carbon; Pink, Hydrogen; Light Blue, Lithium

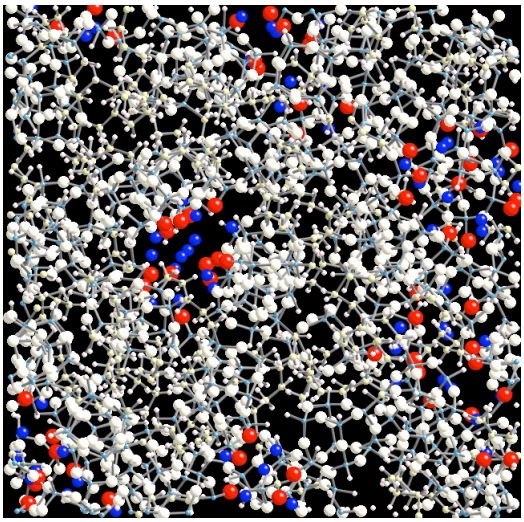

a)

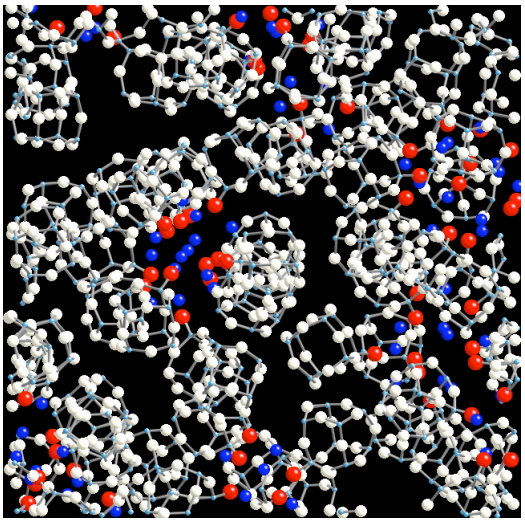

b)

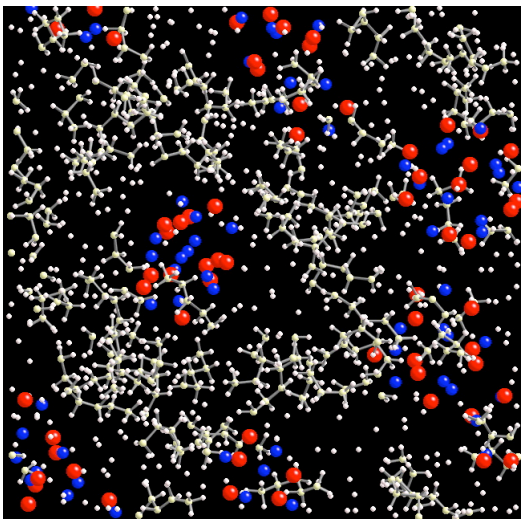

c)

Fig. 5-3 Snapshots of mono-C5POSS siloxy-based Li+ electrolyte at 550 K: a) the structure with all elements shown, b) the structure with hydrocarbon hidden, c) the structure with POSS particles hidden; lithium, blue; oxygen bonding to lithium, red; silicon, light blue; oxygen, light pink; carbon, light yellow; hydrogen, lighter pink;

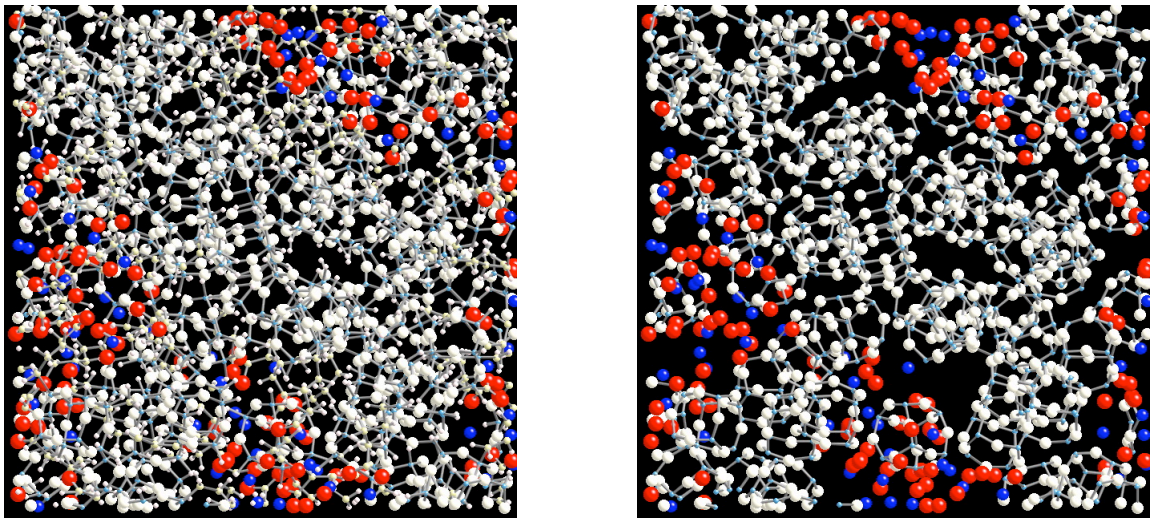

a) b)

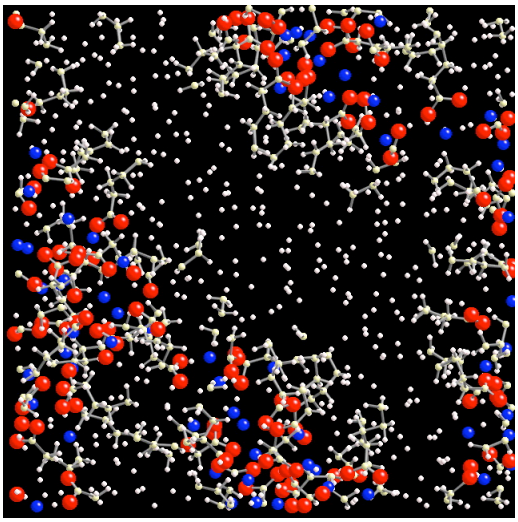

c)

Fig. 5-4 Snapshots of mono-C5POSS Carboxyl-based Li+ electrolyte at 550 K: a) the structure with all elements shown, b) the structure with hydrocarbon hidden, c) the structure with POSS particles hidden; lithium, blue; oxygen bonding to lithium, red; silicon, light blue; oxygen, light pink; carbon, light yellow; hydrogen, lighter pink;

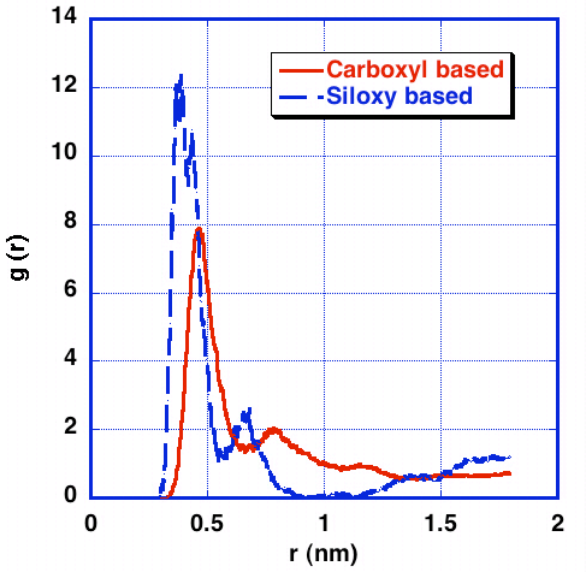

a)

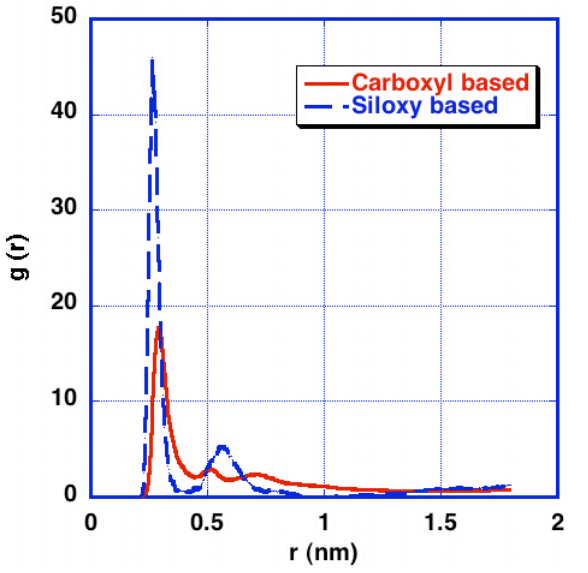

b)

Fig. 5-5 Pair correlation functions of elements, a) Li-Li and b) Li-O

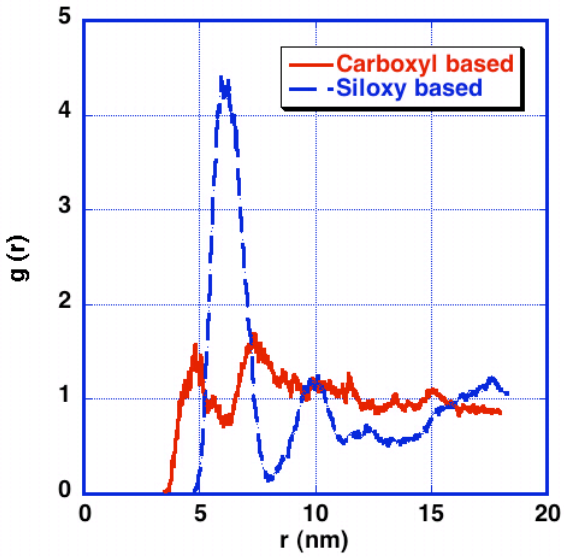

a)

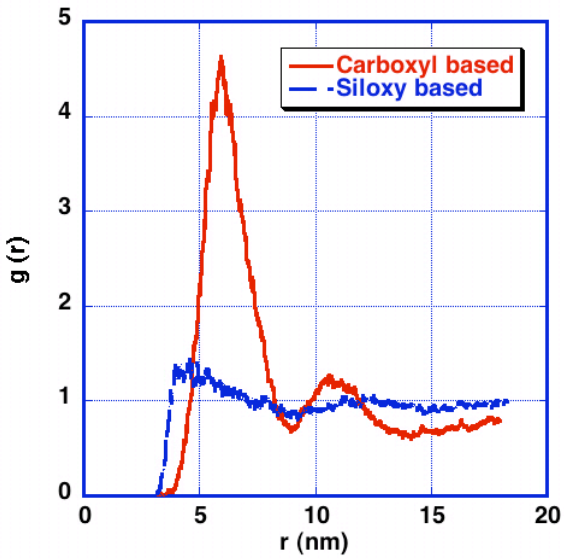

b)

Fig. 5-6 a) 'head' – 'head' and b) 'tail' – 'tail' distribution in carboxyl-based and siloxy-based mono-C5POSS

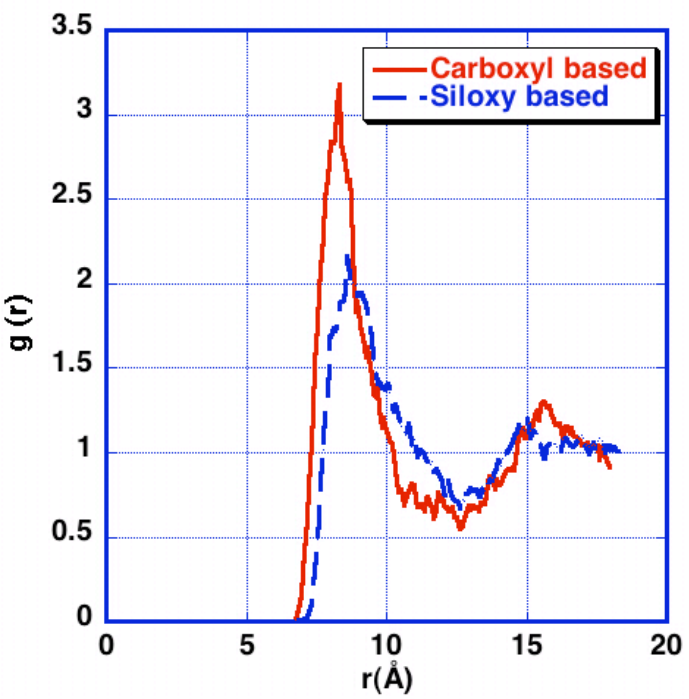

Fig. 5-7 Centers of POSS particles pair correlation function

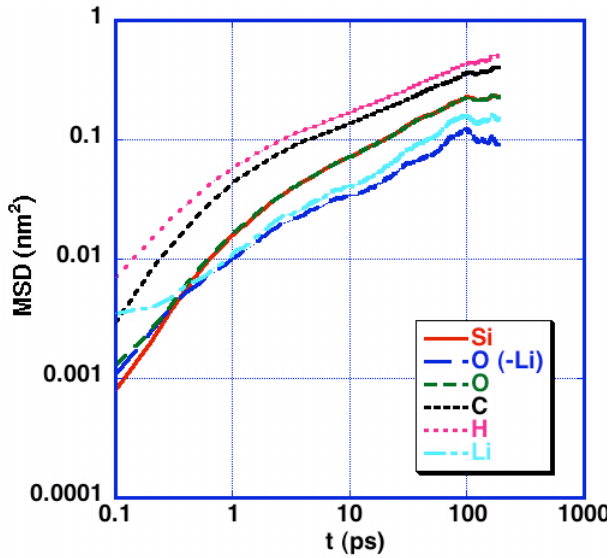

a)

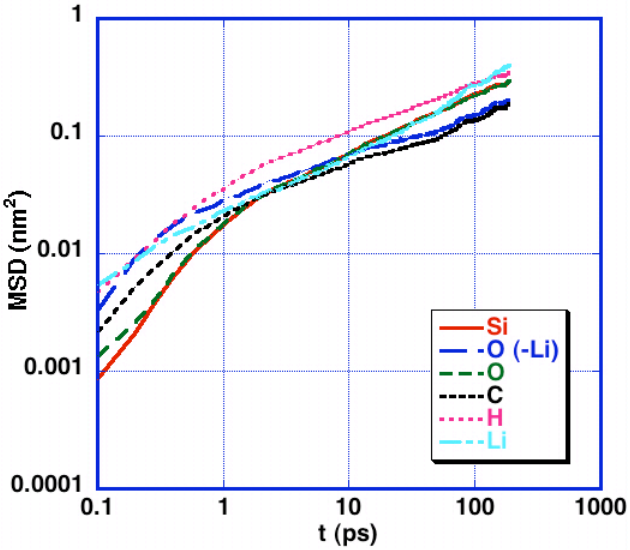

b)

Fig. 5-8 Mean Squared displacement of elements at 550 K: a) siloxy-based C5-POSS electrolyte; and b) carboxyl-based C5-POSS electrolyte

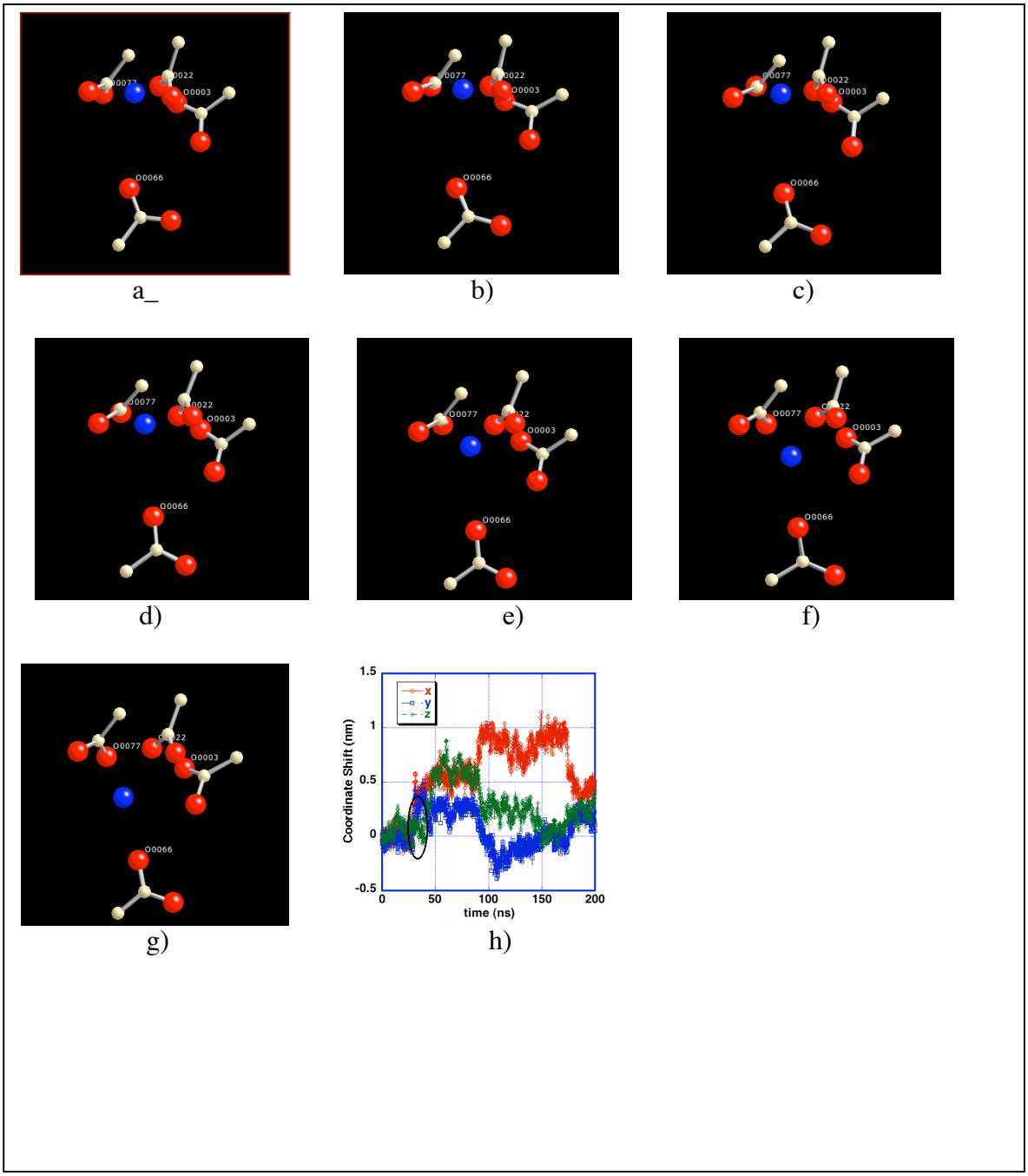

Fig. 5-9 Snapshots of local structures of carboxyl-based system at 550 K starting from a random time t, with most particles in the system hidden for clarity purpose, blue, lithium, red, oxygen and light yellow, carbon: structure at a) t; b) t + 0.025 ps; c) t + 0.05 ps; d) t + 0.075 ps; e) t + 0.1 ps; f) t + 0.125 ps; g) t + 0.15 ps; h) coordinates lf the Li^+ cation as a function of time

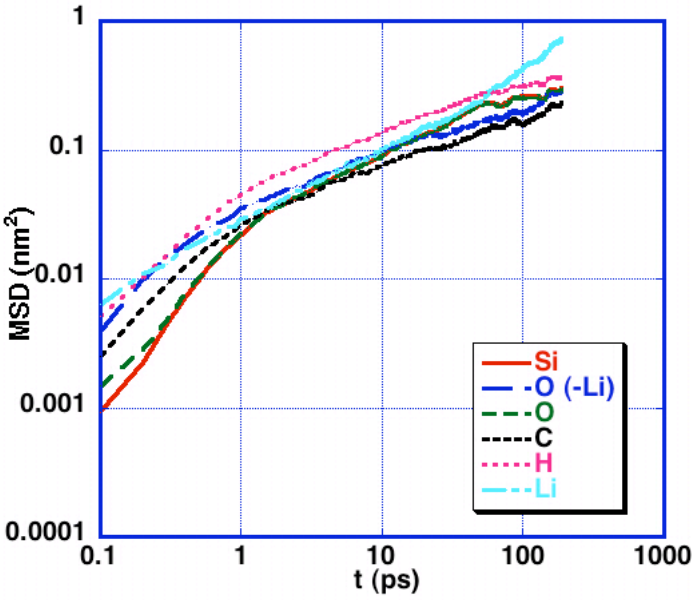

Fig. 5-10 Mean Squared displacement of elements at 600 K in carboxyl-based C5-POSS electrolyte

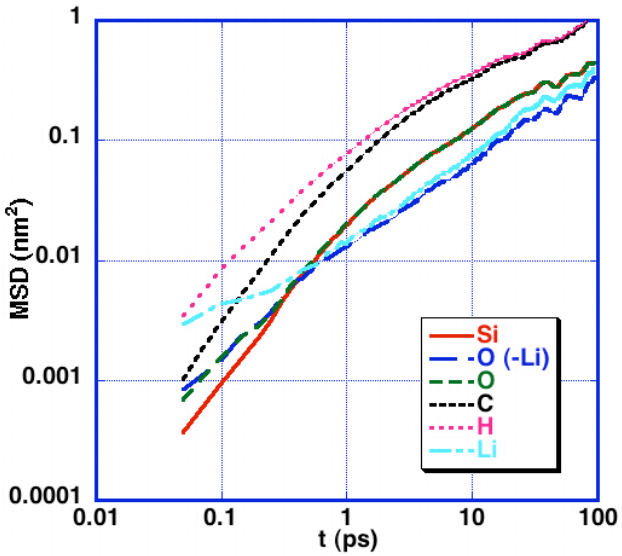

a)

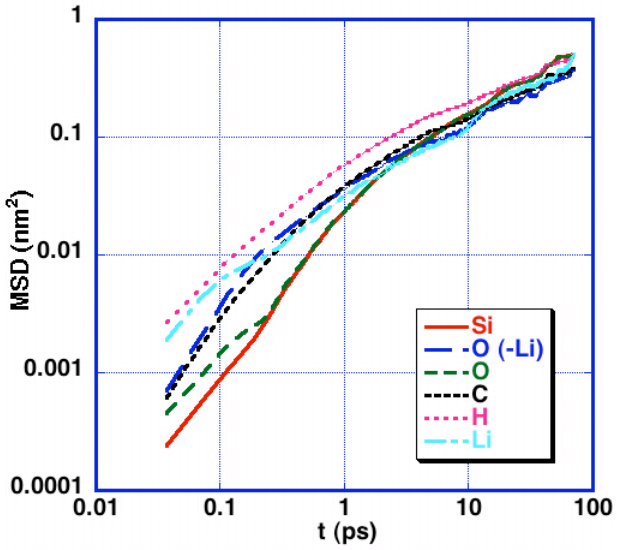

b)

Fig. 5-11 Mean Squared displacement of elements at 575 K, a) in siloxy-based C20-POSS electrolyte; b) in carboxyl-based C20-POSS electrolyte

References

1. Hickner, M.A., et al., Alternative Polymer Systems for Proton Exchange Membranes. Chem. Rev., 2004. 104: p. 4587-4612.
2. Lassegues, J.C., Proton Conductors: Solids, Membranes and Gels-Materials and Devices. 1992, Cambridge, U.K.: Cambridge University Press.
3. Nogami, M., et al., High Proton Conductivity in Porous P2O5-SiO2 Glasses. J. Phys. Chem. B., 1999. 103: p. 9468-9472.
4. Nogami, M., Y. Goto, and T. Kasuga, Proton Conductivity in Zr4+ - Ion-Doped P2O5-SiO2 Porous Glasses. J. Am. Ceram. Soc., 2003. 86(9): p. 1504-1507.
5. Li, Z., et al., A Room-Temperature Ionic-Liquid-Templated Proton-Conducting Gelatinous Electrolyte. J. Phys. Chem. B., 2004. 108: p. 17512-17518.
6. Becker, W. and G. Schmidt-Naake, Proton Exchange Membranes by Irradiation Induced Grafting of Styrene Onto FEP and ETFE: Influences of the Crosslinker N, N-Methylene-bis-acrylamide. Chemical Engineering & Technology, 2002. 25(4): p. 373-377.
7. Reardon, B.J., Ph. D. Thesis, University of Illinois. 1997.

Chapter 6

Summary and Possible Extension of the Work

The goal for the work presented in this thesis was to provide a comprehensive analysis of structural and dynamic properties of alkane functionalized POSS nano-hybrids. We have carried out molecular dynamics simulation using an in-house force field.

Based on an existing in-house force field, which was designed to model covalent-ionic bonding in silica, Lennard-Jones and four-body torsion potential were added to address the complex interactions between hydrocarbons in POSS-alkane structures. Taking mono-functionalized hexyl-POSS as model material, parameters of the force field were optimized to reproduce the experimental results: crystal structure and infrared spectrum of mono-hexyl-POSS. The simulation included 64 mono-hexyl-POSS molecules and ran NPT ensemble at 291 K and ambient pressure. To apply constant pressure, Rahman-Parrinello algorithm is employed to allow the size and the shape of the simulation box to change.

After I obtained the parameters that yield satisfactory results, I investigate the same mono-hexyl-POSS system under conditions where no experiment data are available, i.e. melting and subsequent glass transition process. A different algorithm, Andersen

algorithm is used to apply constant pressure to liquid cannot withstand the sheer stress in Rahman-Parrinello algorithm. The equilibrium crystal structure at 291 K is heated up to 550 K at a rate of 1 K/ps and is then cooled below 200 K. Configuration is collected every 20 K and is relaxed in the force field for another 1 ns before structural and dynamic properties are measured. A melting point of 430 K is predicted by the force field. The melting process takes two steps: hydrocarbon deviates from the lattice sites and mix with neighboring hydrocarbons first and then 'drag' the POSS particles off the lattice sites as well to form amorphous structure. The preferred orientational order, reflected by strong first peaks in 'head'-'head' and 'tail'-'tail' distribution, diminishes upon melting, and partially regains order after glass transition. The 'head' is defined as the silicon atom located opposite to the hexyl chain and the 'tail' is defined as the carbon atom at the end of the hydrocarbon chain.

A further study on the effect of the length of tethers on the structural properties of resulting nano-composites find out that the distance between the closest neighboring POSS cages is not affected by the length of the tether. The length of the alkane chain does, however, have an impact on overall packing. The longer the chain the more efficient packing pattern is obtained as longer chains are flexible to bend to fill the interstices around POSS cubes. Hence the nano-coomposites with longer chains are less porous. It is of no surprise then when containing the same amount of hydrocarbon components, the mono-functionalized system, which has longer chain, is more compact than the di-functionalized. The packing of pendent structure is constrained by the bonding of the POSS cages to the common backbone. This is most obvious when the chain is short.

The inherent nature of the POSS nano-composites, a structure composed of hard and stable segments of POSS domain and soft and mobile hydrocarbon domain, makes them an ideal candidate in application of battery electrolyte. Two systems are constructed to introduce the conducting ions, one containing a siloxy group at the corner of POSS cubes and the other containing a carboxyl group at the end of the hydrocarbon chain. Both of the systems form –Li-O- domains that behave as anchoring points for the structure and reduce the mobility of all elements in the system. The –Li-O- domain formed in carboxyl-based alkane-POSS system is continuous, thanks to the flexible chain which accommodates the attraction between lithium and oxygen of neighboring molecules. Even though the –Li-O- band or trunk itself cannot migrate, lithium ions themselves manage to diffuse within the trunk through hopping mechanism. Thus we have proved that POSS nano-compostes could be made into electrolyte. It is also found that mono-C20-POSS carboxyl-based system is better in terms of conducting compared to the mono-C5-POSS carboxyl-based system. The increased organic component, however, could potentially bring disadvantage of inferior mechanical properties.

As possible extension of future research, investigation of complex network structure formed by multi-functionalized POSS would be very useful. Due to the intensive resource needed to calculate complex and bigger system, MD simulation of such system should focus on producing variables such as spacing distance between nearest POSS particles as input for meso-scale simulation.

Additional effort is needed to continue exploration of producing practical ion conductor based POSS nano-composites. The architect of POSS configuration, the

location to insert the charged group and possibility of non-alkane organic groups need to be investigated to identify structures of better conducting quality.

Appendix A. Charge Optimization Procedure

We optimize the inter-molecular interaction in MD force fields by matching the potential energy surface produced from ab initio calculation. A model is set up with a separate system composed of a fixed single Polyhedral Oligomeric Silsesquioxane (POSS) with a pair of NaCl as a virtual dipole moving on the spherical surface. Interaction energy between POSS and NaCl as a function of the location of NaCl is obtained by ab initio calculation. In MD force fields that have electrostatic interaction as the only inter-molecular interaction, partial point charges sitting at the center of the atoms are varied to minimize the mean squared difference of the energy surface between MD and ab initio results. Introducing variable charges that are dependent on the environment gives a better approximation to the desired potential energy surface.

1 Introduction

The unique structure and reactivity of octasilsesquioxane, also termed as polyhedral oligomeric silsesquioxane (POSS), leads to a wide range of applications. Substitution at the corners of the POSS cube with organic groups makes it an ideal candidate as the building block for nano-hybrid materials and serves to effectively modify the thermal stability and mechanical properties of the organic matrix[1-5]. POSS also attracts tremendous interest in the design of optical[6, 7] and electronic[8-11] devices. The octa-functionality of the POSS is utilized to synthesize dendrimers[12-14] which play an important role in drug delivery research. The microporous structure[15] synthesized from POSS renders good selectivity in gas adsorption[16] and provides support for various kinds of catalyst[17-21].

Many computational efforts have been made to understand the configuration and structure of the POSS system. According to ab initio calculation, the rigid POSS cages possess relatively high stability compared to silicon oxide cages with different sizes[22]. Xiang et. al. have carried out detailed density function theory calculations on the isolated POSS molecule[23]. They confirmed the stability of octasilsesquioxane and determined the configuration, binding energy and density of states. So far, these researches based on first principle calculations have thoroughly explored the relationship between topology, structure and energy of single POSS molecule without much work on inter-POSS interactions or further POSS-polymer interactions. At a higher scale simulation, Cerius2 software package is employed to obtain the pore size inside the POSS composite materials in a combined experiment and computation work[15]. Bharadwaj et al. used atomistic molecular dynamics simulations with the commercial Compass force field to investigate the effect of POSS on the structural and thermal properties of norbornene-POSS polymers[24]. Their research suggests the reinforcement comes from the ponderous POSS acting as anchoring points. Recently, Striolo et. al. published some work on the transport behavior of POSS in organic solvents[25]. Meso-scale simulation was done to identify the phase transition of tetra-tether POSS systems in various solvents[26]. Most of the MD or meso-scale simulations either utilized commercial packages that are not specifically designed for POSS or had only qualitative agreement with experiment/quantum-mechanics-calculation.

This work contributes to the pool of computation works by investigating the inter-molecular interaction of POSS cages. The potential field around a single POSS molecule is obtained through plane wave computation. Then the charge distribution that

fits the potential profile best is determined. Understanding the local electrostatic forces is essential to the explanation of the mechanism of reinforcement. Especially in the field of catalysis application, local electron distribution directly affects the acidity of the catalyst, and hence determines the ability of accelerating reaction[27]. The accurate charge distribution is obtained in an attempt to bridge between first principle calculation and simulations at higher length scale.

2 Model Development

A single POSS cage, together with a virtual dipole that is composed of Na+ and Cl-, forms an isolated system (Fig. 1). With the center fixed at the origin of the Cartesian axis, the POSS cage has constant bond lengths and bond angles that are determined through the equilibrium state using VASP package: dSi-O= 1.6309 Å, dSi-H= 1.4639 Å,∠SiOSi= 147.5891°, ∠OSiO= 109.711°. The POSS cage is perfectly symmetric and motionless. The virtual dipole is positioned in a sphere around the cage with the dipole vector always parallel to the radial direction. The positive charge Na+ is pointing inward and maintains a fixed distance of 7Å to the origin. This relatively large distance is chosen so that the dipole is far away from the POSS enough to avoid consideration of the difference in short-range repulsion when calculating the total energy.

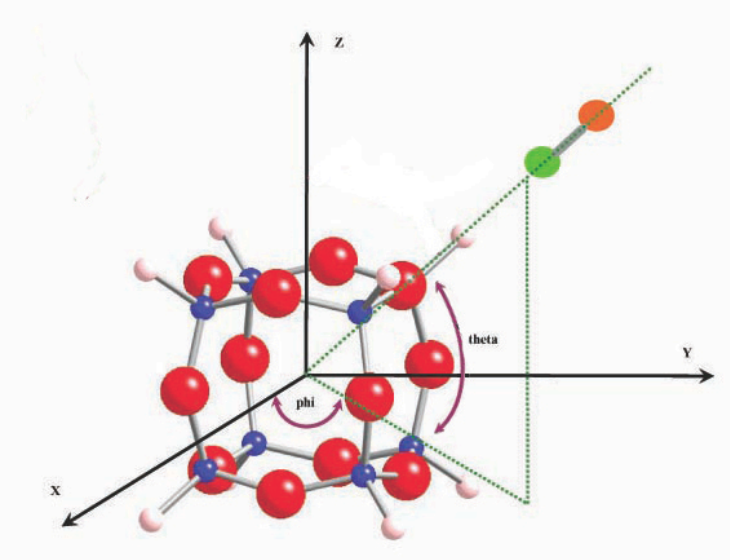

Fig. 1 POSS cage with a virtual dipole: blue, silicon; red, oxygen; pink, hydrogen; green, sodium; orange, clorium

Then this virtual dipole is moved around inside the spherical surface to positions described by Theta and Phi. The total energies of the system Etot, of the separate POSS molecule alone EPOSS and of the separate virtual dipole ENaCl are obtained through density functional theory calculation. By subtracting EPOSS and ENaCl from Etot, the interaction potential energy surface as a function of Theta and Phi, or the vector ri, is obtained:

$$\phi(\mathbf{r_i}) = E_{tot}(\mathbf{r_i}) - E_{POSS} - E_{NaCl} \qquad \text{(A-1)}$$

Take the potential energy surface from ab initio calculations as reference, ϕ(ri). Atomic charges are optimized to produce the electrostatic force field around the POSS cage, ϕq(ri), that best fits the reference surface:

$$\sigma^2 = \frac{1}{N}\sum_{i}^{N}\left[\phi(\mathbf{r_i}) - \phi_q(\mathbf{r_i})\right]^2 \qquad \text{(A-2)}$$

in which mean squared difference $\sigma 2$ needs to be minimized. The charges that satisfy equation (2), also called potential–derived charges, have proven to render higher accuracy in describing the electrostatic interactions than chemical–derived charges based on partitioning of electron clouds [28].

The intuitive charge optimization implements assigning partial atomic charges to the center of each atom, with the same amount to each element. This method has been widely applied because of its simplicity. However, it bears the defect that it ignores the polarization effect of the ions, which imposes inaccuracy on certain materials containing strong polarizable ions such as O2-. To account for the polarization effect which is strong in POSS molecule, three different approaches are available[29]. The straightforward representation is introducing inducible point dipoles which could capture the polarizability quite well, yet creat complex dipole-dipole force evaluation terms into the Hamiltonian. Secondly, the shell model which was originally published by Dick and Overhauser holds true for crystals, especially halide crystals[30]. Problems arise with the shell model in oxides at the surface where the periodicity of the lattice is broken[31]. The artificial spring that connects the core and shell of the ions appears to be vulnerable and unstable, subject to the surrounding electrostatic force field. The third alternative is charge transfer, which allows variable charges dependent on the electrostatic environment through self-consistent atomic electronegativity equalization method (EEM). The major drawback of the charge transfer scheme lies in its inability of representing polariazability in a planar molecule.

Fortunately for the cubic shaped POSS molecule, the defect of the charge transfer method is easily bypassed. This article involves charge distribution by partial point charges and EEM charges.

3 Results and Discussion

The total energy of the separate POSS molecule and of the separate virtual dipole NaCl is found to be –180.630598ev and -4.674982ev respectively through density functional theory calculation. The interaction energy defined in equation (1), as a function of theta and phi, is shown in Fig. 2. The 3D plot exhibits a basin shape landscape with minimum in the middle and maximum at the four corners. To get a clearer view, the trajectory intersection of the potential surface surface at Phi = 45° and at Theta = 30°/45° are presented respectively too. As can be seen from the figures, the lowest energy –0.085946ev appears at around (45°, 35°), which corresponds to the configuration with the dipole sitting closest to the hydrogen at the corner of the POSS cage. While the dipole is pointing to the face center of the POSS cage, the interaction energy reaches the maximum –0.024873ev. And when the dipole moves to a position where it is closest to the oxygen ion, at (45°, 0°) or (0°/90°, 45°), the interaction energy obtained is –0.058906ev.

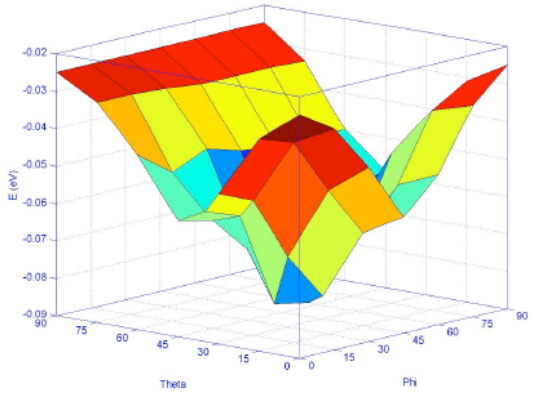

a)

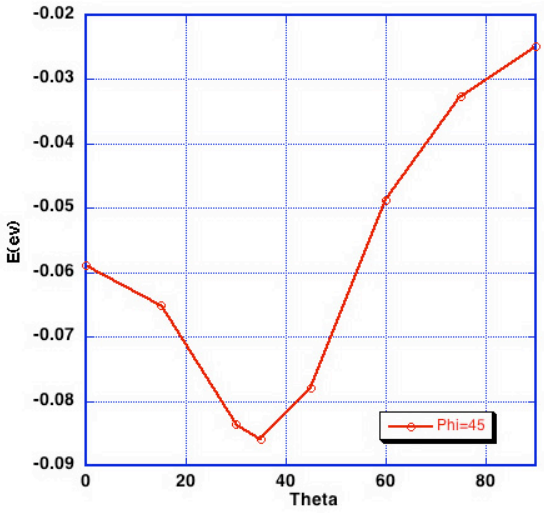

b)

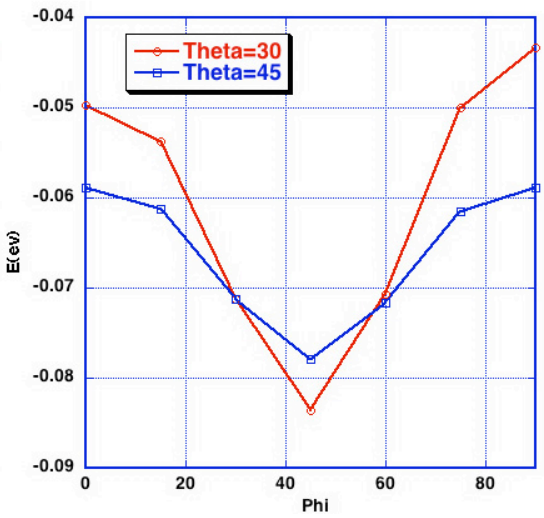

c)

Fig. 2 (a) Potential energy surface from density functional theory calculation, color code: from higher to lower energy, red -> yellow ->blue; b) Intersection of the potential surface with Phi = 45°; c) Intersection of the potential surface with Theta = 35°/45°

The potential energy surface indicates an overall attraction between the POSS cage and the virtual dipole from the all-negative values. The dipole pulls electrons toward itself to create polarized displacement from the original symmetric electron cloud distribution of the POSS molecule. The strongest attraction, depicted by the lowest energy, exists when the dipole is closest to the corner. The weakest attraction,

accordingly, appears when the dipole points to the center of the POSS surface, where the electron density is relatively low.

Then the atomic charges are optimized by minimizing the mean squared difference defined in equation (2). To prevent the ions from having net charges against common sense physics, a constraint is imposed so that only charges between 0 and valence charge of the element are made possible to the ions. Also each molecule is kept neutral during the charge optimization process:

$$q_{Si} + 1.5q_O + q_H = 0.0 \qquad q_{Na} + q_{Cl} = 0.0 \tag{A-3}$$

The resulting charges are shown in Table-1. The best match is obtained when the charges are 3.408, -2.0 and –0.408 on Silicon, oxygen and hydrogen respectively. To better understand the extent by how much the electrostatic force field is off the reference, a quantity is defined as relative error (RE%):

$$RE\% = N\sigma^2 / \sum_{\mathbf{i}}^{\mathbf{N}} \phi^2(\mathbf{r_i}) \tag{A-4}$$

As can seen from the table, the relative error from the set of the optimized charges is higher than 50%, relatively large. This makes variable charges necessary to provide a more accurate description of the interaction energy which is sensitively dependent on the environment.

Table 1 Fitting the potential energy surface with partial atomic charges

q_{Si}	q_O	q_H	q_{Na}	q_{Cl}	$\sigma^2(ev^2)$	RE%
3.408	-2.0	-0.408	0.662	-0.662	2.192e-3	52.5716%

EEM mothod[32] or the very similar charge equilibration (Qeq) approach[33] adapts a theorem of equal electronegativity in a steady system and hence assigns charges to the atoms real time according to the electrostatic environment. The following equation is used:

$$\chi = \chi_i^* + 2\eta_i^* q_i + \sum_{i \neq j}^{n} q_j J_{ij} \qquad \text{(A-5)}$$

in which χ stands for the electronegativity of the molecule, χ_i^* refers to the electonegativity of atom i and η_i^* represents the hardness of atom i. J_{ij} describes the electrostatic interaction between atoms. It takes the form of $\frac{14.4}{R_{ij}}$ between charges belonging to different molecules. As for charges in the same molecule, a simplified version[34][35] is taken to replace the complex integration of overlapped orbitals:

$$J_{ij} = \frac{14.4}{\left(R_{ij}^3 + \left(\frac{1}{J_{ij}^0} \right)^3 \right)^{\frac{1}{3}}} \quad , \; J_{ij}^0 = \left(J_{ii}^0 J_{jj}^0 \right)^{\frac{1}{2}} \qquad \text{(A-6)}$$

The parameters in equation (5) and (6) are taken from reference 35 with slight changes to yield higher resemblance to the potential energy surface from ab initio calculation. These parameters are listed in Table-2. However, EEM scheme is not applied to NaCl for simplification. Instead the charges on the virtual dipole are picked through grid searching method for values that generate best match, +0.69 and –0.69 respectively.

Table-2: parameters used in calculation

Atom type	χ_i^*	η_i^*	J_{ii}^0
Si	1.50	5.2213	0.2888
O	9.40	9.8850	0.8000
H	3.14	8.7226	0.4783

The potential energy surface obtained (Fig. 3) using the above listed parameters generates much higher resemblance than the fixed partial point charges. Again, intersection of the potential energy surface is plotted to get a clearer view. The mean squared difference is approximately 8.639e-5 ev with relative error only around 3.81%, a huge improvement comparing to 52.5716% of the fixed point charge approach.

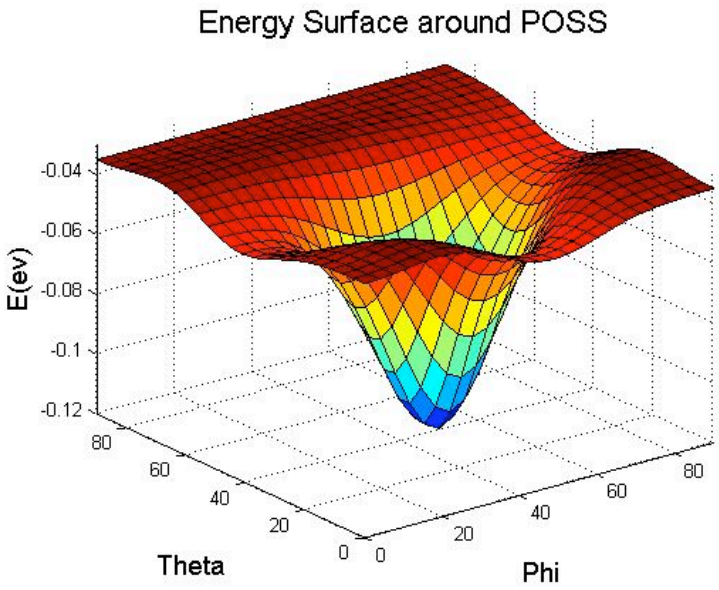

a)

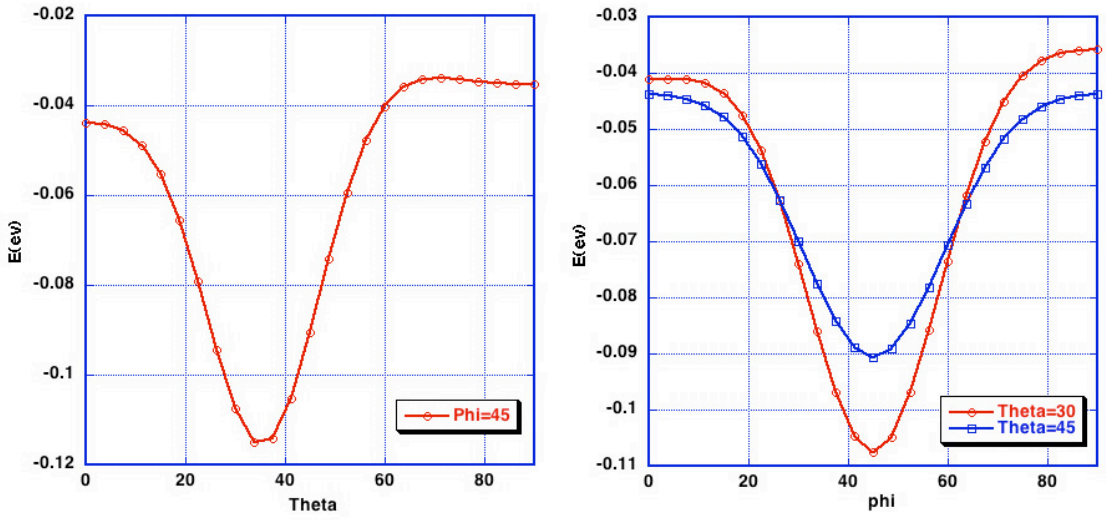

b) c)

Figure 3. a) Potential surface generated by EEM charges; b) Intersection of the potential surface with Phi = 45°; c) Intersection of the potential surface with Theta = 35° and 45° respectively

Even though the 3D plot captures the landscape of the reference potential energy surface qualitatively, a closer look at the intersected trajectories exposes the quantitative differences. It gives a lower value where the energy surface hits the minimum, overestimating the attraction. On the other hand, when the dipole is close to the oxygen, the attraction is under-estimated, indicating the polarizability of the oxygen is not full represented. What is also underestimated is the energy maximum at face center of the POSS cage. Overall, the interaction energy surface generated from the EEM charges produces a broader band between energy maximum and minimum and a higher gradient.Yet the match is considered a great success with the relative error 3.81%, considering the exact match of potential surface has been reported to be very difficult.

The charges obtained through this EEM scheme varies with the configurations. Yet, the magnitude of the fluctuations maintains relatively small. For the separate POSS system, EEM charges and Mulliken charges from VASP package are listed in table 3. As for the combined POSS-dipole system, the charge dependence on the configuration is shown in Fig. 4.

Table-3 Charge Comparison

	Si#1	Si#8	O#9	O#20	H#21	H#28
EEM	0.79076	0.79076	-0.52930	-0.52930	0.0031899	0.0031899
Mulliken	1.5230	1.5234	-0.8157	-0.8158	-0.2999	-0.2996

Charges are selectively labeled. With Phi fixed at 45°, as Theta varies from 0° to 90°, charges on both silicon and hydrogen which are close to the virtual decrease and increase again, indicating a stronger pull over the electrons by the dipole at the short distance (Theta = 35°). While the other pair of silicon and hydrogen which are further away from the dipole present no significant difference. The similar trend occurs for Phi dependence when Theta is fixed at 45°. The charges on oxygen #9 decrease continuously as Phi increase from 0° to 90° at a constant 45° Theta, in an agreement with the claim of stronger pull from the dipole within shorter distance.

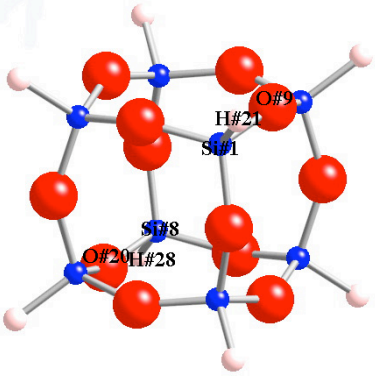
O#9
H#21
Si#1
Si#8
O#20
H#28

a)

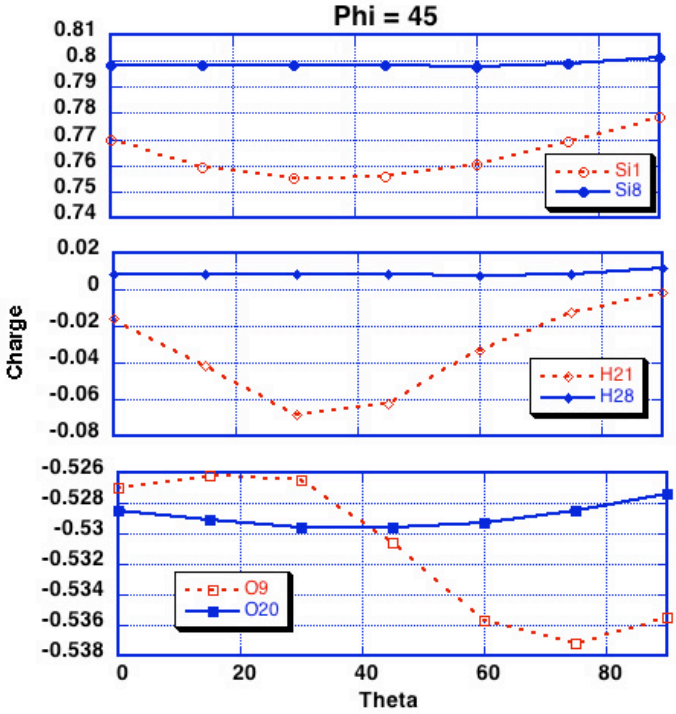
Phi = 45
0.81
0.8
0.79
0.78
0.77
0.76
0.75
0.74
Si1
Si8
0.02
0
-0.02
-0.04
-0.06
-0.08
H21
H28
-0.526
-0.528
-0.53
-0.532
-0.534
-0.536
-0.538
O9
O20
Charge
0
20
40
60
80
Theta

b)

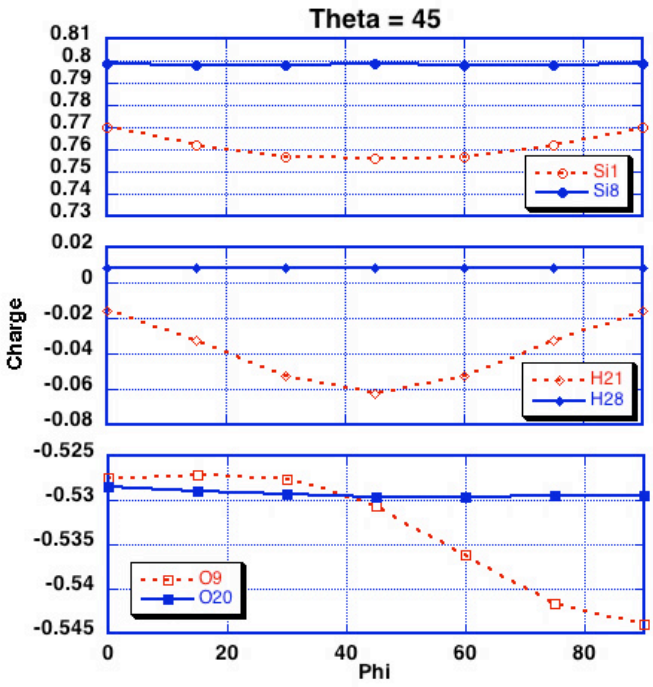

c)

Fig. 4 Charge dependence over configuration. a) atom label; b) and c) charge vs. configuration

Overall the charge fluctuation is quite small, with a magnitude of less than 0.4. Relatively the difference is only 4% for silicon and oxygen, while almost 200% for hydrogen due to its small value. Because of the difference of the charges in different electrostatic environment is very small, it is optimistic to assume that the change of the charges will pose little effect to short-range interactions once plugged into MD force field, even though more calculations need to be done to confirm the assumption.

4 Conclusion

This paper has carried out both ab initio calculation and electrostatic force field evaluation to describe the interaction energy surface around a single POSS molecule. It is found that the POSS exhibits strongest attraction to the virtual dipole implemented when the dipole locates closest to the corner of the POSS cage. The attraction is weakest when the dipole is pointing to the face center of the POSS cage. The visualization of the potential energy surface help to understand the force field around the POSS cage and offers explanation of the POSS crystal.

Two schemes are employed to produce charges that would generate a force field to match the quantum mechanical reference best. The partial atomic charge approach optimizes a set of fixed charges for each element in the POSS cage. The resulting potential surface proves to be not a satisfying match given the large relative error 52.5716%. The Electronegativity Equalization Method (EEM) approach applies a theorem to determine the charges based on the electrostatic environment. This EEM approach appears to provide much better resemblance with a relative error only 3.81%. The charge dependence on the configuration is also briefly discussed.

References

1. Lichtenhan, J.D., Polyhedral Oligomeric Silsesquioxanes - Building-Blocks for Silsesquioxane-Based Polymers and Hybrid Materials. Comments on Inorganic Chemistry, 1995. 17(2): p. 115-130.
2. Schwab, J.J. and J.D. Lichtenhan, Polyhedral oligomeric silsesquioxane (POSS)-based polymers. Applied Organometallic Chemistry, 1998. 12(10-11): p. 707-713.
3. Marcolli, C. and G. Calzaferri, Monosubstituted octasilasesquioxanes. Applied Organometallic Chemistry, 1999. 13(4): p. 213-226.
4. Li, G.Z., et al., Polyhedral oligomeric silsesquioxane (POSS) polymers and copolymers: A review. Journal of Inorganic and Organometallic Polymers, 2001. 11(3): p. 123-154.
5. Lichtenhan, J.D., J.J. Schwab, and W.A. Reinerth, Nanostructured chemicals: A new era in chemical technology. Chemical Innovation, 2001. 31(1): p. 3-5.
6. Matsuda, A., et al., Thermal softening behavior and application to transparent thick films of poly(benzylsilsesquioxane) particles prepared by the sol-gel process. Journal of the American Ceramic Society, 2001. 84(4): p. 775-780.
7. Shen, J., et al., Modeling of configurations and third-order nonlinear optical properties of methyl silsesquioxanes. Journal of Chemical Physics, 2005. 122(20).
8. Leu, C.M., Y.T. Chang, and K.H. Wei, Polyimide-side-chain tethered polyhedral oligomeric silsesquioxane nanocomposites for low-dielectric film applications. Chemistry of Materials, 2003. 15(19): p. 3721-3727.
9. Leu, C.M., Y.T. Chang, and K.H. Wei, Synthesis and dielectric properties of polyimide-tethered polyhedral oligomeric silsesquioxane (POSS) nanocomposites via POSS-diamine. Macromolecules, 2003. 36(24): p. 9122-9127.
10. Chen, Y.W. and E.T. Kang, New approach to nanocomposites of polyimides containing polyhedral oligomeric silsesquioxane for dielectric applications. Materials Letters, 2004. 58(29): p. 3716-3719.
11. Cheng, Y.Y., J.Y. Kan, and I.S. Lin, Adhesion studies of low-k silsesquioxane. Thin Solid Films, 2004. 462-63: p. 297-301.
12. Casado, C.M., et al., Cyclic siloxanes and silsesquioxanes as cores and frameworks for the construction of ferrocenyl dendrimers and polymers. Applied Organometallic Chemistry, 1999. 13(4): p. 245-259.
13. Zhang, X.J., et al., Synthesis and computer modelling of hydroxy-derivatised carbosilane dendrimers based on polyhedral silsesquioxane cores. Journal of the Chemical Society-Dalton Transactions, 2001(22): p. 3261-3268.
14. Ropartz, L., et al., Hydrocarbonylation reactions using alkylphosphine-containing dendrimers based on a polyhedral oligosilsesquioxane core. Journal of the Chemical Society-Dalton Transactions, 2002(9): p. 1997-2008.
15. Zhang, C.X., et al., Highly porous polyhedral silsesquioxane polymers. Synthesis and characterization. Journal of the American Chemical Society, 1998. 120(33): p. 8380-8391.
16. Tejerina, B. and M.S. Gordon, Insertion mechanism of N-2 and O-2 into T-n(n=8, 10, 12)-silsesquioxane framework. Journal of Physical Chemistry B, 2002. 106(45): p. 11764-11770.

17. Liu, J.C., M-x-O-y-Si-z bonding models for silica-supported Ziegler-Natta catalysts. Applied Organometallic Chemistry, 1999. 13(4): p. 295-302.
18. Pescarmona, P.P., et al., A new, efficient route to titanium-silsesquioxane epoxidation catalysts developed by using high-speed experimentation techniques. Angewandte Chemie-International Edition, 2001. 40(4): p. 740-743.
19. Xiao, F.S., et al., Hydrothermally stable ordered mesoporous titanosilicates with highly active catalytic sites. Journal of the American Chemical Society, 2002. 124(6): p. 888-889.
20. Severn, J.R., et al., Silsesquioxane-bonded zirconocene complexes; soluble models for silica-tethered olefin polymerization catalysts. Dalton Transactions, 2003(11): p. 2293-2302.
21. Wada, K., et al., Synthesis and catalytic activity of group 4 metallocene containing silsesquioxanes bearing functionalized silyl groups. Organometallics, 2004. 23(24): p. 5824-5832.
22. Earley, C.W., A Quantum-Mechanical Investigation of Silsesquioxane Cages. Journal of Physical Chemistry, 1994. 98(35): p. 8693-8698.
23. Xiang, K.H., et al., Theoretical study of structural and electronic properties of H-silsesquioxanes. Journal of Physical Chemistry B, 1998. 102(44): p. 8704-8711.
24. Bharadwaj, R.K., R.J. Berry, and B.L. Farmer, Molecular dynamics simulation study of norbornene-POSS polymers. Polymer, 2000. 41(19): p. 7209-7221.
25. Striolo, A., C. McCabe, and P.T. Cummings, Thermodynamic and transport properties of polyhedral oligomeric sislesquioxanes in poly(dimethylsiloxane). Journal of Physical Chemistry B, 2005. 109(30): p. 14300-14307.
26. Chan, E.R., et al., Simulations of tetra-tethered organic/inorganic nanocube-polymer assemblies. Macromolecules, 2005. 38(14): p. 6168-6180.
27. Sastre, G., D.W. Lewis, and A. Corma, The role of the electrostatic potential, electric field and electric field gradient on the acidity of AFI and CHA zeotypes. Physical Chemistry Chemical Physics, 2000. 2(1): p. 177-185.
28. Tsiper, E.V. and K. Burke, Rules for minimal atomic multipole expansion of molecular fields. Journal of Chemical Physics, 2004. 120(3): p. 1153-1156.
29. Lamoureux, G. and B. Roux, Modeling induced polarization with classical Drude oscillators: Theory and molecular dynamics simulation algorithm. Journal of Chemical Physics, 2003. 119(6): p. 3025-3039.
30. Dick, B.G. and A.W. Overhauser, Theory of the Dielectric Constants of Alkali Halide Crystals. Physical Review, 1958. 112(1): p. 90-103.
31. Wojcik, M.C. and K. Hermansson, The problem of the detaching shell in the shell model potential for oxides. Chemical Physics Letters, 1998. 289(1-2): p. 211-218.
32. Mortier, W.J., S.K. Ghosh, and S. Shankar, Electronegativity Equalization Method for the Calculation of Atomic Charges in Molecules. Journal of the American Chemical Society, 1986. 108(15): p. 4315-4320.
33. Rappe, A.K. and W.A. Goddard, Charge Equilibration for Molecular-Dynamics Simulations. Journal of Physical Chemistry, 1991. 95(8): p. 3358-3363.
34. Louwen, J.N. and E.T.C. Vogt, Semi-empirical atomic charges for use in computational chemistry of molecular sieves. Journal of Molecular Catalysis a-Chemical, 1998. 134(1-3): p. 63-77.

35. Njo, S.L., J.F. Fan, and B. van de Graaf, Extending and simplifying the electronegativity equalization method. Journal of Molecular Catalysis a-Chemical, 1998. 134(1-3): p. 79-88.

Appendix B. Incorporation of Torsion Interaction in The Force Field

Part I: Formula

Use Rahman-Parinello-Nose Lagrangian

$$L=\frac{1}{2}\sum_{i=1}^{N}m_i\dot{\vec{s}}_i^T\underline{G}\dot{\vec{s}}_i f^2+\frac{1}{2}WTr(\dot{\underline{h}}^T\dot{\underline{h}})+\frac{Q}{2}\dot{f}^2-\phi-\underline{p}\Omega-\frac{1}{2}Tr(\underline{\Sigma}\underline{G})-(g+1)k_BT\ln f$$

where $\vec{r}_{ij}=\underline{h}\vec{s}_{ij}$, and ϕ is the potential of the system, which is composed of torsion potential and pair potential, $\phi=\sum_i^N\left(\sum_{j,k,n}\phi^{tor}\left(\vec{r}_{ij},\vec{r}_{jk},\vec{r}_{kn}\right)+\sum_{j>i}^N\phi^{pair}\left(r_{ij}\right)\right)$. There exists a relationship for lagrangian operator:

$$\frac{\partial}{\partial\theta}\left(\frac{\partial L}{\partial\dot{\vec{s}}_i}\right)=\frac{\partial L}{\partial\vec{s}}$$

Therefore,

$$\ddot{\vec{s}}_l=-\frac{1}{m_l\underline{G}f^2}\left(\sum_{l\in\{i,j,k,n\}}\frac{\partial\phi^{tor}(\vec{r}_{ij},\vec{r}_{jk},\vec{r}_{kn})}{\partial\vec{s}_l}+\sum_{j\neq l}^{N}\frac{\partial\phi^{pari}(r_{lj})}{\partial\vec{s}_l}\right)-\underline{G}^{-1}\dot{\underline{G}}\dot{\vec{s}}_l-2\dot{\vec{s}}_l\frac{\dot{f}}{f}$$

Now consider the contribution from torsion potential alone. (From now on the notion of $\ddot{\vec{s}}_i$ indicates the part of second derivative from torsion potential only)

$$\ddot{\vec{s}}_i=-\frac{1}{m_i\underline{G}f^2}\frac{\partial\phi^{tor}(\vec{r}_{ij},\vec{r}_{jk},\vec{r}_{kn})}{\partial\vec{s}_{ij}} \tag{B-1}$$

$$\ddot{\vec{s}}_j=-\frac{1}{m_j\underline{G}f^2}\left[\frac{\partial\phi^{tor}(\vec{r}_{ij},\vec{r}_{jk},\vec{r}_{kn})}{\partial\vec{s}_{jk}}-\frac{\partial\phi^{tor}(\vec{r}_{ij},\vec{r}_{jk},\vec{r}_{kn})}{\partial\vec{s}_{ij}}\right] \tag{B-2}$$

$$\ddot{\vec{s}}_k=-\frac{1}{m_k\underline{G}f^2}\left[\frac{\partial\phi^{tor}(\vec{r}_{ij},\vec{r}_{jk},\vec{r}_{kn})}{\partial\vec{s}_{kn}}-\frac{\partial\phi^{tor}(\vec{r}_{ij},\vec{r}_{jk},\vec{r}_{kn})}{\partial\vec{s}_{jk}}\right] \tag{B-3}$$

$$\ddot{\vec{s}}_n=-\frac{1}{m_n\underline{G}f^2}\left[-\frac{\partial\phi^{tor}(\vec{r}_{ij},\vec{r}_{jk},\vec{r}_{kn})}{\partial\vec{s}_{kn}}\right]=\frac{1}{m_n\underline{G}f^2}\frac{\partial\phi^{tor}(\vec{r}_{ij},\vec{r}_{jk},\vec{r}_{kn})}{\partial\vec{s}_{kn}} \tag{B-4}$$

The torsion potential function with the configuration shown in Fig 1 is as follows.

$$\phi^{tor}(\vec{r}_{ij},\vec{r}_{jk},\vec{r}_{kn})=A_1(1+\cos\theta)+A_2(1-\cos2\theta)+A_3(1+\cos3\theta)+A_4$$

where θ is the dihedral angle and cosθ is defined as,

$$\cos\theta = \frac{(\vec{r}_{ij} \times \vec{r}_{jk}) \cdot (\vec{r}_{jk} \times \vec{r}_{kn})}{\left|\vec{r}_{ij} \times \vec{r}_{jk}\right| \left|\vec{r}_{jk} \times \vec{r}_{kn}\right|}$$

For c-c-c-h and h-c-c-h, take A1=A2=0. Some literature gives the expression of torsion angle potential for c-c-c-h and h-c-c-h: c(1-cos3θ). However according to the plot of potential vs. θ shown in mathematica file "cos-plot" and the desired trans- and gauch- conformation of hydrocarbon shown in "torsion-conformation.ppt", we take A3(1+ cos3θ).

First, get the intermediate partial derivative of the torsion potential over cosθ. Since

$$\begin{aligned}\phi^{tor}(\vec{r}_{ij},\vec{r}_{jk},\vec{r}_{kn}) &= A_1(1+\cos\theta) + A_2(1-\cos 2\theta) + A_3(1+\cos 3\theta) + A_4 \\ &= A_1(1+\cos\theta) + A_2(2-2\cos^2\theta) + A_3(1+4\cos^3\theta - 3\cos\theta) + A_4 \\ &= 4A_3\cos^3\theta - 2A_2\cos^2\theta + (A_1 - 3A_3)\cos\theta + A_1 + 2A_2 + A_3 + A_4\end{aligned}$$

Therefore,

$$\frac{\partial\phi^{tor}(\vec{r}_{ij},\vec{r}_{jk},\vec{r}_{kn})}{\partial\cos\theta} = 12A_3(\cos\theta)^2 - 4A_2\cos\theta + (A_1 - 3A_3) \qquad \text{(B-5)}$$

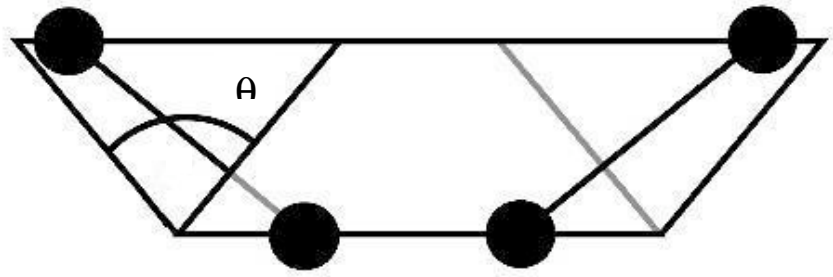

The dihedral angle and associated vectors

Then,

$$\frac{\partial\cos\theta}{\partial\vec{s}_{ij}} = \frac{\dfrac{\partial[(\vec{r}_{ij} \times \vec{r}_{jk}) \cdot (\vec{r}_{jk} \times \vec{r}_{kn})]}{\partial\vec{s}_{ij}}}{\left|\vec{r}_{ij} \times \vec{r}_{jk}\right| \left|\vec{r}_{jk} \times \vec{r}_{kn}\right|} + \frac{(\vec{r}_{ij} \times \vec{r}_{jk}) \cdot (\vec{r}_{jk} \times \vec{r}_{kn})}{\left|\vec{r}_{jk} \times \vec{r}_{kn}\right|} \frac{\partial\left(\dfrac{1}{\left|\vec{r}_{ij} \times \vec{r}_{jk}\right|}\right)}{\partial\vec{s}_{ij}} \qquad \text{(B-6)}$$

To simplify the derivative calculation, assign $(\vec{r}_{ij} \times \vec{r}_{jk})$ to vector M, and assign $\vec{r}_{jk} \times \vec{r}_{kn}$ to vector N. Hence, First part of the equation (B-6)

$$\frac{\partial[(\vec{r}_{ij} \times \vec{r}_{jk}) \cdot (\vec{r}_{jk} \times \vec{r}_{kn})]}{\partial \vec{s}_{ij}} \Big/ \left|\vec{r}_{ij} \times \vec{r}_{jk}\right\|\vec{r}_{jk} \times \vec{r}_{kn}\Big| = \frac{\partial[(\vec{r}_{ij} \times \vec{r}_{jk}) \cdot B]}{\partial \vec{s}_{ij}} \Big/ |A| \cdot |B| = \frac{(B \cdot \frac{\partial}{\partial \vec{s}_{ij}})(\vec{r}_{ij} \times \vec{r}_{jk}) + B \times (\frac{\partial}{\partial \vec{s}_{ij}} \times (\vec{r}_{ij} \times \vec{r}_{jk}))}{|A| \cdot |B|}$$

$$= \frac{(B \cdot \frac{\partial}{\partial \vec{s}_{ij}})(\vec{r}_{ij} \times \vec{r}_{jk}) + B \times ((\vec{r}_{jk} \cdot \frac{\partial}{\partial \vec{s}_{ij}})\vec{r}_{ij} - \vec{r}_{jk}(\frac{\partial}{\partial \vec{s}_{ij}} \cdot \vec{r}_{ij}))}{|A| \cdot |B|}$$

$$= \frac{(B_x \frac{d}{ds_{ijx}} + B_y \frac{d}{ds_{ijy}} + B_z \frac{d}{ds_{ijz}})[(r_{ijy} r_{jkz} - r_{jky} r_{ijz})\hat{i} + (r_{ijz} r_{jkx} - r_{jkz} r_{ijx})\hat{j} + (r_{ijx} r_{jky} - r_{jkx} r_{ijy})\hat{k})}{|A| \cdot |B|} +$$

$$\frac{B \times ((r_{jkx} \frac{d}{ds_{ijx}} + r_{jky} \frac{d}{ds_{ijy}} + r_{jkz} \frac{d}{ds_{ijz}})\vec{r}_{ij} - \vec{r}_{jk}(\frac{dr_{ijx}}{ds_{ijx}} + \frac{dr_{ijy}}{ds_{ijy}} + \frac{dr_{ijz}}{ds_{ijz}}))}{|A| \cdot |B|} \qquad \text{(B-7)}$$

Because

$$\vec{r}_{ij} = \underline{h}\vec{s}_{ij} = (h_{11} s_{ijx} + h_{12} s_{ijy} + h_{13} s_{ijz})\hat{i} + (h_{21} s_{ijx} + h_{22} s_{ijy} + h_{23} s_{ijz})\hat{j} + (h_{31} s_{ijx} + h_{32} s_{ijy} + h_{33} s_{ijz})\hat{k}$$

Then,

$$\text{(B-7)} * (|A| \cdot |B|) = [B_x(h_{21} r_{jkz} - h_{31} r_{jky}) + B_y(h_{22} r_{jkz} - h_{32} r_{jky}) + B_z(h_{23} r_{jkz} - h_{33} r_{jky})]\hat{i} +$$

$$[B_x(h_{31} r_{jkx} - h_{11} r_{jkz}) + B_y(h_{32} r_{jkx} - h_{12} r_{jkz}) + B_z(h_{33} r_{jkx} - h_{13} r_{jkz})]\hat{j} +$$

$$[B_x(h_{11} r_{jky} - h_{21} r_{jkx}) + B_y(h_{12} r_{jky} - h_{22} r_{jkx}) + B_z(h_{13} r_{jky} - h_{23} r_{jkx})]\hat{k} \quad +$$

$$B \times [(r_{jkx} h_{11} + r_{jky} h_{12} + r_{jkz} h_{13})\hat{i} + (r_{jkx} h_{21} + r_{jky} h_{22} + r_{jkz} h_{23})\hat{j} + (r_{jkx} h_{31} + r_{jky} h_{32} + r_{jkz} h_{33})\hat{k} - \vec{r}_{jk}(h_{11} + h_{22} + h$$

$$= [B_x(h_{21} r_{jkz} - h_{31} r_{jky}) + B_y(h_{31} r_{jkx} - h_{11} r_{jkz}) + B_z(h_{11} r_{jky} - h_{21} r_{jkx})]\hat{i} +$$

$$[B_x(h_{22} r_{jkz} - h_{32} r_{jky}) + B_y(h_{32} r_{jkx} - h_{12} r_{jkz}) + B_z(h_{12} r_{jky} - h_{22} r_{jkx})]\hat{j} +$$

$$[B_x(h_{23} r_{jkz} - h_{33} r_{jky}) + B_y(h_{33} r_{jkx} - h_{13} r_{jkz}) + B_z(h_{13} r_{jky} - h_{23} r_{jkx})]\hat{k}$$

$$= [h_{11}(r_{jky} B_z - r_{jkz} B_y) + h_{21}(r_{jkz} B_x - r_{jkx} B_z) + h_{31}(r_{jkx} B_y - r_{jky} B_x)]\hat{i} +$$

$$[h_{12}(r_{jky} B_z - r_{jkz} B_y) + h_{22}(r_{jkz} B_x - r_{jkx} B_z) + h_{32}(r_{jkx} B_y - r_{jky} B_x)]\hat{j} +$$

$$[h_{13}(r_{jky} B_z - r_{jkz} B_y) + h_{23}(r_{jkz} B_x - r_{jkx} B_z) + h_{33}(r_{jkx} B_y - r_{jky} B_x)]\hat{k} == \underline{h}^T(\vec{r}_{jk} \times B)$$

$$= \frac{\underline{h}^T(\vec{r}_{jk} \times B)}{|A| \cdot |B|}$$

Hence, (B-7)

And the second part of the equation (B-6) is

$$\frac{(\vec{r}_{ij} \times \vec{r}_{jk}) \cdot (\vec{r}_{jk} \times \vec{r}_{kn})}{|\vec{r}_{jk} \times \vec{r}_{kn}|} \frac{\partial(\frac{1}{|\vec{r}_{ij} \times \vec{r}_{jk}|})}{\partial \vec{s}_{ij}} = \frac{A \cdot B}{|B|} \frac{\partial(\frac{1}{|A|})}{\partial \vec{s}_{ij}} = -\frac{1}{2} \frac{A \cdot B}{|A|^3 |B|} \frac{\partial(|A|^2)}{\partial \vec{s}_{ij}}$$

$$= -\frac{1}{2} \frac{\cos\theta}{|A|^2} \frac{\partial[(r_{ijy} r_{jkz} - r_{ijz} r_{jky})^2 + (r_{ijz} r_{jkx} - r_{ijx} r_{jkz})^2 + (r_{ijx} r_{jky} - r_{ijy} r_{jkx})^2]}{\partial \vec{s}_{ij}} =$$

$$-\frac{\cos\theta}{|A|^2} [A_x \frac{r_{jkz} \partial r_{ijy} - r_{jky} \partial r_{ijz}}{\partial \vec{s}_{ij}} + A_y \frac{r_{jkx} \partial r_{ijz} - r_{jkz} \partial r_{ijx}}{\partial \vec{s}_{ij}} + A_z \frac{r_{jky} \partial r_{ijx} - r_{jkx} \partial r_{ijy}}{\partial \vec{s}_{ij}}] \qquad \text{(B-8)}$$

Therefore

$$\frac{(8)}{\frac{\cos\theta}{|A|^2}} = -\{A_x[r_{jkz}(h_{21}\hat{i} + h_{22}\hat{j} + h_{23}\hat{k}) - r_{jky}(h_{31}\hat{i} + h_{32}\hat{j} + h_{33}\hat{k})]$$

$$+ A_y[r_{jkx}(h_{31}\hat{i} + h_{32}\hat{j} + h_{33}\hat{k}) - r_{jkz}(h_{11}\hat{i} + h_{12}\hat{j} + h_{13}\hat{k})]$$

$$+ A_z[r_{jky}(h_{11}\hat{i} + h_{12}\hat{j} + h_{13}\hat{k}) - r_{jkx}(h_{21}\hat{i} + h_{22}\hat{j} + h_{32}\hat{k})]\}$$

$$= -\{[h_{11}(r_{jky}A_z - r_{jkz}A_y) + h_{21}(r_{jkz}A_x - r_{jkx}A_z) + h_{31}(r_{jkx}A_y - r_{jky}A_x)]\hat{i}$$

$$+ [h_{12}(r_{jky}A_z - r_{jkz}A_y) + h_{22}(r_{jkz}A_x - r_{jkx}A_z) + h_{32}(r_{jkx}A_y - r_{jky}A_x)]\hat{j}$$

$$+ [h_{13}(r_{jky}A_z - r_{jkz}A_y) + h_{23}(r_{jkz}A_x - r_{jkx}A_z) + h_{33}(r_{jkx}A_y - r_{jky}A_x)]\hat{k}\}$$

$$= \underline{h}(A \times \vec{r}_{jk})$$

Hence, combine (B-7) and (B-8), we get

$$\frac{\partial \cos\theta}{\partial \vec{s}_{ij}} = \underline{h}^T [\frac{\vec{r}_{jk} \times (\vec{r}_{jk} \times \vec{r}_{kn})}{|\vec{r}_{ij} \times \vec{r}_{jk}| |\vec{r}_{jk} \times \vec{r}_{kn}|} + \cos\theta \frac{(\vec{r}_{ij} \times \vec{r}_{jk}) \times \vec{r}_{jk}}{|\vec{r}_{ij} \times \vec{r}_{jk}|^2}] \qquad \text{(B-9)}$$

simillarly,

$$\frac{\partial \cos\theta}{\partial \vec{s}_{jk}} = \frac{\frac{\partial[(\vec{r}_{ij} \times \vec{r}_{jk}) \cdot (\vec{r}_{jk} \times \vec{r}_{kn})]}{\partial \vec{s}_{jk}}}{|\vec{r}_{ij} \times \vec{r}_{jk}| |\vec{r}_{jk} \times \vec{r}_{kn}|} + \frac{(\vec{r}_{ij} \times \vec{r}_{jk}) \cdot (\vec{r}_{jk} \times \vec{r}_{kn})}{|\vec{r}_{jk} \times \vec{r}_{kn}|} \frac{\partial(\frac{1}{|\vec{r}_{ij} \times \vec{r}_{jk}|})}{\partial \vec{s}_{jk}} + \frac{(\vec{r}_{ij} \times \vec{r}_{jk}) \cdot (\vec{r}_{jk} \times \vec{r}_{kn})}{|\vec{r}_{ij} \times \vec{r}_{jk}|} \frac{\partial(\frac{1}{|\vec{r}_{jk} \times \vec{r}_{kn}|})}{\partial \vec{s}_{jk}}$$

$$= \underline{h}^T [\frac{-(\vec{r}_{ij} \times \vec{r}_{jk}) \times \vec{r}_{kn} - \vec{r}_{ij} \times (\vec{r}_{jk} \times \vec{r}_{kn})}{|\vec{r}_{ij} \times \vec{r}_{jk}| |\vec{r}_{jk} \times \vec{r}_{kn}|} + \cos\theta (\frac{\vec{r}_{ij} \times (\vec{r}_{ij} \times \vec{r}_{jk})}{|\vec{r}_{ij} \times \vec{r}_{jk}|^2} + \frac{(\vec{r}_{jk} \times \vec{r}_{kn}) \times \vec{r}_{kn}}{|\vec{r}_{jk} \times \vec{r}_{kn}|^2})] \qquad \text{(B-10)}$$

and,

$$\frac{\partial \cos\theta}{\partial \vec{s}_{kn}} = \frac{\frac{\partial[(\vec{r}_{ij}\times\vec{r}_{jk})\cdot(\vec{r}_{jk}\times\vec{r}_{kn})]}{\partial \vec{s}_{kn}}}{\left|\vec{r}_{ij}\times\vec{r}_{jk}\right|\left|\vec{r}_{jk}\times\vec{r}_{kn}\right|} + \frac{(\vec{r}_{ij}\times\vec{r}_{jk})\cdot(\vec{r}_{jk}\times\vec{r}_{kn})}{\left|\vec{r}_{ij}\times\vec{r}_{jk}\right|}\frac{\partial(\frac{1}{\left|\vec{r}_{jk}\times\vec{r}_{kn}\right|})}{\partial \vec{s}_{kn}}$$

$$= \underline{h}^T[\frac{(\vec{r}_{ij}\times\vec{r}_{jk})\times\vec{r}_{jk}}{\left|\vec{r}_{ij}\times\vec{r}_{jk}\right|\left|\vec{r}_{jk}\times\vec{r}_{kn}\right|} + \cos\theta\frac{\vec{r}_{jk}\times(\vec{r}_{jk}\times\vec{r}_{kn})}{\left|\vec{r}_{jk}\times\vec{r}_{kn}\right|^2}] \qquad \text{(B-11)}$$

hence,

$$\ddot{\vec{s}}_i = -\frac{\underline{h}^{-1}}{m_i f^2}[12A_3(\cos\theta)^2 - 4A_2\cos\theta + (A_1 - 3A_3)][\frac{\vec{r}_{jk}\times(\vec{r}_{jk}\times\vec{r}_{kn})}{\left|\vec{r}_{ij}\times\vec{r}_{jk}\right|\left|\vec{r}_{jk}\times\vec{r}_{kn}\right|} + \cos\theta\frac{(\vec{r}_{ij}\times\vec{r}_{jk})\times\vec{r}_{jk}}{\left|\vec{r}_{ij}\times\vec{r}_{jk}\right|^2}]$$

and,

$$\ddot{\vec{s}}_j = \frac{\underline{h}^{-1}}{m_j f^2}[12A_3(\cos\theta)^2 - 4A_2\cos\theta + (A_1 - 3A_3)][\frac{(\vec{r}_{ij}\times\vec{r}_{jk})\times\vec{r}_{kn} + (\vec{r}_{ij}+\vec{r}_{jk})\times(\vec{r}_{jk}\times\vec{r}_{kn})}{\left|\vec{r}_{ij}\times\vec{r}_{jk}\right|\left|\vec{r}_{jk}\times\vec{r}_{kn}\right|}$$

$$-\cos\theta(\frac{(\vec{r}_{ij}+\vec{r}_{jk})\times(\vec{r}_{ij}\times\vec{r}_{jk})}{\left|\vec{r}_{ij}\times\vec{r}_{jk}\right|^2} + \frac{(\vec{r}_{jk}\times\vec{r}_{kn})\times\vec{r}_{kn}}{\left|\vec{r}_{jk}\times\vec{r}_{kn}\right|^2})]$$

and,

$$\ddot{\vec{s}}_k = -\frac{\underline{h}^{-1}}{m_k f^2}[12A_3(\cos\theta)^2 - 4A_2\cos\theta + (A_1 - 3A_3)][\frac{(\vec{r}_{ij}\times\vec{r}_{jk})\times(\vec{r}_{jk}+\vec{r}_{kn}) + \vec{r}_{ij}\times(\vec{r}_{jk}\times\vec{r}_{kn})}{\left|\vec{r}_{ij}\times\vec{r}_{jk}\right|\left|\vec{r}_{jk}\times\vec{r}_{kn}\right|}$$

$$-\cos\theta(\frac{\vec{r}_{ij}\times(\vec{r}_{ij}\times\vec{r}_{jk})}{\left|\vec{r}_{ij}\times\vec{r}_{jk}\right|^2} + \frac{(\vec{r}_{jk}\times\vec{r}_{kn})\times(\vec{r}_{jk}+\vec{r}_{kn})}{\left|\vec{r}_{jk}\times\vec{r}_{kn}\right|^2})]$$

and,

$$\ddot{\vec{s}}_n = \frac{\underline{h}^{-1}}{m_n f^2}[12A_3(\cos\theta)^2 - 4A_2\cos\theta + (A_1 - 3A_3)][\frac{(\vec{r}_{ij}\times\vec{r}_{jk})\times\vec{r}_{jk}}{\left|\vec{r}_{ij}\times\vec{r}_{jk}\right|\left|\vec{r}_{jk}\times\vec{r}_{kn}\right|} + \cos\theta\frac{\vec{r}_{jk}\times(\vec{r}_{jk}\times\vec{r}_{kn})}{\left|\vec{r}_{jk}\times\vec{r}_{kn}\right|^2}]$$

Part II Codes in fortran

```
subroutine frc4b

      real rij(0:3)
      real rjk(0:3)
      real rkn(0:3)
      real r1(3)
      real r2(3)
      real rr
      real rs
      real dd
      real csph

      real pe
      real ff
      real fij(3)
      real fjk(3)
      real fkn(3)

      real vija(3)
      real vijb(3)
      real vjka(3)
      real vjkb(3)
      real vkna(3)
      real vknb(3)
```

```
      real angle

c compute 4 body dihedral interaction ...
      include 'params.h'

      include 'strcts.m'
      include 'pt4par.m'
      include 'tensrs.m'
      include 'confg.m'
      include 'coordr.m'
      include 'cntrl.m'
      include 'radial.m'
      include 'systm.m'
      include 'optnl.m'
      include 'stats.m'

c make sure icen1 <= icen2
c compute dihedral angle start with j of ijkn
      do 100 j=ist(icen1),ien(icen1)
       do 100 kk=1,nbcnt(0,j)
         k=nblst(kk,j)
         if(k.gt.j.and.ispcs(k).eq.icen2) then
c center atom decided, then find i and n

           do 120 ii=1,nbcnt(0,j)
             i=nblst(ii,j)
```

```
                if(i.ne.k) then
   c i decided
                  do 140 nn=1,nbcnt(0,k)
                    n=nblst(nn,k)

                    nspi=ispcs(i)
                    nspn=ispcs(n)
                    if(nspi.gt.nspn) then
                         isp=nspn
                         nspn=nspi
                         nspi=isp
                    endif

                    if(n.ne.j.and.isgn(nspn,nspi).eq.1)
then



   c begin calculate force, potential energy and dihedral
distribution

                      rij(0)=dstnb(0,ii,j)
                      rjk(0)=dstnb(0,kk,j)
                      rkn(0)=dstnb(0,nn,k)

                      do 160 m=1,3
                         rij(m)=dstnb(m,ii,j)
                         rjk(m)=-dstnb(m,kk,j)
```

```
                        rkn(m)=-dstnb(m,nn,k)
 160                continue

   c found three vectors
   c get cos(phi)
                      r1(1)=rij(2)*rjk(3)-rij(3)*rjk(2)
                      r1(2)=rij(3)*rjk(1)-rij(1)*rjk(3)
                      r1(3)=rij(1)*rjk(2)-rij(2)*rjk(1)
                      rr=r1(1)*r1(1)+r1(2)*r1(2)+r1(3)*r1(3)

                      r2(1)=rjk(2)*rkn(3)-rjk(3)*rkn(2)
                      r2(2)=rjk(3)*rkn(1)-rjk(1)*rkn(3)
                      r2(3)=rjk(1)*rkn(2)-rjk(2)*rkn(1)
                      rs=r2(1)*r2(1)+r2(2)*r2(2)+r2(3)*r2(3)

csph=r1(1)*r2(1)+r1(2)*r2(2)+r1(3)*r2(3)
                      dd=sqrt(rr)*sqrt(rs)
                      csph=csph/dd

   c                   cs2ph=2.0*csph*csph-1.0
   c                   cs3ph=csph*(4.0*csph*csph-3.0)

                      pe = a1(nspn,nspi)*(1.+csph) +
        &         2.*a2(nspn,nspi)*(1.-csph*csph) +
        &         a3(nspn,nspi)*(1+4.*csph**3.-3.*csph) +
```

```
     &        a4(nspn,nspi)

                    dpe = dpe + pe
c                    pe = pe/(nbcnt(0,j)-1)
c                    dpe=dpe+pe/(nbcnt(0,k)-1)

c potential energy calculated
c now force

                    ff=-
a1(nspn,nspi)+4.0*a2(nspn,nspi)*csph-
     &        3.0*a3(nspn,nspi)*(4.0*csph*csph-1.0)

c                    ff = ff/(nbcnt(0,j)-1)
c                    ff = ff/(nbcnt(0,k)-1)

                   vija(1)=rij(2)*r1(3)-rij(3)*r1(2)
                   vija(2)=rij(3)*r1(1)-rij(1)*r1(3)
                   vija(3)=rij(1)*r1(2)-rij(2)*r1(1)

                   vjka(1)=rjk(2)*r1(3)-rjk(3)*r1(2)
                   vjka(2)=rjk(3)*r1(1)-rjk(1)*r1(3)
                   vjka(3)=rjk(1)*r1(2)-rjk(2)*r1(1)

                   vkna(1)=rkn(2)*r1(3)-rkn(3)*r1(2)
                   vkna(2)=rkn(3)*r1(1)-rkn(1)*r1(3)
```

```
                        vkna(3)=rkn(1)*r1(2)-rkn(2)*r1(1)

                        vijb(1)=rij(2)*r2(3)-rij(3)*r2(2)
                        vijb(2)=rij(3)*r2(1)-rij(1)*r2(3)
                        vijb(3)=rij(1)*r2(2)-rij(2)*r2(1)

                        vjkb(1)=rjk(2)*r2(3)-rjk(3)*r2(2)
                        vjkb(2)=rjk(3)*r2(1)-rjk(1)*r2(3)
                        vjkb(3)=rjk(1)*r2(2)-rjk(2)*r2(1)

                        vknb(1)=rkn(2)*r2(3)-rkn(3)*r2(2)
                        vknb(2)=rkn(3)*r2(1)-rkn(1)*r2(3)
                        vknb(3)=rkn(1)*r2(2)-rkn(2)*r2(1)

                        do 180 m=1,3
                         fij(m)=vjkb(m)/dd-csph*vjka(m)/rr
                         fij(m)=fij(m)*ff

                         fkn(m)=-vjka(m)/dd+csph*vjkb(m)/rs
                         fkn(m)=fkn(m)*ff

                         fjk(m)=(vkna(m)-
vijb(m))/dd+csph*vija(m)/rr
        &       -csph*vknb(m)/rs
                         fjk(m)=fjk(m)*ff
```

```
c force calculation done

                    frc(m,i)=frc(m,i) - fij(m)
                    frc(m,j)=frc(m,j) + fij(m) - fjk(m)
                    frc(m,k)=frc(m,k) + fjk(m) - fkn(m)
                    frc(m,n)=frc(m,n) + fkn(m)


c pressure tensor, here the pressure tensor seems to be
c the stress tensor by concept

                    do 185 lc = 1, 3
                      ptns(lc,m) = ptns(lc,m) +
      &
rij(lc)*fij(m)+rjk(lc)*fjk(m)+rkn(lc)*fkn(m)

 185                continue

 180               continue


c now get the distribution of dihedral angles
                   nt=(it-1)/wkt
                   if((it-nt*wkt).gt.idlt) then
                      angle=acos(csph)*45.0/atan(1.0)
                      iag=int(angle/fld(1,4))+1
```

```
                        ip=nspc*(nspi-1)+nspn-nspi*(nspi-
1)/2
   c a = nspc, b = nspc-nspi+2, height = nspi-1
   c ip = (a+b)*height/2 + (nspn-nspi+1)
   c put the 2D triangle array into 1D
                        if(iag.gt.0) then
csntsn(iag,ip)=csntsn(iag,ip)+10.
                           numcsn(ip) = numcsn(ip) + 1
                        endif
                     endif


                   endif
    140           continue

               endif
    120       continue
           endif
    100  continue

         return


         end
```